ISSN 2377-9098

AIMS Biophysics

Volume No. 12

Issue No. 2

May-August 2025

ENRICHED PUBLICATIONS PVT. LTD

S-9, IInd FLOOR, MLU POCKET,
MANISH ABHINAV PLAZA-II, ABOVE FEDERAL BANK,
PLOT NO-5, SECTOR-5, DWARKA, NEW DELHI, INDIA-110075,
PHONE: - + (91)-(11)-47026006

ISSN 2377-9098

AIMS Biophysics

Aims and Scope

AIMS Biophysics is an international Open Access journal devoted to publishing peer-reviewed, high quality, original papers in the field of biophysics. We publish the following article types: original research articles, reviews, editorials, letters, and conference reports.

AIMS Biophysics welcomes, but not limited to, the papers from the following topics:

- Structural biology
- Biophysical technology
- Bioenergetics
- Membrane biophysics
- Cellular Biophysics
- Electrophysiology
- Neuro-Biophysics
- Biomechanics
- Systems biology

ISSN 2377-9098

AIMS Biophysics

ISSN 2377-9098

AIMS Biophysics

(Volume No. 12, Issue No. 2, May - August 2025)

Contents

Development and bioevaluation of controlled release 5aminoisoquinoline nanocomposite: a synergistic anticancer activity against human colon cancer

Alaa AL-Rahman Gamal1, El-Sayed Mahmoud El-Sayed1, Tarek El-Hamoly2,3,* and Heba Kahil1

1 Biophysics group, Physics Department, Faculty of Science, Ain Shams University, Cairo Egypt
2 Drug Radiation Research Department, National Center for Radiation Research and Technology, Egyptian Atomic Energy Authority, Cairo, Egypt
3 Cyclotron Project, Nuclear Research Centre, Egyptian Atomic Energy Authority, Cairo, Egypt

ABSTRACT

The current study presents a bimodal therapeutic platform for cancer treatment. Bimodal implies that the presented drug loaded core-shell structure is capable of elevating the tumor tissue temperature (hyperthermia) through the superparamagnetic iron oxide core and simultaneously release a Poly (ADP-ribose) polymerase-1(PARP-1)-modifying agent from the thermoresponsive shell. Magnetic thermoresponsive nanocomposite MTN was synthesized via an in situ free radical polymerization of thermo-responsive (N-isopropylacrylamide) (NIPAAm) monomer in the presence of 11-nm monodisperse SPIONs. The composite was allowed to swell in various concentrations of the PARP inhibitor: 5-aminoisoquinoline (5-AIQ) forming drug-loaded magnetic thermoresponsive nanocomposite (MTN-5.AIQ). Structural characterization of the formed composite is studied via various experimental tools. To assess the coil to globule transition temperature, the lower critical solution temperature (LCST) is determined by differential scanning calorimetry (DSC) method and the cloud point (Tp) is determined by turbidometry. Magnetic thermoresponsive nanocomposite (MTN) is formed with excellent potential for hyperthermia. A high drug loading efficiency (85.72%) is obtained with convenient temperature dependent drug release kinetics. Biocompatibility and cytotoxic efficacy are tested on an in vivo and in vitro colorectal-adenocarcinoma model, respectively. MTN.5AIQ administration exhibits normal hepatic and renal functions as well as lower toxic effect on normal tissue. In addition, the composite effectively inhibits Caco-2 cells viability upon incubation. Based on tissue. In addition, the composite effectively inhibits Caco-2 cells viability upon incubation. Based on the obtained results, the proposed therapeutic platform can be considered as a novel, promising candidate for dual therapy of colorectal adenocarcinoma exhibiting a PARP-1 overexpression. as well as increased the inhabiting efficacy of 5-AIQ. the obtained results, the proposed therapeutic platform can be considered as a novel, promising candidate for dual therapy of colorectal adenocarcinoma exhibiting a PARP-1 overexpression. as well as increased the inhabiting efficacy of 5-AIQ.

Keywords: SPIONs; thermoresponsive polymer; hyperthermia; PARP inhibitor; PNIPAM

Abbreviations: 5-AIQ: 5-aminoisoquinoline; AMF: Alternating magnetic field; EDX: Energy dispersive X-ray ; FCC: Face centered cubic ; FTIR: Fourier transform infrared spectroscopy; GOT: Glutamic oxaloacetic transaminase; GPT: Glutamic pyruvic transaminase; HPLC: High performance liquid chromatography; HRTEM: High resolution transmission electron microscope; LCST: Lower critical solution temperature; MTN: Magnetic thermoresponsive nanocomposite; PARP-1: Poly (ADPribose) polymerase-1; PNIPAAm: Poly(N-isopropylacrylamide); SAR: Specific absorption rate; SPIONs: Superparamagnetic iron oxide nanoparticles; TCP: Cloud point temperature; XRD: X-ray diffraction.

1. Introduction

Enormous interest has been focused on developing smart delivery vehicles capable of targeting and controlling the release of chemotherapeutic agents. Controlled drug release is very attractive as it overcomes various drawbacks of conventional chemotherapy. Limitations of using chemotherapy with subsequent adverse outcomes on healthy tissues can be attributed to incompatible pharmacokinetics as well as narrow therapeutic indices [1]. Recently, the utilization of smart polymers showed great potential for controlling drug release when subjected to external stimuli such as temperature, PH, electric/magnetic field, light, etc. [1]. Among the various thermoresponsive polymers, Poly(Nisopropyl acrylamide)(PNIPAAm) is the most extensively used candidate.

The current study reported the design of a core-shell drug loaded platform, in which SPIONs constitute the core that acts as the heat source, and PNIPAAm acts as the thermoresponsive shell, together they constitute the core shell magnetic thermoresponsive nanocomposite (MTN). 5aminoisoquinoline (5-AIQ) acts as a PARP inhibitor loaded on MTN. This drug loaded magnetic thermoresponsive nanocomposite (MTN.5-AIQ) can be intravenously injected and targeted to the tumor site by a magnetic field gradient. An alternating magnetic field (AMF) then triggers heat production by the SPION cores, which consequently triggers drug release. The elevated temperature along with the chemotherapeutic agent are awaited to play synergistic roles in tumor treatment.

The thermoresponsive Poly(N-isopropylacrylamide) (PNIPAAm) is frequently used for drug delivery owing to its convenient coil to globule transition temperature; the effect that can favor its use over other alternatives in a multitude of biomedical applications [1,2]. This polymer exhibits thermally reversible coil-to-globule phase transition when the temperature changes around the LCST of the polymer. At temperatures below its LCST, PNIPAAm becomes hydrophilic as it swells and extends in virtue of the intermolecular hydrogen bonds formed between polymer chains and water molecules. Whereas, above LCST, the polymer chain collapses, releases much of the water content and eventually shrinks. These reversible shrinking and water release of PNIPAAm are exploited for drug loading and release. The hydrophilicity of the polymer can be modified by association of SPIONs and drug loading resulting in an increase LCST. The high temperature generated by induction heating leads to coil-to globule transition of the composite, followed by expulsion of the loaded drug in a controlled manner.

SPIONs act as tiny antennae that generate heat upon exposure to alternating magnetic field (AMF). They exhibit superparamagnetic behavior at room temperature, which implies that they can be magnetized by applying magnetic field and lose their magnetization when the field is removed [3]. Heat dissipation from these superparamagnetic nanoparticles is caused by two relaxation mechanisms; the rotation of the moments within the particle (Néel relaxation) and the physical rotation of the particle itself (Brownian or viscous loss) [4] upon exposure to AMF. Néel (τN) and Brownian (τB) magnetic relaxation times of a particle are given by Equation 1 and Equation 2 [5] respectively; where τN is the Néel relaxation time, τB is the Brownian relaxation time, Vm is the volume of the magnetic core, K is

the anisotropy constant, k_B is the Boltzmann constant, T is the absolute temperature, f is an attempt frequency for changes in the dipole direction, η is the viscosity of the carrier fluid and V_{hyd} is the hydrodynamic volume of the particle.

$$\tau_N = \frac{1}{f_\circ} exp\left(\frac{KV_m}{K_B T}\right) \quad (1)$$

$$\tau_B = \frac{3V_{hyd}}{K_B T}\eta \quad (2)$$

PARP-1 belongs to the superfamily of more than seventeen enzymes that catalyzes the transfer of ADPribose units from its substrate NAD+ to several protein acceptors as single-strand break repair and base excision repair factors which contribute to DNA repair [6]. In general, PARP inhibitors act through competitive blocking of the NAD+ binding domain of the enzyme [7]; the effect which inhibits the repair of damaged DNA and facilitates apoptosis-dependent death of tumor cells [8]. 5aminoisoquinoline (5-AIQ) is an active, water soluble inhibitor of Poly (ADP-ribose) polymerase-1 (PARP-1) that adjunctly promotes radiotherapy and chemotherapy of various cancer types [9]. The elevated mortality associated with metastatic colon cancer is attributed to further development of resistant microenvironments towards current drugs [10–12]. Today, different techniques are dedicated to prognose these types of resistance and the progress of their treatment regimens [13]. Latest chemotherapeutic protocols for colon cancer include DNA-modifying pharmaceuticals, like oxaliplatin or irinotecan, combined with 5-fluorouracil [14]. Furthermore, many studies revealed the anti-cancer effect of the natural flavonoids in treatment of colorectal cancers [15–17]. Such treatment regimens are initially successful in numerous patients, but ultimately, the majority of patients become resistant. A significant interpretation of this resistance in colon cancer is the frequent DNA repair mechanism-linked to high expression of PARPs enzymes [18]. Previous studies investigated the use of commercially available PARP-1 inhibitors like Olaparib alone or in combination with the chemotherapeutic agents , the latter was accepted as a promising candidate for treatment of colon cancer [19]. Magnetite coated with thermoresponsive polymer and its derivatives was previously synthesized for drug delivery and controlled drug release applications. Doxorubicin was loaded on the magnetite thermoresponsive nanocomposite and used as the anticancer model drug [20–22]. In addition, indomethacin was loaded on thermo-responsive magnetic nanoclusters grafted with Poly(Nisopropylacrylamide) and PNIPAAm-co-PEGMA copolymers and was used as the anticancer model drug [23]. The current work investigates the feasibility of loading 5-aminoioquinoline drug (5-AIQ) on the magnetic thermoresponsive polymer and its release kinetics.

2. Materials and methods

2.1. Chemicals

Ferric chloride hexahydrate (FeCl3.6H2O, 97%), ferrous chloride Tetrahydrate (FeCl2.4H2O, 98%), sodium hydroxide pellets (NaOH, 98%) and ammonium persulfate (APS, 98%) were purchased from LOBA CHEMIE PVT.LTD. While, N, isopropylacrylamide monomer (NIPAAm, 97%), N-methylene bisacrylamide (MBA, 99%), N,N,N′,N′Tetramethylethylenediamine (TEMED, 99%) and 5Aminoisoquinoline (5-AIQ) and Phosphate buffer saline (PBS) were purchased from Sigma Aldrich. Caco-2 cell lines were purchased from the Cell Bank of Egyptian company for production of vaccine, sera and drugs (VACSERA) (Cairo, Egypt). (RPMI) medium, Methylthiazolyldiphenyl-tetrazolium

bromide (MTT) and Dimethyl sulfoxide (DMSO) were obtained from Sigma-Aldrich, St. Louis, MO, USA. All used chemicals are analytical grade.

2.2. Synthesis of superparamagnetic iron oxide nanoparticles SPIONs

SPIONs were prepared by the co-precipitation method. Briefly, 4.44 g of ferric chloride hexahydrate and 2.12 g of ferrous chloride tetra hydrate were dissolved in 150 ml of deionized water under magnetic stirring at 80 ℃ for 15 min; the pH of the solution was adjusted to 13 by addition of 10 M sodium hydroxide solution. After another 15 minutes of stirring at 80 ℃, the black precipitate (iron oxide nanoparticles) was formed. The precipitate was separated by strong magnet and washed times with distilled water. Finally, these nanoparticles were dried under vacuum at room temperature overnight. The obtained SPIONs powders were used for synthesis of magnetic thermoresponsive nanocomposite based on iron oxide and PNIPAAM (MTN).

2.3. Synthesis of magnetic thermoresponsive nanocomposite (MTN)

N-isopropyacrylamide monomer was polymerized in the presence of SPIONs by free radical polymerization reaction. 66.4 ml solution of SPIONs (0.1 M) was added to 56.9 ml solution of NIPAAm monomer (0.28 M) and sonicated for 10 min. The mixture was transferred to a magnetic stirrer, during stirring, 4.74 ml of the crosslinker MBA solution (0.01 M) and 0.95 ml of the initiator APS (0.27 M) were added to the mixture. Afterwards, 1.8 ml TEMED was added to the final solution. Stirring was continued for 20 minutes and the solution was left without disturbance for 2 hours. The mixture was centrifuged at 13000 rpm to collect the magnetic thermoresponsive nanocomposites (MTN) and washed several times with deionized water. MTN was dried in vacuum at room temperature for 24 hours and subsequently used for drug loading and further characterization.

2.4. Characterization

XRD pattern for SPIONs was obtained using an X-ray diffractometer (XRD, BRUKER Co. D8 ADVANCE-Germany) with CuKα radiation λ = 1.5418 Å. The crystallite size (T) of the sample was calculated by Scherrer equation (Equation 3) [24]; where β is the width of the peak at half maximum intensity for a specific plane with miller indices h, k, and l, whereas, C is the shape factor (taken as 0.9), λ is the wavelength of the incident X-ray and θ is the half angle between the incident and diffracted beams (2θ) in radians. The lattice parameter was calculated using Equation 4 [25]; where d hkl is the interplanar spacing, and a is the lattice parameter

$$T = \frac{C\,\lambda}{\beta \cos\theta} \tag{3}$$

$$d_{hkl}^{2} = \frac{a^{2}}{h^{2}+k^{2}+l^{2}} \tag{4}$$

FTIR spectra of SPIONs and magnetic thermoresponsive nanocomposite (MTN) samples, dispersed in KBr pellets, were obtained using FTIR (Nicolt 6700-USA) at 4 cm-1 resolution. The morphology of magnetic thermoresponsive nanocomposites (MTN) was studied using high transmission electron microscope (HRTEM, JEM-2100, JEOL-Japan). The elemental composition of magnetic thermoresponsive nanocomposite (MTN) was determined using EDX spectroscopy (OXFORD INCA Penta FETX3- England).

The polymer content in the magnetic thermoresponsive nanocomposite (MTN) was determined by thermogravimetric analyzer (TGA, SDT Q600 TA, USA) in the temperature range from room temperature to 850 °C at a heating rate of 10 °C min-1 under nitrogen atmosphere.

The LCST of PNIPAAm and MTN.5-AIQ was estimated using differential scanning calorimeter (DSC, SDT Q600 TA, USA) in the temperature range from 25 to 70 °C at a heating rate of 5 °C min-1 under nitrogen atmosphere. Whereas the turbidity test was performed on PNIPAAm solution with turbidimeter (HACH 2100N turbidimeter). Turbidity is measured in nephelometric turbidity unit (NTU) where, "nephelometric" describes an optical principle of instrumentation whereby turbidity is determined by measuring the amount of light scattered at some angle from the incident light path by particles suspended in the test solution. The scattered light by (0.625 mg/ml) PNIPAAm solution was measured for thermo-stated samples at various temperatures ranging from 25 to 50 °C.

The magnetization curves of magnetic nanoparticles (MNPs) and magnetic thermoresponsive nanocomposite (MTN) samples were obtained by applying the sample in powder form using vibrating sample magnetometer (VSM; 9600-1 LDJ, USA) at room temperature. The operation of a VSM is based on magnetizing the sample using a direct magnetic field and simultaneously forcing it to vibrate in the vicinity of pickup coils. Such vibration induces a voltage which alternates at the same frequency with a magnitude determined by the magnetization of the sample.

The potential of the magnetic core to produce heat via relaxation losses is assessed via calculation of the SAR values using an induction heater (DW-UHF-10 kW, China) at 198 kHz, and 9.4 kA/m). A fixed volume of the ferrofluid (4 ml of 3 and 7mg/ml solution of magnetite in water) was placed in a glass vial that was inserted in a Styrofoam jacket -as an insulator- and the temperature was measured by an alcohol thermometer. SAR was calculated by using Equation 5 [26]; where ci is the specific heat of water and glass vial that are 4.18 and $0.793\ JK^{-1}g^{-1}$ respectively, mi is the mass of water and glass vial; taken as 4 and 5.2758 grams respectively, $\frac{\Delta T}{\Delta t}$ is the initial slope of the time-dependent temperature curve and mSPION is the mass of SPIONs in the solution in grams.

$$SAR = \frac{\sum m_i c_i}{m_{SPION}} \frac{\Delta T}{\Delta t} \quad (5)$$

MTN was allowed to swell in various concentrations of 5-AIQ, sonicated for 15 minutes, and transferred to a shaking water bath in dark for 23 hours at room temperature. Drug loaded MTN (MTN.5AIQ) was separated from the solution by a strong magnet and the supernatant was analyzed by (HPLC, YOUNGLIN-9100, South Korea). Isocratic separation method was carried out according to the following conditions: RB18 column; mobile phase: acetonitrile 0.8%: acetic acid (6: 4); flow rate:1.5 ml/min; and peaks were separated at λ = 260 nm. The drug concentration was calculated using a calibration curve. The drug uptake by MTN and drug loading efficiency were calculated by Equation 6 and Equation 7 [20], respectively.

$$drug\ uptake\ = W_{feed}\ -\ W_{free} \quad (6)$$

$$drug\ loading\ efficiency\ = \frac{W_{feed} - W_{free}}{W_{feed}} \times 100 \quad (7)$$

Where, Wfeed the weight of drug in which the MTN swelled and Wfree, the weight of drug in the supernatant. To determine the temperature at which the maximum drug release occurred, MTN.5-AIQ sample was suspended in phosphate buffer saline (PH = 7.4) and incubated at different temperatures (35 up to 46 °C) for 30 min and the supernatant was analyzed by UV-visible spectrophotometer at a wavelength range from 200 to 250 nm. The released drug concentrations were determined by calculating the area under the peak from 200 to 232 nm.

2.6. Biocompatibility and toxicological parameters

Male Swiss albino mice (weighing ~ 25–31 g) were kept at animal facility of Faculty of Science, Ain Shams University. The animals were housed in an air-conditioned facility with a 12-h light/dark cycle, allowed free access to food and water. Mice were humanely treated in accordance with the ARRIVE guidelines for animal care. All experimental procedures were approved by the Ain Shams University Research Ethics Committee.

Fifteen mice were randomly divided into three groups. The first group was intraperitoneally injected with saline and served as sham-operated control, the second one administered a single dose of cisplatin (15mg/kg) as a positive control (cisplatin-treated group). The last group administered a single intraperitoneal injection of (MTN.5-AIQ) (5mg/Kg). All mice were then euthanized, and blood samples were collected from the heart and sera form different groups were separated by centrifugation (1500/10 min) and kept at −20 ˚C until the time of analysis. The kidney and liver tissue samples were collected and fixed in 10% buffered neutral formalin for further histopathological studies.

2.6.1. Kidney and liver functions

Renal functions were evaluated by measuring serum creatinine and uric acid according to manufacturer's instructions using commercial calorimetric kits (Bio-diagnostic Co., Cairo, Egypt). Hepatic functions were evaluated by measuring serum glutamic oxaloacetic transaminase (GOT) and glutamic pyruvic transaminase (GPT) according to manufacturer's instructions (Bio-diagnostic Co., Cairo, Egypt).

2.6.2. Histological examinations

Kidney and liver samples obtained from different experimental groups were fixed in 10% buffered neutral formalin. The samples were then routinely dehydrated in graded series of ethanol, cleared in xylol and mounted in molten Paraplast at 58–62 ℃. Paraffin sections of about 4 ± 5 μm were obtained, stained with H&E stain [27] and examined under light microscope (LICA, German, provided with HD camera).

2.7. Cell culture and MTT assay

Cryopreserved Caco-2 cells were cultured in a humidified atmosphere (5% CO2, 37 ℃) with RPMI-1640 Medium supplemented with 2% fetal bovine serum (FBS) and 50 μg/mL gentamycin. Cells were passaged at 80–90% confluency after trypsinization with pre-warmed trypsin-EDTA solution. The cytotoxicity of 5-AIQ, MTN and MTN.5-AIQ.4 samples was investigated on Caco-2 cell lines by cell viability MTT assay. The experiment was conducted for determination of the IC50 (the concentration of the drug which causes 50% cell death). The selected samples were two-fold diluted in culture media. Cells were treated with 100 μl of each sample and incubated for further 24 hours. Then, 20 μl of MTT solution were added to each well and incubated for 1–5 hours. Finally, the produced formazan was dissolved in 200 μl DMSO and the mean absorbance of three replicates was measured at 570 nm.

2.8. Statistical analysis

All values are presented as means ± SE. Statistical analysis of experimental data was performed using a

one-way analysis of variance (ANOVA) followed by Donnett's multiple comparison test for comparing means from different treatment groups.

3. Results and discussion

3.1. Structure and morphology

The X-ray diffraction (XRD) pattern of the iron oxide core is shown in Figure 1A. The obtained pattern shows a face centered cubic (FCC) structure, the peaks positioned at 2θ = 29.942 °, 35.386 °, 43.123 °, 57.019 ° and 62.581 ° correspond to reflections from the planes; (220), (311), (400), (511) and (440) respectively [28]. These positions and their relative intensities are consistent with ICDD 89 0688 card [28] which confirms that the synthesized particles are single phase magnetite or maghemite. The calculated average crystallite for the obtained SPIONs size is 12.7 nm and the average lattice parameter is 8.3992 Å.

The Fourier transform infrared spectroscopy (FTIR) spectrum of SPIONs is shown in Figure 1B (lower plot in black). The SPIONs sample exhibits one intense peak at 550 cm-1 due to stretching vibration mode associated with the metal-oxygen absorption band (Fe–O bonds) in the Fe3O4 sample [29]. There are less intense peaks at 1632 and 865 cm-1 resulting from the bending vibration of the O–H in plane and out of plane bonds of water respectively [30] in addition to a broad peak centered at 3377 cm-1 due to the O-H bond stretching vibrations of water [31]. FTIR spectrum of SPION-PNIPAAm sample is also shown in Figure 1B (upper plot in red). The spectrum illustrates the characteristic peaks of Fe3O4 and PNIPAAm. The peak at 550 cm-1 represents Fe-O bond with no observed shift because the SPION-PNIPAAm is prepared after the magnetite is synthesized (post synthesis polymerization). The characteristic peaks at 1545 cm-1 and 1650 cm-1 represent the amide II (NH bending) and amide I (C=O stretching) vibrational mode found in PNIPAAm respectively, the peaks at 1365 and 1395 cm-1 arise from bending vibration of isopropyl group -CH(CH3)2 found in PNIPAAm, the peak at 3300 cm-1 corresponds to secondary N-H amide symmetric stretching vibration [32], the peaks at 2972 cm-1 and 1460 cm-1 correspond to (C-H) stretching and bending vibration respectively [31], the peak at 1245 cm-1 corresponds to (C-N) bending vibration found in PNIPAAm [33].

High resolution transmission electron microscope (HRTEM) analysis shows the size and morphology of MTN. TEM micrograph of MTN in Figure 1C reveals the spherical shape of MTN with core shell structure. The MNPs appears as dark spots coated with PNIPAAm that constitutes the grayish layer as clarified by the arrows. The observed aggregation of the particles is a consequence of imaging under high vacuum conditions. The average diameter of SPIONs was estimated with automated size distribution analysis software (image J). The size distribution curve of SPIONs obtained from TEM micrographs is shown in Figure 1D. The SPIONs diameter was determined to be 11.03 nm, which is consistent with the size obtained from XRD data, suggesting each particle is a single crystal. Moreover, the statistical analysis of the particles reveals the narrow size distribution of the nanoparticles (5–20 nm). Selected area electron diffraction pattern is shown in Figure 1E. Peak indexing was performed using Equation 8 [34]; where d is the interplanar spacing, Rr is the ring radius, Lf is the camera focal length, λ is the wavelength of electron and V is 200 kV (Equation 9).

$$d = \frac{\lambda}{R_r} L_f \tag{8}$$

where,

$$\lambda = \sqrt{\frac{1.505}{V}} \tag{9}$$

For the (311) plane, the calculated d-value from SAED, XRD and standard d-values in literature [20] are 2.5340, 2.53454 and 2.53 (Å) respectively which confirms the face centered cubic structure of SPIONs.

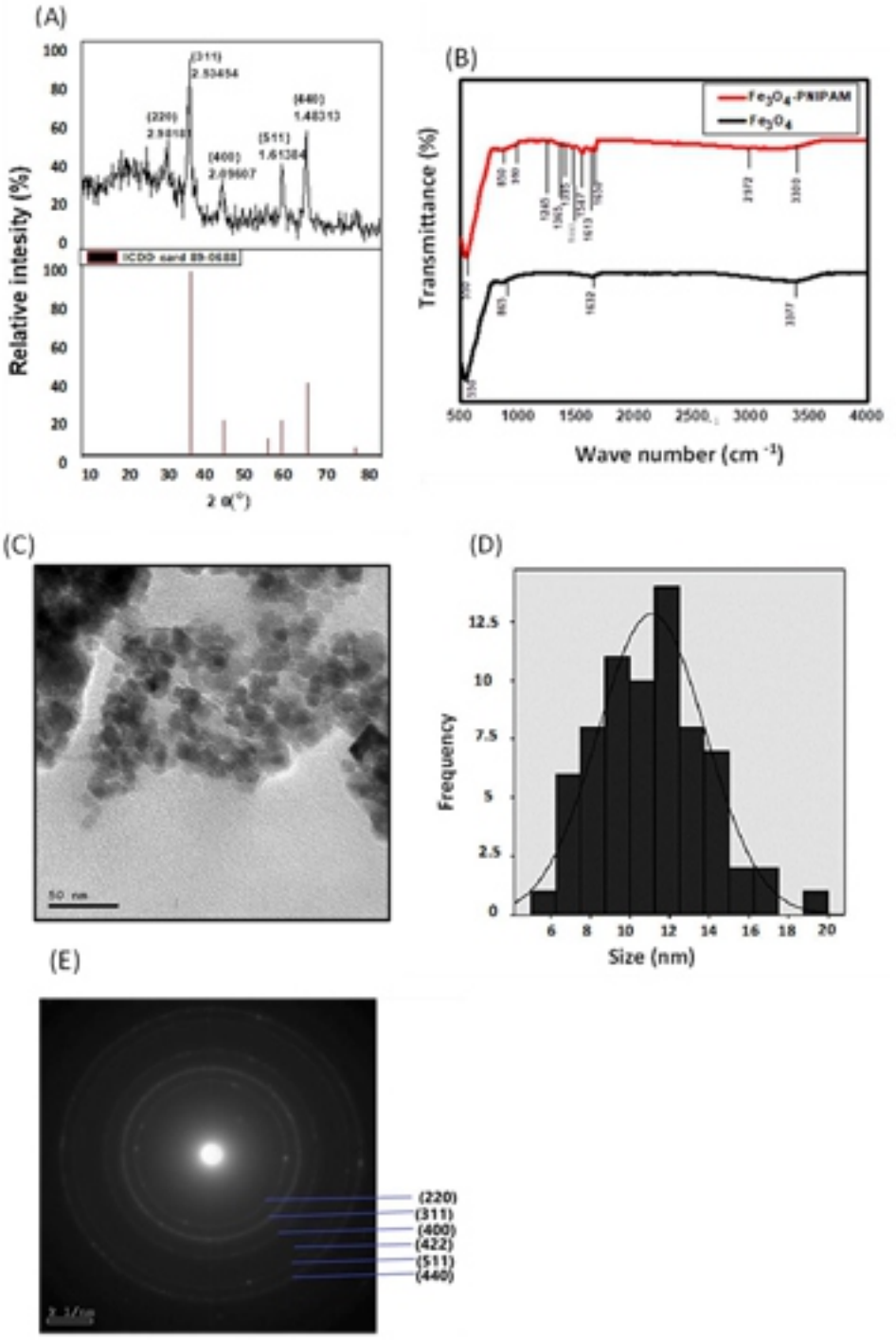

Figure 1. (A) X-ray diffraction pattern for SPIONs, (B) FTIR spectra for SPIONs (lower curve) and SPIONs-PNIPAAm (MTN) (upper curve). (C) TEM micrograph for SPIONs-PNIPAAm (MTN), (D) size distribution histogram for SPIONs, (E) SAED pattern of MTN.

Energy dispersive X-ray (EDX) spectrum of MTN is shown in Figure 2A. The major peaks of Fe at 0.7, 6.3, 7 keV correspond to the binding energy of Fe (Lα ,Kα and Kβ respectively) [35]. The presence of nitrogen peaks confirms the coating of SPIONs with the Poly(N-isopropylacrylamide) [36].

The polymer content of magnetic thermoresponsive nanocomposite (MTN) was determined using TGA analysis. TGA thermogram estimates the weight loss occurring in the sample upon increasing the temperature from room temperature to 850 °C as shown in Figure 2B. The thermogram shows that weight loss occurred in two steps; one below 200 °C due to loss of water, the other occurred in the range from 200 to 600 °C. The latter loss was attributed to the degradation of the side chain functional group and back bone structure of the -PNIPAAm [22]. The results show that the amount of PNIPAAm in MTN is 5.08%.

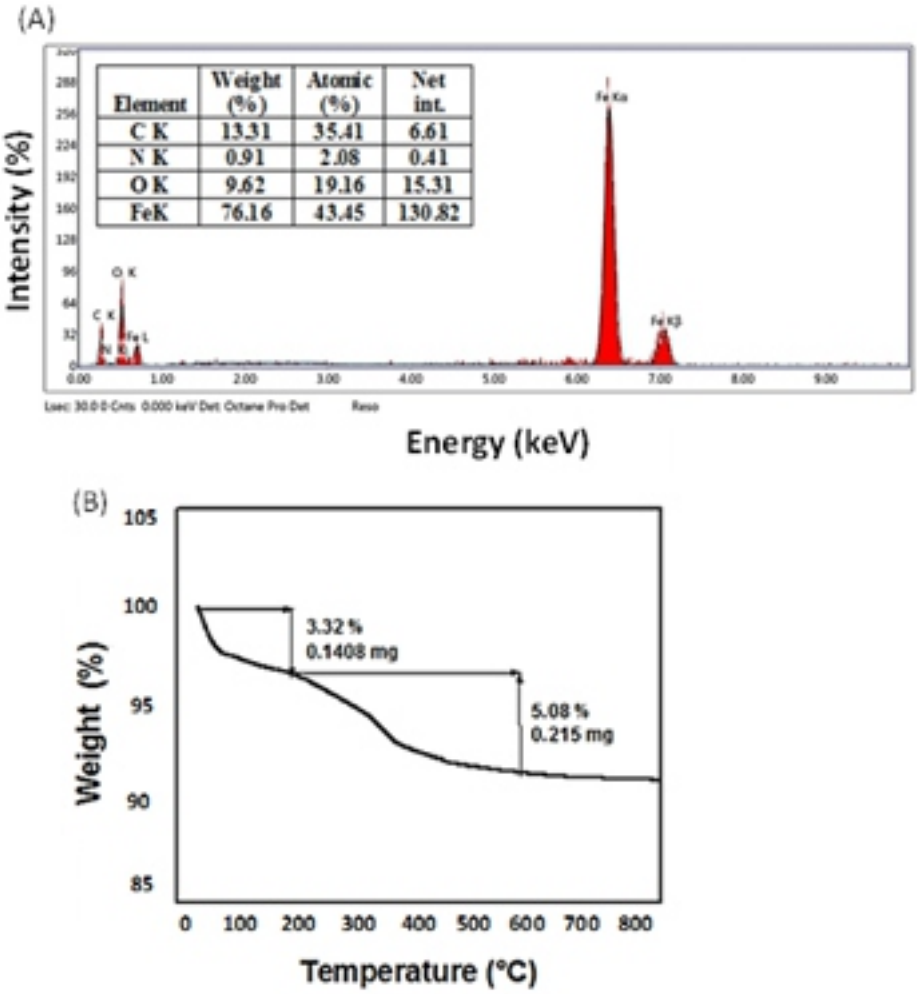

Figure 2. (A) EDX pattern for SPIONs-PNIPAAm (MTN). (B) TGA thermogram of the magnetic thermoresponsive nanocomposite (MTN).

3.2. Thermal response

The coil to globule transition was assessed via two methods: DSC (a thermal method) and turbidimetry (an optical method). DSC was used to determine the LCST for the polymer alone and for MTN.5-AIQ and the thermograms are shown in Figure 3A, B. The LCST in each case can be determined in different ways; either from the tangent drawn at the onset of depression (44.5 °C for PNIPAAm and 43.5 °C for MTN.5AIQ) or the tangent along the curve (48 °C for PNIPAAm and 47 °C for MTN.5 - AIQ, or the peak point (46.72 °C for PNIPAAMm or 44.5 °C for MTN.5-AIQ).

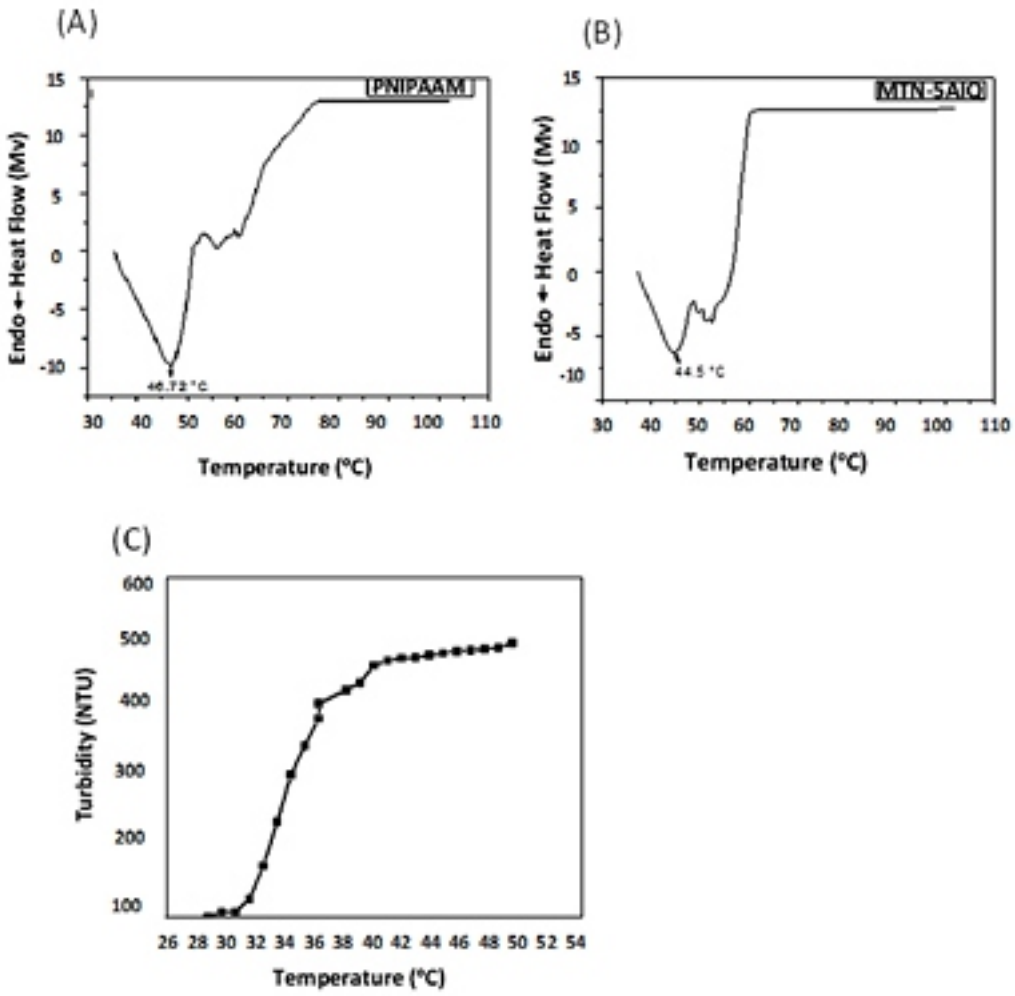

Figure 3. (A) and (B) DSC of PNIPAAm and MTN.5-AIQ, respectively showing the phase transition temperature of the nanocomposites. (C) Turbidity test for PNIPAAm showing the Tcp of the polymer.

As for turbidimetry, the cloud point temperature (Tcp) indicates the collapse and aggregation of the soluble polymer leading to clouding of the solution. Figure 3C shows turbidity as a function of temperature for PNIPAAm. It is worth noting that, the turbidity test (based on light transmission) cannot be conducted for samples containing iron oxide as a major constituent. The results show that, as the temperature increases, the turbidity of PNIPAAm increases. As is the case for LCST data, there is no consent about the point on the curve at which Tcp is determined [37]. Therefore, Tcp is considered to lie in the range between 31 to 41 °C for PNIPAAM. The difference in the obtained values of LCST and Tcp for NIPAAM is physically accepted as the principles for obtaining them are different.

A wide range of transition temperature values have been reported in literature. The most common value was between 30–34 °C according to Priya James et al., 2014 [1], and Ward& Georgiou, 2011 [2]. Higher values have been also reported by (Xia et al., 2006). The study showed that Tcp for PNIPAAm decreased from 45.3 °C to 34.4 °C upon increasing the molecular weight with a sharper transition [38].

3.3. Magnetic and specific absorption rate (SAR) measurements of magnetic core

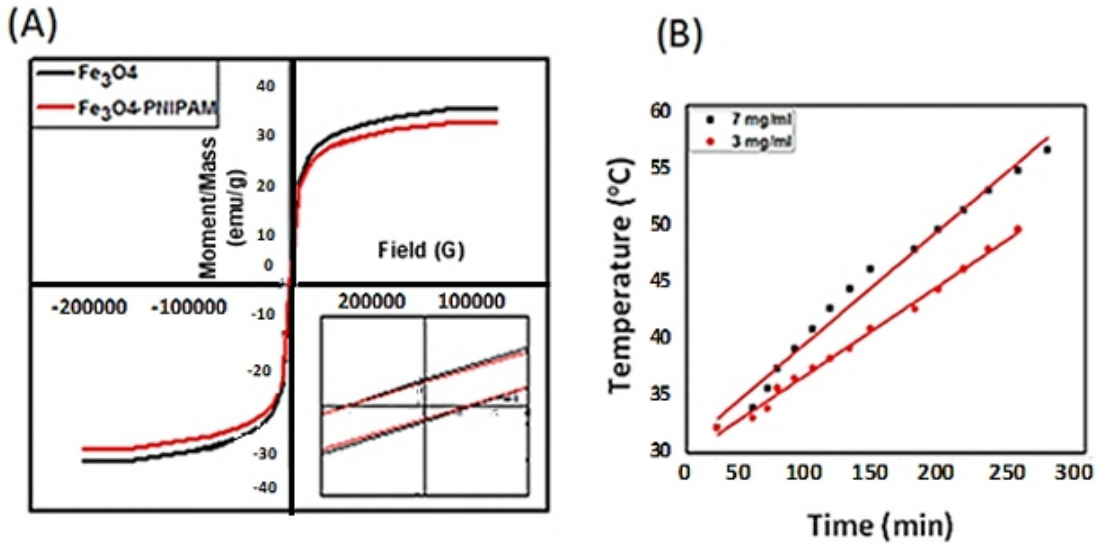

Figure 4. (A) Magnetization curves of SPIONs and MTN with inset showing the vanishingly small value of coercivity (B) Temperature time curve for SPIONs ferrofluids with two concentrations; 3mg/ml and 7 mg/ml; showing the initial (linear) rise.

The magnetization curve of SPIONs is shown in Figure 4A. The curve reveals the superparamagnetic behavior of iron oxide nanoparticles at room temperature with inconspicuous value of remnant magnetization. The saturation magnetization of SPIONs is 35.412 emu/g which is less than the saturation magnetization of bulk magnetite (92 emu/gm) and (74–80 emu/gm) of maghemite [39]. The result is consistent with the fact that the saturation magnetization decreases with size. As the particle size decreases, the surface to volume ratio increases and in turn, the magnetically dead layer fraction increases because of the canted and disordered spins on the surface of the nanoparticles [40]. Likewise, the coercivity decreases with decreasing size below the critical size, which is consistent with previous theoretical estimations [41]. The low values of coercive field (36.3 G) and remanent magnetization (0.93694 emu/g) unveil that the sample is superparamagnetic at room temperature. Slightly lower value of saturation magnetization (32.74 emu/g) is obtained for MTN due to the nonmagnetic polymer layer. It is worth noticing that the decrease in magnetization is consistent with the contribution of PNIPAAm in the MTN structure as obtained from the TGA analysis. Coercive field and remanent magnetization are 34.522 G and 0.83349 emu/g respectively; denoting a Assessment of specific absorption rate of SPIONs was performed by exposing the sample to alternating magnetic field (AMF) of strength equal to 9.4 kA/m and frequency of 198 kHz obtained by the induction heater. Figure 4B shows the temperature rise with time curve for two concentrations of SPIONs colloid (3 and 7 mg/ml) exposed to AMF. The field intensity and the operating frequency are within the acceptable range; ensuring compliance with the safety regulations for respective clinical application [26]. The calculated SAR values for the two-colloid concentrations (3 and 7 mg/ml) are 70.69 and 78.91 W/g respectively. This minor increase of SAR values upon increasing the concentration has been reported in literature [42] as being attributed to increasing the magnetic dipolar interactions between the particles. Even at the low concentration (3mg/ml), the therapeutic temperature (42 °C) was reached after only 4 minutes of exposure. The results proof the efficiency of the Magnetic thermoresponsive nanocomposite (MTN) as a MFH agent.

3.4. Drug loading and release kinetics

Table 1. Drug uptake and drug loading efficiency of MNC.5-AIQ samples.

Samples	Free drug (mg)	Feed drug (mg)	Drug uptake (mg)	Drug loading efficiency (%)
MNN.5-AIQ.1	1.6	5	3.4	68
MNN.5-AIQ.2	2.4	10	7.6	76
MNN.5-AIQ.3	6.268	20	13.732	68.67
MTN.5-AIQ.4	4.284	30	25.716	85.72

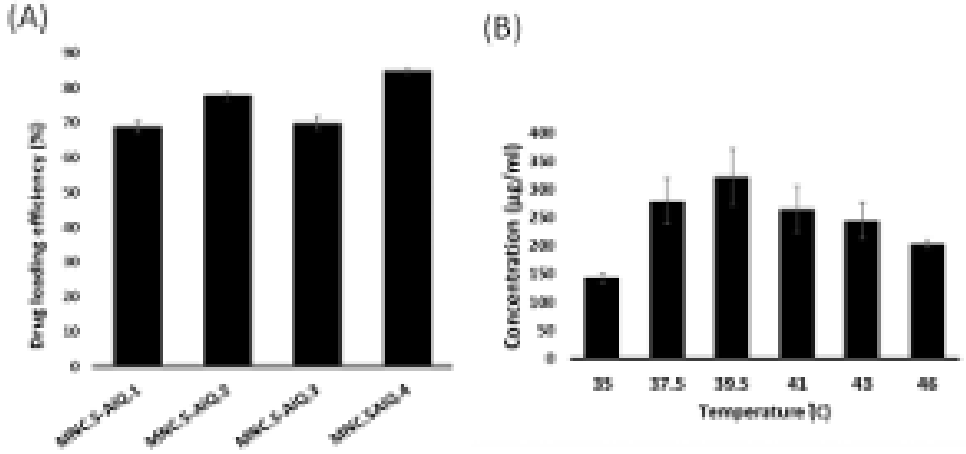

Figure 5. (A) Drug loading efficiency of MTN.5-AIQ samples, (B) 5-AIQ release profile of MTN.5-AIQ.4 nanoparticles incubated at different temperatures. Value represents the mean ± SEM. 5-AIQ; 5-aminoisoquinoline, MTN.5-AIQ; magnetic thermoresponsive nanocomposite loaded with 5-aminoisoquinoline.

Magnetic thermoresponsive nanocomposite (MTN) sample was loaded with 5-aminoisoquinoline (5-AIQ) by resuspension of MTN in four different concentrations of the drug as listed in Table S1. MTN.5-AIQ samples were separated by a strong magnet then the residual concentration of 5-AIQ in the supernatants were quantified using HPLC analysis. The HPLC chromatogram of 5-AIQ is shown in Figure S1A. Table 1 illustrates the value of drug loading efficiency of the samples and Figure 5A illustrates the results. It was noticed that the drug loading efficiency increased as the concentration of feed drug increased and sample MTN.5-AIQ.4 has the highest drug loading capacity. Based on these results, the drug release kinetics were studied for sample, MTN.5-AIQ.4 only.

After incubation of MTN.5-AIQ.4 sample at temperatures of 35, 37.5, 39.5, 41, 43 and 46 °C for 30 minutes, the solution was separated by a strong magnet and the supernatant was analyzed by a UV-visible spectrophotometer. As shown in Figure 5B, the drug release was assessed at different temperatures and the maximum release of the 5-AIQ was at 39.5 °C. In addition, Figure S1B displays the drug release concentration at various temperatures analyzed by HPLC, which supports the findings obtained using UV-spectrophotometer and confirms that the maximum amount of drug is released at hyperthermia within the acceptable therapeutic range.

3.5. Biocompatibility and toxicological parameters

3.5.1. Kidney and liver functions

Serum levels of creatinine, uric acid, glutamic pyruvic transaminase (GPT) and glutamic oxaloacetic transaminase (GOT) were evaluated for the control, cisplatin-treated and MTN.5-AIQtreated groups. Cisplatin impaired the renal function as is apparent from the significantly higher serum creatinine level ($p < 0.05$) compared with the control as shown in Figure 5A. the renal dysfunction induced by cisplatin was previously depicted in literature [43]. The serum creatinine and uric acid levels of the MTN.5-AIQ treated group, however, are not significantly different from those of the control group as illustrated in Figure 6A & B; proving the biocompatibility of MTN.5-AIQ. The significant elevation of serum level ($P < 0.05$) of GPT for the cisplatin group compared to control refers to the hepatotoxicity of cisplatin. On the other hand, the administration of MTN.5-AIQ did not produce any significant changes in liver function compared to the control as shown in Figure 6 C & D. This result proves the biocompatibility of MTN.5-AIQ.

3.5.2. Histopathology examination

Upon cisplatin administration, a marked congestion and atrophy of glomeruli are observed in mice kidneys of cisplatin–treated group compared to normal, Figure 6E (a-c). Furthermore, liver histopathological abnormalities are detected, marked by swelling and vascular degeneration in hepatocytes, Figure 6E (i-j) comparable with normal control. These observations confirm the nephrotoxicity and hepatotoxicity of cisplatin [43]. In MTN.5-AIQ-treated group, normal renal and collecting tubules are shown in Figure 6E (e-f), only slight congestion can be detected in the interstitial blood vesicles. As for hepatotoxicity examination, the livers of MTN.5-AIQ-treated mice show normal histopathological pictures with slight congestion in portal veins with normal bile ductuli (Figure 6E. k). Such results supporting the biocompatibility of MTN.5-AIQ encouraged by undetectable toxicity of the examined organ applied for histological study.

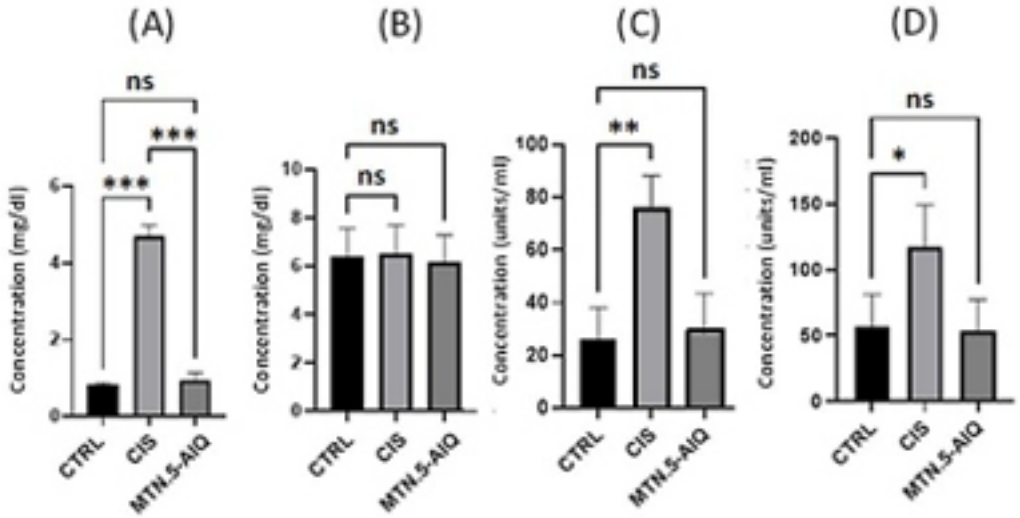

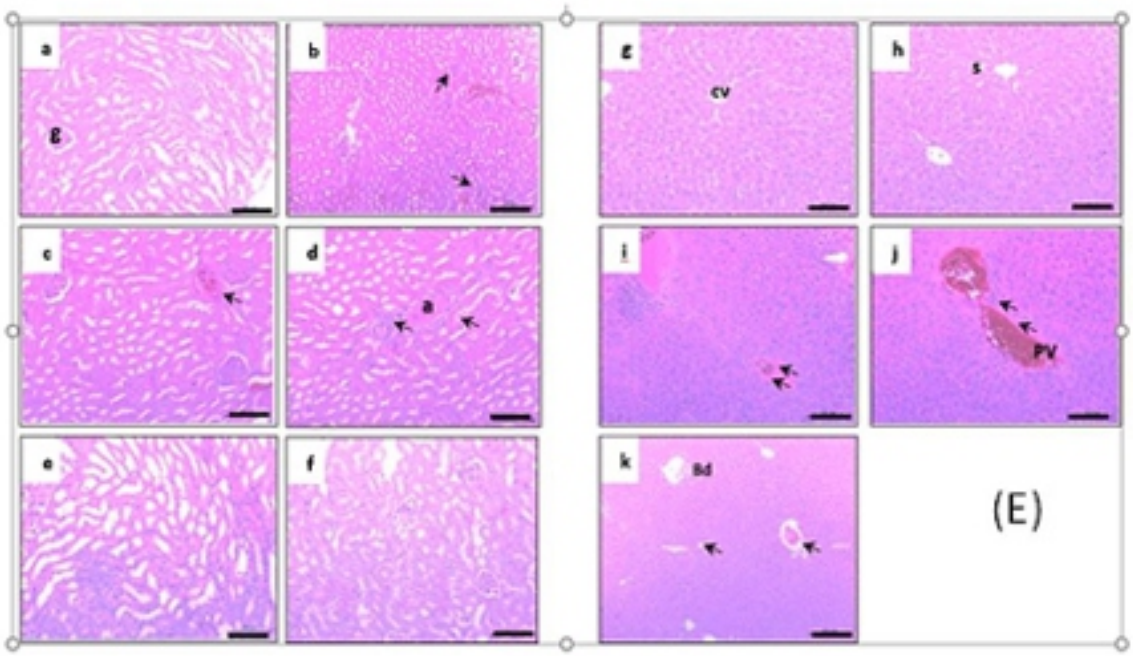

Figure 6. Effect of CIS (dose = 15 mg/kg) and MTN.5-AIQ (dose = 5mg/kg) on kidney and liver functions: Serum (A) creatinine, (B) uric acid, (C) glutamic pyruvic transaminase (GPT) and (D) glutamic oxalic transaminase (GOT) were evaluated for the three experimental groups; CTRL, CIS and MTN.5-AIQ. Each value represents the mean ± SEM (n=5 mice per group), *significantly different versus control group (CTRL) ($P < 0.05$), ** significantly different versus control group ($P < 0.005$), ****significantly different versus control group ($P < 0.0001$). (E) Effect of CIS (dose = 15 mg/kg) and MTN.5-AIQ (dose=5mg/kg) on histopathological changes in kidneys and livers: (a) normal control of mouse kidney. (b-d) Pronounced histopathological abnormalities are seen in mice treated with cisplatin (15 mg/kg body weight). (b) Congestion and partial atrophy of glomeruli in the cortex, (c) congestion and mild tubular degeneration in the cortico- medullary junction, (d) congestion and perarterial leucocytic aggregation in the medullary portion of the kidney (marked by black arrows). (e) Normal renal tubules in the cortico-medulry iunction and normal collecting tubules (f) normal renal cortex be observed in the kidney of the MTN.5-AIQ-treated group. (G&H) normal hepatic cords with normal hepatocytes in control group. (i&j) Pronounced histopathological abnormalities are seen in mice treated with cisplatin (15 mg/kg body weight. (I) Swelling and mild vascular degeneration in hepatocytes, (j) congestion of both central and portal vein together with mononuclear aggregation (marked by black arrows). (k) Liver of MTN.5-AIQ-treated mice shows nearly normal hepatic cords with normal hepatocytes and sinusoids. Scale bar=100µm. CTRL; control, CIS: cisplatin, MTN.5-AIQ; magnetic thermoresponsive nanocomposite loaded with 5-aminoisoquinoline.

3.6. Cytotoxic effect of MTN.5-AIQ on colon adenocarcinoma

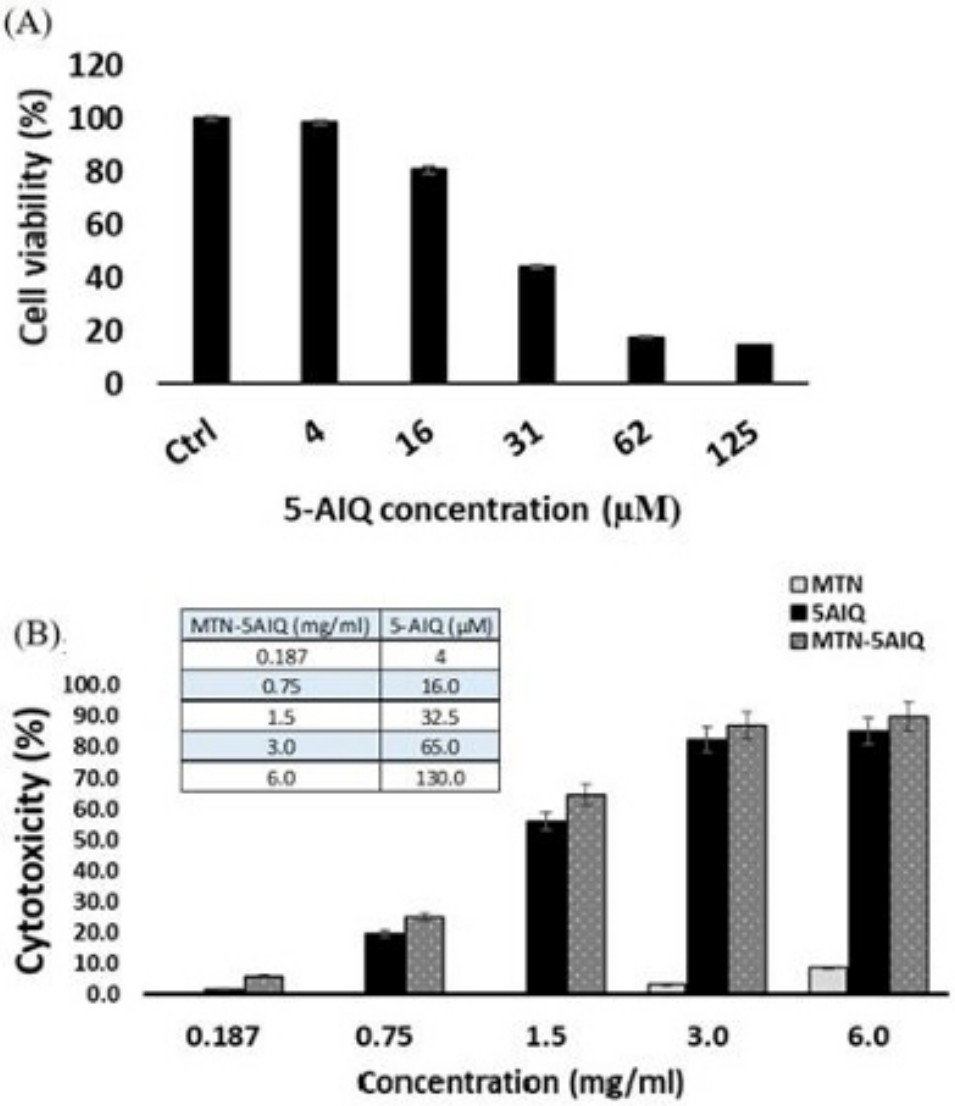

Figure 7. (A) IC50 value of 5-AIQ-induced Cytotoxicity on colon adenocarcinoma (Caco-2) cell. (B) Cytotoxicity measurement of MTN and MTN.5-AIQ on Caco-2 cells; Caco-2 cells were incubated with different doses of either MTN unloaded or loaded composites. Twenty four hours later, cell viability was determined via MTT assay. MTN; magnetic thermoresponsive nanocomposite, MTN.5-AIQ; magnetic thermoresponsive nanocomposite loaded with 5-aminoisoquinoline.

The effect of different 5-AIQ concentrations on Caco-2 cells is illustrated in Figure 7A. The cytotoxicity of MTN and MTN.5-AIQ was studied on Caco-2 cells as shown in Figure 7B. No significant cytotoxicity is induced by MTN on Caco-2 cells up to 6 mg/ml (stock solution). Upon further increasing the concentration of MTN, the cytotoxicity of MTN increased. Chang et al investigated the cytotoxicity of SPIONs nanoparticles on BHK-21 cells and concluded that, there was no cytotoxic effect of iron at a concentration up to 100 µg/mL incubated for 24 h [44]. It was accepted that below a concentration of 5 mg/ml concentration of PNIPAM polymer did not affect the cell survival. Such sublethal dose range was investigated by Vihola and his colleagues on two human cell

The effect of different 5-AIQ concentrations on Caco-2 cells is illustrated in Figure 7A. The cytotoxicity of MTN and MTN.5-AIQ was studied on Caco-2 cells as shown in Figure 7B. No significant cytotoxicity is induced by MTN on Caco-2 cells up to 6 mg/ml (stock solution). Upon further increasing the concentration of MTN, the cytotoxicity of MTN increased. Chang et al investigated the cytotoxicity of SPIONs nanoparticles on BHK-21 cells and concluded that, there was no cytotoxic effect of iron at a concentration up to 100 μg/mL incubated for 24 h [44]. It was accepted that below a concentration of 5 mg/ml concentration of PNIPAM polymer did not affect the cell survival. Such sublethal dose range was investigated by Vihola and his colleagues on two human cell lines; intestinal Caco-2 cell line and bronchial Calu-3 [45]. As shown in the present results, hyperthermia studies proved that low concentrations of SPIONs, around 3 mg/ml, can cause significant rise in temperature in a very short time; the phenomenon that trigger the 5-AIQ release (65 μM). These two factors; hyperthermia and thermally triggered-drug release are aimed to play synergistic effects in treatment of metastatic colon cancer without any aggravated response toward healthy tissues. comparison to 5-AIQ alone, the MTN-5AIQ effectively increase the therapeutic levels of 5-AIQ inside the cells as indicated the elevated cytotoxicity.

4. Conclusions

In this work, the smart nanocomposite (MTN.5-AIQ) was successfully prepared with superior properties. The high therapeutic temperature could be attained with considerably low concentration of SPIONs representing the magnetic core of the composite. Moreover, the polymeric shell showed high efficiency in drug uptake with convenient release kinetics at the therapeutic temperature range. Finally, MTN.5-AIQ showed good in vivo biocompatibility whereas, it caused antineoplastic effect for Caco-2 cell lines. The key mechanism beyond this synergy includes the blockage of PARylation-dependent DNA repair pathway as well as impairment of metabolic adaptation of cancer cell by virtue of PARP inhibition combined with hyperthermia. The uniqueness of MTN.5-AIQ over other anti-cancer approaches can be attributed to its selectivity.

These findings render the genuine loading of 5-AIQ on a thermoresponsive nanocomposite a promising candidate of magnetic-based hyperthermia-PARP inhibition dual therapy for colon adenocarcinoma. On limitation of our study was the design of an appropriate in vivo cancer model for further examination of MTN-5AIQ anti-cancer effects and further efforts are continued in the future. Upcoming work will focus on attempting to leverage the efficacy of magnetic thermoresponsive nanocomposites-loaded with different immunotherapies that are routinely used for treatment of resistance cancers.

Acknowledgements

Magnetic and SAR measurements were conducted at Cyclotron Project, Nuclear Research Center, Egyptian Atomic Energy Authority, Egypt by Dr. Ismaeel Abdulrahim.

Conflicts of interest

On behalf of all authors, the corresponding author states that there is no conflict of interest. Funding: The author(s) declared that no grants were involved in supporting this work. All in vivo experiments were conducted according to (ARRIVE) guidelines for animal care. All animal experiments were approved by the Ain Shams University Research Ethics Committee. The preliminary version of this

work was posted in Research Square server as a preprint [46]. Availability of data and material: Additional datasets used in the present work are available from the corresponding author upon request.

Author contributions:

Conceptualization: AAG, TE, HK; EME; data curation: AAG, HK; formal analysis: AAG, TE, HK; funding acquisition: AAG, TE, HK; investigation: AAG, TE; methodology: AAG, TE, HK; writing original draft preparation: AAG, EME; writing/review and editing: all authors. All authors read and approved the final manuscript.

References

1. James HP, John R, Alex A, et al. (2014) Smart polymers for the controlled delivery of drugs–a concise overview. Acta Pharm Sin B 4: 120–127. https://doi.org/10.1016/j.apsb.2014.02.005

2. Ward MA, Georgiou TK (2011) Thermoresponsive polymers for biomedical applications. Polymers (Basel) 3: 1215–1242. https://doi.org/10.3390/polym3031215

3. Gould P (2006) Nanomagnetism shows in vivo potential. Nano Today 1: 34–39. https://doi.org/10.1016/S1748-0132(06)70115-3

4.Abenojar EC, Wickramasinghe S, Bas-Concepcion J, et al. (2016) Structural effects on the magnetic hyperthermia properties of iron oxide nanoparticles. Prog Nat Sci Mater Int 26: 440448. https://doi.org/10.1016/j.pnsc.2016.09.004

5.Sharifi I, Shokrollahi H, Amiri S (2012) Ferrite-based magnetic nanofluids used in hyperthermia applications. J Magn Magn Mater 324: 903–915. https://doi.org/10.1016/j.jmmm.2011.10.017

6.Ba XQ, Garg NJ (2011) Signaling mechanism of poly(ADP-ribose) polymerase-1 (PARP-1) in inflammatory diseases. Am J Pathol 178: 946–955. https://doi.org/10.1016/j.ajpath.2010.12.004

7.Virág L, Szabó C (2002) The therapeutic potential of poly (ADP-ribose) polymerase inhibitors. Pharmacol Rev 54: 375–429. https://doi.org/10.1124/pr.54.3.375

8.D Threadgill M (2015) 5-Aminoisoquinolin-1-one (5-AIQ), a water-soluble inhibitor of the poly(ADP-Ribose)polymerases (PARPs). Curr https://doi.org/10.2174/092986732266615100211060 2

9. Med Chem 22: 3807–3829. Vinod KR, Chandra S, Sharma SK (2010) Evaluation of 5-aminoisoquinoline (5-AIQ), a novel PARP-1 inhibitor for genotoxicity potential in vitro and in vivo. Toxicol Mech Methods 20: 9095. https://doi.org/10.3109/15376510903572870

10. Romano B, Pagano E, Iannotti FA, et al. (2021) N-Acylethanolamine acid amidase (NAAA) is dysregulated in colorectal cancer patients and its inhibition reduces experimental cancer growth. Brit J Pharmacol 1–16. https://doi.org/10.1111/bph.15737

11. Pagano E, Venneri T, Lucariello G, et al. (2021) Palmitoylethanolamide reduces colon cancer cell proliferation and migration, influences tumor cell cycle and exerts in vivo chemopreventive effects. Cancers (Basel) 13: 1923. https://doi.org/10.3390/cancers13081923

12. Pagano E, Borrelli F, Orlando P, et al. (2017) Pharmacological inhibition of MAGL attenuates experimental colon carcinogenesis. https://doi.org/10.1016/j.phrs.2017.02.002 of Pharmacol Res 119: 227–236.

13. Toğaçar M (2021) Disease type detection in lung and colon cancer images using the complement approach inefficient sets. Comput https://doi.org/10.1016/j.compbiomed.2021.104827 Biol Med 137: 104827.

14. Raftery L, Goldberg RM (2010) Optimal delivery of cytotoxic chemotherapy for colon cancer.

Cancer J 16: 214–219. https://doi.org/10.1097/PPO.0b013e3181ddc5ac flavonoids
15. Fernández J, Silván B, Entrialgo-Cadierno R, et al. (2021) Antiproliferative and palliative activity of in colorectal cancer. https://doi.org/10.1016/j.biopha.2021.112241 Biomed Pharmacother 143: 112241.
16. Küpeli Akkol E, Genç Y, Karpuz B, et al. (2020) Coumarins and coumarin-related compounds in pharmacotherapy of cancer. Cancers (Basel) 12: 1959. https://doi.org/10.3390/cancers12071959
17. Ahmed S, Khan H, Aschner M, et al. (2020) Anticancer potential of furanocoumarins: mechanistic and therapeutic aspects. Int J Mol Sci 21: 5622. https://doi.org/10.3390/ijms21165622
18. Nosho K, Yamamoto H, Mikami M, et al. (2006) Overexpression of poly(ADP-ribose) polymerase-1 (PARP-1) in the early stage of colorectal carcinogenesis. Eur J Cancer 42: 23742381. https://doi.org/10.1016/j.ejca.2006.01.061
19. Augustine T, Maitra R, Zhang J, et al. (2019) Sensitization of colorectal cancer to irinotecan therapy PARP inhibitor rucaparib. Invest New Drug 37: 948–960. https://doi.org/10.1007/s10637-018-00717-9
20. Zhang J, Misra RDK (2007) Magnetic drug-targeting carrier encapsulated with thermosensitive smart polymer: core-shell nanoparticle carrier and drug release response. Acta Biomater 3: 838850. https://doi.org/10.1016/j.actbio.2007.05.011
21. Hegazy M, Zhou P, Wu G, et al. (2017) Construction of polymer coated core-shell magnetic mesoporous silica nanoparticles with triple responsive drug delivery. Polym Chem 8: 5852–5864. https://doi.org/10.1039/C7PY01179B
22. Purushotham S, Ramanujan RV (2010) Thermoresponsive magnetic composite nanomaterials for multimodal cancer therapy. https://doi.org/10.1016/j.actbio.2009.07.004
23. Meerod S, Rutnakornpituk B, Wichai U, et al. (2015) Hydrophilic magnetic nanoclusters with thermo-responsive properties and their drug controlled release. J Magn Magn Mater 392: 83–90. https://doi.org/10.1016/j.jmmm.2015.05.022
24. Sharma R, Bisen DP, Shukla U, et al. (2012) X-ray diffraction: a powerful method of characterizing nanomaterials. Recent Res Sci Technol 4: 77–79.
25. Suryanarayana C, Norton MG (2013) X-ray diffraction: A practical approach. Springer Science & Business Media.
26. Spirou SV, Basini M, Lascialfari A, et al. (2018) Magnetic hyperthermia and radiation therapy: Radiobiological principles and https://doi.org/10.3390/nano8060401
27. Page DL (1983) Theory and Practice of Histological Techniques. https://doi.org/10.1016/S00468177(83)80171-3
28. Wang B, Wei Q, Qu S (2013) Synthesis and characterization of uniform and crystalline magnetite nanoparticles via oxidation-precipitation and modified co-precipitation methods. Int J Electrochem Sci 8: 786–3793.
29. Idris MI, Zaloga J, Detsch R, et al. (2018) Surface modification of SPIONs in PHBV microspheres for biomedical applications. Sci Rep 8: 7286. https://doi.org/10.1038/s41598-018-25243-9
30. Lopez JA, González F, Bonilla FA, et al. (2010) Synthesis and characterization of Fe3O4 magnetic nanofluid. Rev Latinoam Metal y Mater 30: 60–66.
31. Coates J (2000) Interpretation of infrared spectra, a practical approach. Encycl Anal Chem 1081510837. https://doi.org/10.1002/9780470027318.a5606
32. Omer M, Haider S, Park SY (2011) A novel route for the preparation of thermally sensitive core shell magnetic nanoparticles. Polymer 52: 91–97. https://doi.org/10.1016/j.polymer.2010.11.011
33. Narain R (2010) Engineered carbohydrate-based materials for biomedical applications: polymers, surfaces, dendrimers, nanoparticles, and hydrogels. https://doi.org/10.1002/9780470944349

34. Mohapatra S, Rout SR, Panda AB (2011) One-pot synthesis of uniform and spherically assembled functionalized MFe2O4 (M = Co, Mn, Ni) nanoparticles. Colloids Surfaces A Physicochem Eng Asp 384: 453–460. https://doi.org/10.1016/j.colsurfa.2011.05.001

35. Shindo D, Oikawa T (2013) Analytical Electron Microscopy for Materials Science. Springer Science & Business Media.

36. Mutharani B, Ranganathan P, Chen SM (2019) Highly sensitive and selective electrochemical detection of antipsychotic drug chlorpromazine in biological samples based on poly-Nisopropylacrylamide microgel. J https://doi.org/10.1016/j.jtice.2018.10.029

37. Osváth Z, Iván B (2017) The dependence of the cloud point, clearing point, and hysteresis of poly (N-isopropylacrylamide) on experimental conditions: The need for standardization of thermoresponsive transition determinations. Macromol Chem Phys 218: 1600470. https://doi.org/10.1002/macp.201600470

38. Xia Y, Burke NAD, Stöver HDH (2006) End group effect on the thermal response of narrow disperse poly(N-isopropylacrylamide) prepared by atom transfer radical polymerization. Macromolecules 39: 2275–2283. https://doi.org/10.1021/ma0519617

39. Shokrollahi H (2017) A review of the magnetic properties, synthesis methods and applications of maghemite. J Magn Magn Mater 426: 74–81. https://doi.org/10.1016/j.jmmm.2016.11.033

40. Khairy M (2013) Synthesis, characterization and magnetic properties of gamma irradiated and unirradiated magnetic nanopowders. Int J Mater Chem 3: 106–111. https://doi.org/10.5923/j.ijmc.20130305.04

41. Li Q, Kartikowati CW, Horie S, et al. (2017) Correlation between particle size/domain structure and magnetic properties of highly crystalline Fe3O4 nanoparticles. Sci Rep 7: 9894. https://doi.org/10.1038/s41598-017-09897-5

42. Piñeiro-Redondo Y, Bañobre-López M, Pardiñas-Blanco I, et al. (2011) The influence of colloidal parameters on the specific power absorption of PAA-coated magnetite nanoparticles. Nanoscale Res Lett 6: 383. https://doi.org/10.1186/1556-276X-6-383

43. Wu WF, Wang JN, Li Z, et al. (2020) 7-Hydroxycoumarin protects against cisplatin-induced acute kidney injury by inhibiting necroptosis and promoting Sox9-mediated tubular epithelial cell proliferation. Phytomedicine 69: 153202. https://doi.org/10.1016/j.phymed.2020.153202

44. Le Chang XLL, Dai Di Fan YQM, Huan Zhang HPM, et al. (2016) The efficiency of magnetic hyperthermia and in vivo histocompatibility for human-like collagen protein-coated magnetic nanoparticles. Int J Nanomed 11: 1175–1185. https://doi.org/10.2147/IJN.S101741

45. Vihola H, Laukkanen A, Valtola L, et al. (2005) Cytotoxicity of thermosensitive polymers poly(N isopropylacrylamide), poly(N-vinylcaprolactam) and amphiphilically modified poly(Nvinylcaprolactam). Biomaterials 26: 3055–3064. https://doi.org/10.1016/j.biomaterials.2004.09.008

46. Gamal A, El-sayed ES, El-Hamoly T, et al. (2021) Magnetic thermoresponsive nanocomposite for targeted PARP-1 in colorectal adenocarcinoma, an approach for tumor dual therapy research square. https://doi.org/10.21203/rs.3.rs-295938/v1

Resistive and propulsive forces in wheelchair racing: a brief review

Ricardo Silveira,*, Daniel A. Marinho, Catarina C. Santos, Tiago M. Barbosa, Eduarda Coelho, Jorge Morais and Pedro Forte

1 Department of Sports, Higher Institute of Educational Sciences of the Douro, 4560-708 Penafiel, Portugal

2 Department of Sport and Physical Education, Polytechnic Institute of Bragança, 5300-253 Bragança, Portugal

3 Research Center for Sports Health and Human Development, 6201-001 Covilhã, Portugal

4 Department of Sports Sciences University of Beira Interior 6201-001 Covilhã, Portugal

5 Department of Sports Sciences, Health and Exercise, University of Trás-os-Montes

ABSTRACT

Wheelchair racing is one of the most important sports in the Paralympics. The detailed analysis of all parameters is of great importance to achieve sporting excellence in this modality. In wheelchair racing, resistive and propulsive forces determine the movement of the athlete-wheelchair system. Most of propulsive forces are generated by the strength of individuals. As a result, strength levels play an important role in propelling the athlete-wheelchair system. Thus, the main objective of this study is to provide a set of methodologies to assess propulsive and resistive forces. The manuscript presents different methods and procedures, based on previous studies, that can be used for wheelchair racing athletes. Resistive forces in wheelchair racing can be evaluated by analytical procedures, experimental tests, and numerical simulations. Moreover, the strength of athletes' upper limbs to generate propulsion in wheelchair races can be assessed by dynamometry, one-repetition maximum, and medicine ball throw test. It may be that the tests presented may be useful to predict the strength and endurance of athletes' upper limbs. However, this competitive sport still presents a considerable gap in the Paralympics research. Currently, in Paralympic sport, evidence-based methodologies are lacking, making it an issue for athletes, coaches and researchers to support their work on scientific evidences.

Keywords: Paralympics; drag; rolling resistance; strength; performance

1. Introduction

Paralympics play an important role in society's culture and sport practice [1]. Wheelchair racing is one of the biggest events in Paralympics [2]. Here, it is possible to identify four distinct classes (T51, T52, T53, and T54), in which the athletes' classification depends on the disability criteria (i.e. spinal cord injury) and is set according to their muscular strength [3,4]. For an athlete to be eligible in one of these classes, he or she may be affected by one or more of these characteristics: limb deficiency (amputee), loss of range of motion, muscle weakness or paralysis (resulting from spinal injury or bifid spine) and

different limbs' sizes [3]. The International Paralympic Committee defines the classification of these athletes as follows [3]: (1) T51–athletes who have a decrease on shoulders muscles strength and difficulty in elbows extension for the pushing action during the propulsive phase. The athletes do not have muscle activity and strength in the trunk muscles. Typically, athletes' propulsion is achieved by the elbow flexors and wrist extensors; (2) T52–the athletes use shoulders, elbow, and wrist muscles to propel the wheelchair. One can observe a possible weakness in the muscular strength of the fingers. The trunk muscles strength are typically absent; (3) T53–athletes may present full ability in the upper limbs; however, they may not have muscular activity in the abdominal or lower spine; and (4) T54– the participants preserve the upper limbs muscular strength and can have muscular activity in the entire trunk. T54 athletes may also have some leg capacity [3].

Wheelchair racing involves short (sprint events; 100 m, 200 m, and 400 m), middle (800 m and 1500 m), and long-distance races (5000 m and 10000 m). During the race, athletes must reach maximum speed as soon as possible and maintain it [5]. For that, higher power must be applied during the propulsive phase; and the stroke cycle is divided into the propulsive and the recovery phase [5]. The propulsive phase can be divided into: (1) the catch (the moment when the hand first touches the handrims, close to 12: 00); (2) the drive phase (pushing the handrims, between 12: 00 and 6: 00), and; (3) the release phase (the moment the hand breaks contact with the handrims, close to 6: 00) [2]. The recovery phase is the moment between the release phase and the catch, the beginning of a new stroke cycle. This moment is characterized by a backwards hyperextension of the athletes' upper limbs [2]. During the stroke cycle, the propulsive force results from the athlete's upper limbs strength applied on the handrims. Resistive forces are the drag force and the rolling resistance [5]. The athlete's ability to decrease resistance and increase propulsion can improve performance [5]. The movement phase is the moment of hand and wrist acceleration on the handrim, usually between 2: 00 and 5: 00. The release phase is when the contact between the hand and the rim breaks, close to 6: 00 [2]. The catch is the moment the hand touches the rim, it usually occurs around 1: 00 and 2: 00. [2]

To date, it is possible to find just a few studies assessing resistive forces in wheelchair racing [6,7]. And to the best of our knowledge, only one study was found assessing the athletes' upper limbs strength [8]. Furthermore, most studies that have assessed propulsion in wheelchair racing have focused on the upper limbs' kinematics [8,9]. As far as the authors know, there are no studies with protocols assessing both propulsive (based on upper limbs strength) and resistive forces. So, understanding and reporting the methods/tests available to assess such forces can allow and help to control and monitor the training sessions. This will help to identify the impact of impairments on athletes' performance and ensure that classification can be determined by injury type, training and fitness level, and assess the athletes' differences between categories. Therefore, this study seeks to present different methods and tests (laboratory and field) to evaluate the propulsive and resistive forces of wheelchair racing athletes.

2. Resistive forces / propulsive forces

2.1. Resistive forces

In wheelchair racing, the main resistive forces are drag and rolling resistance [7,10]. For speeds above 4,5 m/s, the drag contribution is above 40% [7,10]. During a Paralympic event (100 m), a T52 elite athlete may reach 5 m/s in the first 15 m [7]. Therefore, the rolling resistance is the main resistive force. During a 100 m race, the drag contribution is more than 40% during the last 75 m [5,7,10]. Wheelchair sprinters can use different strategies to minimize both rolling resistance and drag [10]. The drag is dependent on the subjects' anthropometric characteristics, speed and the athlete-wheelchair system

[11], temperature [12], and position of the athletes side-by-side on the track [13]. For instance, athletes' posture and body position (i.e., surface area) in the wheelchair influence drag by about 30% [11]. However, other conditions such as temperature and position of the athletes side-by-side on the track have not been tested yet. Moreover, a reduction of the mass in the athlete-wheelchair system may improve performance [14], and it is expected that increasing tire pressure may also improve the athletes' performance [15]. Tire pressure and type influence wheelchair impulse and propulsion [15]. Therefore, the wheelchair properties should also be optimized in order to improve the athletes' performance [15].

Much of this knowledge gap derives from a lack of understanding of the relative contributions of the biomechanical effort of the wheelchair user and the cost of mechanical wheelchair propulsion to the resulting movement [16]. A primary metric of wheelchair mobility is called "effort", which reflects the biomechanical effort of the wheelchair user while pushing the wheelchair. Studies on human propulsion effort, usually measure this variable as metabolic cost. These researches have investigated the impact of different wheelchairs types and configurations. However, these studies fail to provide information for clinical decision-making to modify the wheelchairs beyond their standard configuration [16], or use methods based on human subjects' dimensions, lacking sensitivity [17,18] to adopt different wheelchair configurations [17,18]. Given the enormous diversity of human users and their biomechanics of propulsion in different wheelchairs, the most efficient way is to first focus on developing standardized measures representative of the cost of mechanical wheelchair propulsion [17,18].

2.1.1. Drag

2.1.1.1. Wind tunnel

Wind tunnel analyses are the gold standard method for aerodynamics assessment [2,19]. However, it is considered expensive and time-consuming [2,19]. The versatility and reality of a wind tunnel reinforce its importance for aerodynamic research, considered a gold standard technique [2,20,21]. The flow in a wind tunnel test section must meet high requirements to obtain accurate and reliable measurement data. A good flow quality requires a certain degree of spatial uniformity and temporal stability of speed and pressure [22]. Thus, changes in the environmental conditions in the wind tunnel room can affect the data [22]. However, in wind tunnel tests it is not possible to obtain detailed information about the fluid flow behavior [22]. Testing different conditions in a wind tunnel requires reality-based approaches [23], therefore it is not possible to make predictions and simulations, which can increase costs in this methodology [2,19].

There are two types of wind tunnels, the open circuit and closed circuit. In the open circuit type, there is an inlet and an outlet field. This is the most simplistic and affordable type to build. In these tunnels, air is expelled directly into the laboratory and is normally re-entered after circulating through the laboratory [24,25]. However, some tunnels use a source of compressed gas [24]. The open circuit wind tunnels are relatively immune to temperature fluctuations and major disturbances in the return flow. That is caused by laboratory volume that is much higher than the tunnel [24]. There are two types of open circuit wind tunnels, the suck down and blower. Blower tunnels are the most flexible because the fan is at the entrance to the tunnel, so the test section can easily be changed or modified, seriously interrupting the flow. These tunnels tolerate that the outlet diffusers can be completely omitted to allow easier access to samples and test instruments, although the omission often results in a noticeable loss of energy [24,25]. The suck down type is also called suction tunnel, usually more susceptible to low frequency instability

in the return flow. However, some claims have been made to minimize the inlet vorticity due to the fluid not passing through the fan before entering the test [24,26].

In closed circuit wind tunnels, the flow outlet returns to the inlet portion of the tunnel (entrance); whereas, in closed circuits the amount of the air and its flow are constant, improving the efficiency of the tests. Typically, closed circuit wind tunnels are larger and designed to maintain as much fluid flow uniformity as possible [25–27]. Ventilators in the test section power the tunnels. Moreover, some include multi-stage compressors (required for transonic and supersonic air speeds) [25–27]. These closed circuit wind tunnels are characterized by air recirculation, lower air energy requirement, lower speeds and better control of test conditions. [24–27].

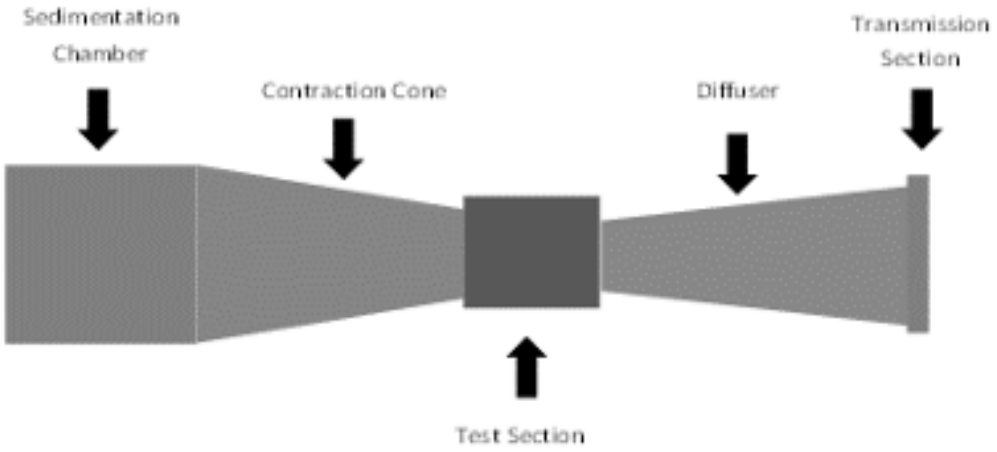

Figure 1. Five main components to the wind tunnel testing.

It is possible to identify five main components in wind tunnels (Figure 1). The components are the sedimentation chamber, the contraction cone, the test section, the diffuser, and the transmission section [24,25]. In the sedimentation chamber, it is possible to find a honeycomb material to conduct and preserve the airflow uniformity. The rotating fan creates a movement in the air that has an undesirable effect on the test section. The honeycomb eliminates this uneven air flow [24,26]. The contraction cone component is designed to increase the air speed in the test section without additional turbulence in the air flow [24]. The objects to be tested and analyzed are placed in the test section [24,26]; where, in this chamber the evaluations and observations are made [24,27]. The diffuser chambers are similar to cones, expanding as they move away from the test section. This allows an increase in the fluid pressure and a decrease in its velocity. The air flow is slowed down and minimizes the turbulence in the diffuser; here, the test section is connected to the fan [24,27]. Finally, the transmission section allows choosing the wind speed in the test section. [21]. So far, no study assessing the aerodynamics of wheelchair racing athletes by wind tunnel was found. That said, there is a need to fill this research gap. Further research should compare drag through the gold standard method (wind tunnel) with numerical simulations, experimental testing, and analytical procedures. Comparing them can help to better understand the fluid flow behaviour and the drag variations between methods.

2.1.1.2. Analytical procedures

Drag can be estimated by analytical procedures (equation 1). These provide information in real time and on site and are more accessible compared to other available techniques such as the numerical simulations and experimental procedures [20]. However, analytical procedures require the use of assumptions and/or estimated values for specific variables. To date, no study compared analytical procedures with different drag assessment techniques in wheelchair racing. In cycling, it is possible to find studies comparing analytical procedures with numerical simulations and the results show high values of agreement between the methods [20,28]. That said, it is necessary to minimize the research gap by assessing the effect of different temperatures, altitudes, equipment, and performance predictions based on analytical procedures.

$$F_d = \frac{1}{2} \cdot \rho \cdot v^2 \cdot A \cdot C_D \quad (1)$$

In which, Fd is the drag force (in N), p is the air density (in kg/m3), v is the velocity (in m/s), A is the surface area (m2), and CD represents the drag coefficient (dimensionless). The effective area (ACD) is computed by the product of CD and A.

2.1.1.3. Coasting deceleration techniques

Deceleration techniques do not allow to control environmental factors such as wind, humidity, temperature, and variations in the subjects' positions [2,11]. However, aerodynamic and rolling resistance can be tested to provide realistic possibilities that cannot be achieved in laboratorial settings. Deceleration techniques found in the literature are: (1) rolling distance applying the ramp methods; (2) the timing gate method that measures the decrease in speed at different points between two brands (doors); and (3) the speed method that directly measures velocity at each time [2].

The method of rolling distance with the ramp consists in rolling a wheelchair from a ramp to the track. The wheelchair will be accelerated on the ramp, then the total distance covered will be measured [29]. The timing method is an alternative to rolling distance; in which the unit of measure will be the time that the wheelchair spends between two marks. In these procedures, the wheelchair may be accelerated before the marks [29]. Finally, in the speed method, the athlete can accelerate the wheelchair to maximum speed, then speeds are recorded in each instance [14,29].

The friction force on a rolling object is not usually a topic discussed in introductory physics textbooks. Although the invention of the wheel is one of the essential world achievements, rolling friction is usually ignored [30].

2.1.1.4. Numerical simulation

Computational fluid dynamics (CFD) is part of biomechanics and aims to analyze the fluid flow behavior. This methodology allows the discretization of Navier-Stokes equations by the finite volume method [31,32]. These equations come from Newton's second law in fluid mechanics, assuming that the fluid stress is the sum of the diff [31,33]. The solution to the equations determines the fluid speed at a given point in space and time. In CFD, space is divided into small cells to form a grid or mesh volume. Then an algorithm is applied to solve the equations of volume motion [31]. For data collection, a three-dimensional model of a wheelchair racing athlete is required. The three-dimensional model can be acquired by three dimensional scanners [11,33]. Software such as Sense 3D (3D Systems, Inc., Rock Hill, SC, USA) and Geomagic Studio (3D Systems, Rock Hill, SC, USA) allow the image processing. The files can be saved in IGES format (* .igs) in order to be executable in the Ansys Mesh module

(Ansys Fluent 16.0, Ansys Inc., Pennsylvania, USA); here, it is possible to generate the grid or mesh elements. The Mesh module (Ansys Mesh, Ansys Inc., Pennsylvania, USA) will allow building the graphic model representative of the volume subdivided into small cells or elements and define the boundary conditions [11,33]. At solid borders and close to them, FLUENT (Fluent®) calculates the Reynolds and energy stresses [11,32].

The Fluent® commercial code can be used in order to predict the behavior of physical phenomenon by numerical calculations. So far, this was the only software used to assess the aerodynamics of wheelchair racing athletes through numerical simulations [5,11]. The numerical code allows the output of pressure, viscosity, total drag, and respective coefficients [20,21]. The average Reynolds values that come from the Navier-Strokes equations (RANS) have been used in sports aerodynamics analysis [11,20,21]. These equations are solved by decomposing the instantaneous values into means. The fluid flow behavior is given by equation 2, Reynolds tension by equation 3, temperature by equation 4, and mass transfer by equation 5.

$$\frac{\partial_{Ui}}{\partial_{xi}} = 0 \tag{2}$$

$$\frac{\partial_{Ui}}{\partial_t} \pm U_j \frac{\partial_{Ui}}{\partial_{x_j}} = -\frac{1}{\rho}\frac{\partial P}{\partial x_j} + \frac{\partial}{\partial x_j}\left(2\nu S_{ij} - \overline{\mu_j{}'\mu_i{}'}\right) \tag{3}$$

$$\frac{\partial_{\theta i}}{\partial_t} \pm U_j \frac{\partial_{\theta}}{\partial_{x_j}} = \frac{1}{\rho_{cp}}\frac{\partial}{\partial x_j}\left(k\frac{\partial \theta}{\partial x_j} - \overline{\mu_j{}'\theta'}\right) \tag{4}$$

$$\frac{\partial_C}{\partial_t} \pm U_j \frac{\partial_C}{\partial_{x_j}} = \frac{\partial}{\partial x_j}\left(D\frac{\partial C}{\partial x_j} - \overline{\mu_j{}'c'}\right) \tag{5}$$

In the equations, the instantaneous velocity and the position are given by μi and xi respectively, the instantaneous pressure is given by p, t is the time, ρ the fluid density, the molecular kinematic viscosity is given by v, the cp is the heat capacity, the thermal conductivity is k, the Sij is the strainrate tensor, c is the instantaneous concentration, and D is the molecular diffusion coefficient. The Reynolds stresses component $\overline{\mu_j{}'\mu_i{}'}$ is the turbulence of the mean flow, and the fluid flow parcels will create the exchange of momentum.

For aerodynamic analysis of wheelchair races, turbulent flows, characterized by fluctuating velocity fields as supported by the literature, can be used [5,11]. Fluctuations can be small-scale and high-frequency, and computation time may be expensive. However, it is possible to calculate the mean of the instantaneous equations, manipulating them so that in small scale they are removed. This creates a set of less expensive equations by new unknown variables to be added. These unknown variables are determined by the turbulence models. The turbulence models are necessary for the fluids computational simulations. In Fluent® there are several models available [11,32,34]: (i) -Standard K epsilon; (ii) -Standard K-ε; (iii) -Realizable K-ε; (iv) -Spalart-Allmoras; (v) -Reynolds Stress (RSM). The turbulence model used in past studies with a wheelchair racing athlete was the k-ε (Realizable kε) [11,28,35]. This model presents speed curves similar to the Standard K– ε model, which presents greater computing savings [11,28].

Fluent® processes, solves, and outputs the results. When importing the created mesh, it allows defining the boundaries, fluid properties, materials and it executes the resolution operations using the SIMPLE © or PISO algorithm. Upon that, it is possible to study the fluid flow behavior, transmission of heat and/or mass, changes of phases, chemical reactions, and movements. In Fluent®, it is possible to obtain data such as viscosity, pressure and total drag, as well as the respective drag coefficients [11]. It is possible to find CFD studies on the aerodynamics of wheelchair racing [5,7,11]. To date, the literature

presents works that used numerical simulations or analytical models to assess resistive forces with a single elite athlete [5,7,11,35]. Comparing different methods to assess drag with CFD in wheelchair racing athletes is still unclear. Moreover, there is a lack of research assessing different athlete's positions, competitive categories, and temperature effects on drag.

2.1.2. Rolling resistance

In wheelchair racing, rolling resistance results from the friction of the tires on the ground. Rolling resistance can be reduced by mass and/or equipment [2] and can be determined using equation 6.

$$F_R = \mu_r mg + k_f mgv^2 \quad (6)$$

In equation 6, FR is the rolling resistance, μr is the coefficient of resistance, m is the mass of the athlete in the wheelchair, g is the acceleration of gravity and kf is the coefficient of the influence of speed on the rolling resistance, and v^2 is the velocity.

2.1.2.1. Equipment

Sawatzky et al. [36] conducted a study on tire pressure. The authors found no significant differences in rolling resistance until the pressure decreased to 50% of the recommended value. However, the performance with a solid tire was inferior compared to the pneumatic tire, even when inflated to 25% of the recommended pressure. Tires that were inflated to only 25% corresponded to an increase of almost 25% in energy expenditure. This study showed that when inflated at 50% of the recommended pressure, the pneumatic tires have less rolling resistance than solid tires. Wheelchair athletes who use solid tires may experience greater fatigue due to the added resistance [36]. In road cycling, tire pressure influences performance and comfort. A bicycle with high tire pressure is more efficient because it has less rolling resistance. However, it is not as comfortable as it increases the vibration from the road surface to the athlete [37]. It is possible to find studies on tire pressure and its effect on cyclists and wheelchair athletes [37]. However, no study was found on the influence of tire type and pressure levels on the performance of wheelchair racing sprinters.

2.1.2.2. Mass reduction method

In wheelchair racing the wheelchair mass is an important parameter for rolling resistance. Diminishing the rolling resistance by the mass reduction allows an improvement in winning time [14]. The influence of mass on victory time is much higher comparing to the influence of the rolling friction coefficient (1.5x to 4x higher) and higher than the drag coefficient (4x to 5.5x higher) in sprinting events (15 > 30 s race) [14]. With small mass reductions, the arrival time can improve even in sprint events [14].

To assess rolling resistance in field tests, athletes may race in the same conditions (stroke frequency, similar environmental conditions, total power or maximum speed trials) with different masses. Thus, the rolling resistance can explain the differences between the two conditions (with and without additional mass). This method (trials comparison) can be used to compare different tires, wheelchairs, spokes diameters, and pressures. The athlete's bioenergetics may be controlled to fully recover between trials [14]. So, the effect of rolling resistance can be explained by the difference between copulated mass and no additional mass.

2.1.2.3. Speed decay

Rolling resistance is usually ignored and the inability to explain or model the deceleration of a rotating rigid object on a rigid horizontal surface requires a mechanism for this phenomenon [30].

It is possible to find an equation for the relationship between the effective frictional force and the normal force on an object rolling freely along a horizontal or inclined track [29,38]. Upon that, if the object is a standard laboratory cart, this ratio is equal to the rolling resistance coefficient for realistic inclined angles. The fundamental reason why rolling resistance overcomes static friction in this case is that the wheels, as rotating components, represent only a percentage of the total mass of the cart [30]. Rolling resistance results from the loss of mechanical energy when descending a ramp [30]. There are two contributions: the deformation of the wheels and/or track, and the torque that is opposing the rotation of the wheels [39,38]. The deformation results from the flattening and/or depression of the track caused by the vehicle [40]. Static or kinetic friction mainly influences the torque that opposes the rotation of the wheels. Thus, rolling resistance acts at every moment on a moving object [40]. The partial contribution of rolling resistance and drag force shows a non-linear relationship with speed. There is a greater contribution of rolling resistance at slow speeds, while the role of drag force increases with speed. Therefore, customized solutions must be designed to reduce rolling resistance in Paralympic athletes, due to the decisive role in performance [6].

2.2. Propulsion forces

The spinal cord injury makes the athletes dependent on the upper limbs' strength for mobility (wheelchair propulsion). The strength for these tasks is provided mainly by the musculature of the upper limbs [37]. During the propulsive phase, the wheelchair will be accelerated by the athlete's ability to transfer power and strength to the handrims. Therefore, performance (speed) depends on the athlete's strength and ability to generate mechanical power [5].

Propulsive forces in wheelchair racing may be assessed by quantifying the amount of force that is applied on the handrims. However, no study was found assessing propulsive force in wheelchair racing athletes. Most studies focus on athlete's upper limbs strength and kinematic analysis [8,9]. Thus, the assessment of the athlete's upper limbs strength has been used alternatively to assess propulsive force. Some studies with disable-bodied subjects on wheelchair analyzed procedures such as dynamometer [8], one-repetition maximum [41], and medicine ball throw [42].

In the study by Miyazaki et al. [43] a force sensor system was used on the wheelchair wheel. The tangential force waveforms were measured and then the waveforms were classified as bimodal or unimodal depending on the athletes' propulsion style (technique). Thus, the ability to apply propulsive force during the push phase, which is difficult to estimate by kinematic analysis, could be estimated using the force sensor system [43]. However, the authors did not compare the differences between propulsive tangential force and upper limbs strength.

Altogether, the literature is scarce on the subject of propulsion and upper limbs strength assessment. So far, there are no standardized methods to assess propulsive force and upper limbs strength [8,9]. Thus, it is important to present different tests to assess upper limbs strength. In the authors' understanding, the greater the strength of the upper limbs, the higher the probability of increased levels of propulsive tangential force.

2.2.1. Dynamometry

One of the standard technologies capable of providing data reliability for muscular strength is the isokinetic dynamometry [44]. Vanlandewijck et al. [8] measured the upper limbs strength on elbows extension with and without backrest support in wheelchair athletes. In this test, the participants were seated in a fixed chair on the floor. In front of the participants there was a dynamometer fixed on the wall, adjustable in height and width and positioned in front of the chest.

The participant imposed maximum strength for 3 seconds, perpendicular to the plates and pushing against the wall with both hands. Three tests were performed with full recovery between tests. The authors presented values of mean maximal force of 52.02 kilograms of force (Kgf) with backrest; and 30.48 Kgf without backrest for the wheelchair basketball athlete. In the same study, a wheelchair tennis athlete produced a force of 54.72 Kgf with a backrest support; and 10.62 Kgf without the backrest support. It should be noted that the inclusion of abdominal muscles resulted in a strength loss of 41.41% for the basketball athlete and 80.59% for the tennis athlete. This procedure can probably be used to assess the propulsive forces (upper limbs strength) of the wheelchair runner. However, there may be some concerns to rule out abdominal muscles activity. The Figure 2 presents a representative dynamometry test to assess elbows extension strength levels.

Figure 2. Dynamometry test to assess upper limbs strength by elbows extension.

2.2.2. One-repetition maximum

As in most sports [44,45], strength is a component of success in competition and so it is in wheelchair racing. Recommendations for exercises and training stimuli are based on coaches' experiences and, in particular, comprehensive research in sports science [46]. However, it is possible to identify a lack of research on wheelchair racing with precise guidelines for specific training protocols, especially in strength training [46].

Tørhaug et al. [47] assessed the effect of strength training on maximal bench press on work economy during wheelchair propulsion in men with spinal cord injury. The strength tests (one-repetition maximum test, 1RM) were performed using an adjustable bench press and a calibrated bar in the Eleiko Olympic version (Eleiko AB, Halmstad, Sweden) encoder (20 kg, 2,85 cm in diameter, 2,20 m in length) with weights. All participants were lying supine on a pedestal tied with a Velcro strap at the waist for stability and then stood up. Power, force, and speed were recorded using the MuscleLab 4000e

(V.8.10; Ergotest Innovation A.S., Porsgrunn, Norway). The MuscleLab system's maximum measurement error is less than 0,3, 0,9 and 1,2% for strength, speed, and power, respectively. To determine the 1RM for each participant, loads were added (three to five times) with rest periods of 5 minutes until reaching the maximum value. The 1RM was accepted when the entire survey was completed in a controlled manner, without assistance [47]. This protocol allows assessing the maximum strength of the upper limbs of wheelchair racing athletes. However, a set of procedures are required to stabilize the trunk, avoiding falls or unbalance positions/postures. Moreover, medical recommendations might be taken in account about spinal cord injury severity and integrity during the exercise [48].

2.2.3. Throwing the medicine ball

The use of medicine balls in sports has been used to assess upper limbs strength [48–50]. The combination of strength and speed usually has strength as a key element for the successful execution [50]. Given this, it is expected that strength training programs can improve the muscle power of athletes, helping them to accelerate as quickly as possible [5].

The medicine ball throw test is inexpensive and can provide the trainer with valuable information about the effectiveness of training programs [50]. This test has been used to assess propulsive strength [41]. Thus, the aforementioned test might be used to assess the upper limbs muscular power in wheelchair racing athletes (Figure 3). The athletes can be instructed to, in a seating position, keep both feet parallel and shoulder-width while throwing the medicine ball (mass of 1 kg and circumference of 0,72 m) [51]. The speed and distance that the ball hits on the field allow us to quantify muscular strength [41].

To date, no study has been found that assessed the upper limbs strength of wheelchair racing athletes by the medicine ball throw. Moreover, there is a need to compare the medicine ball throw with different methods (e.g., dynamometry and one-repetition maximum) [41].

Figure 3. Wheelchair racing athlete throwing the medicine ball.

3. Conclusions and further research

This study presented a set of methodologies to assess propulsive and resistive forces. Additionally, recommendations were provided for different evaluations. The wheelchair racing resistive forces can be assessed by analytical procedures, experimental tests, and numerical simulations. This paper presented a set of tests to assess upper limbs strength to generate propulsion forces in wheelchair racing

athletes. However, there is limited research about direct methods to assess propulsive tangential force. It is possible that the tests presented may be useful to predict the strength and resistance of the upper limbs of athletes.

To date, there is no study comparing the different methods. There is a lack of research about equipment testing and performance predictions in different environmental conditions in wheelchair racing. Furthermore, it is important to understand the effect of different environment temperatures on the athletes' performance and the effect of their track disposition during the race. That said, different competitive categories, postures, temperatures and athletes' disposition on the track influence the resistive and propulsive forces of the subjects and, consequently, their performance.

The community should be aware that by decreasing the mass of the athlete-wheelchair system, the performance will be improved if the athlete maintains full power (ability to generate force). Controversy, small adjustments in technique and changing the position in the chair, can reduce drag and, consequently, improve performance. Athletes must maintain proper body alignment and synchronization during stroke cycles, allowing them to reach and maintain maximum speed with less energy cost [5].

Coaches and analysts can use these methodologies to conduct evidence-based practice, helping athletes to improve their performance.

Acknowledgments (All sources of funding of the study must be disclosed)

This research is supported by the Portuguese Foundation for Science and Technology, I.P. (project UIDB04045/2020) and The APC. It has been funded by the Research Center in Sports Health and Human Development, Covilhã, Portugal.

Conflict of interest

The authors declare no conflict of interest.

Author contributions:

Conceptualization, R.S.; P.F.; E.C. and J.E.M..; methodology, P.F. and J.E.M.; validation, T.M.B, D.A.M; formal analysis, R.S., C.C.S P.F.; investigation, R.S. and P.F.; resources, D.A.M and T.M.B.; data curation, R.S. and P.F.; writing—original draft preparation, R.S. C.C.S. and P.F.; writing—review and editing, P.F., J.E.M., E.C., T.M.B; visualization, D.A.M, E.C. and J.E.M.; supervision, P.F., E.C. and J.E.M.; project administration, R.S. and P.F.; funding acquisition, D.A.M. and T.M.B. All authors have read and agreed to the published version of the manuscript.

References

1. Celestino T, Pereira A (2018) In a pursuit of excellence in the adapted sport: a case study. Desporto e Atividade Física para Todos–Revista Científica da FPDD 4: 25–37

2. Forte P, Barbosa TM, Marinho DA (2015) Technologic appliance and performance concerns in wheelchair racing–helping Paralympic athletes to excel, In: Liu, C.H., 101–121. http: //dx.doi.org/10.5772/61806

3. IPC International Paralympic Committee Athletics Classification Rules and Regulations, 2018. Available from: https://www.paralympic.org/athletics/classification.

4. Tweedy S, Bourke J (2009) IPC athletics classification project for physical impairments: Final report—stage 1.
5. Forte P, Marinho DA, Morais JE, et al. (2018) Estimation of mechanical power and energy cost in elite wheelchair racing by analytical procedures and numerical simulations. Comput Method Biomec Biomed Eng 21: 585–592. https://doi.org/10.1080/10255842.2018.1502277
6. Barbosa TM, Forte P, Morais JE, et al. (2014) Partial contribution of rolling friction and drag force to total resistance of an elite wheelchair athlete. In 1st International Conference in Sports Science & Technology. Institute for Sports Research 749–753.
7. Barbosa TM, Coelho E (2017) Monitoring the biomechanics of a wheelchair sprinter racing the 100 m final at the 2016 Paralympic games. Eur J Phys 38: 044001.
8. Vanlandewijck YC, Verellen J, Tweedy SM (2010) Towards evidence-based classification-the impact of impaired trunk strength on wheelchair propulsion. Adv Rehabil 3: 1–5. https://www.researchgate.net/publication/284843638
9. Cooper RA (1990) Wheelchair racing sports science: a review. J Rehabil Res Dev 27: 295–312.
10. Forte P, Marinho DA, Morais JE, et al. (2019) Analysis of the resistive forces acting on a world ranked wheelchair sprinter at different speeds. Motricidade 15: 78–79.
11. Forte P, Marinho DA, Morais JE, et al. (2018) The variations on the aerodynamics of a world ranked wheelchair sprinter in the key-moments of the stroke cycle: a numerical simulation analysis. PloS One 13: e0193658. https://doi.org/10.1371/journal.pone.0193658
12. Beaumont F, Lestriez P, Estocq P, et al. (2019) Aerodynamic investigation of the thermo dependent flow structure in the wake of a cyclist. J Biomech 82: 387–391. https://doi.org/10.1016/j.jbiomech.2018.11.006
13. Blocken B, Toparlar Y, van Druenen T, et al. (2018) Aerodynamic drag in cycling team time trials. J Wind Eng Ind Aerod 182: 128–145. https://doi.org/10.1016/j.jweia.2018.09.015
14. Fuss FK (2009) Influence of mass on the speed of wheelchair racing. Sports Eng 12: 41–53. https://doi.org/10.1007/s12283-009-0027-2
15. de Groot S, Vegter RJK, van der Woude LHV (2013) Effect of wheelchair mass, tire type and tire pressure on physical strain and wheelchair propulsion technique. Med Eng Phys 35: 1476–1482. https://doi.org/10.1016/j.medengphy.2013.03.019
16. Cowan RE, Nash MS, Collinger JL, et al. (2009) Impact of surface type, wheelchair weight, and axle position on wheelchair propulsion by novice older adults. Arch Phys Med Rehab 90: 1076 1083. https://doi.org/10.1016/j.apmr.2008.10.034
17. Sagawa JrY, Watelain E, Lepoutre FX, et al. (2010) Effects of wheelchair mass on the physiologic responses, perception of exertion, and performance during various simulated daily tasks. Arch Phys Med Rehab 91: 1248–1254. https://doi.org/10.1016/j.apmr.2010.05.011
18. Samuelsson KAM, Tropp H, Nylander E, et al. (2004) The effect of rear-wheel position on seating ergonomics and mobility efficiency in wheelchair users with spinal cord injuries: a pilot study. J Rehabil Res Dev 41: 65–74.
19. MacLeish MS, Cooper RA, Harralson J, et al. (1993) Design of a composite monocoque frame racing wheelchair. J Rehabil Res Dev 30: 233.
20. Forte P, Marinho DA, Nikolaidis PT, et al. (2020) Analysis of cyclist's drag on the aero position using numerical simulations and analytical procedures: a case study. Int J Env Res Pub He 17: 3430. https://doi.org/10.3390/ijerph17103430
21. Forte P, Morais JE, P Neiva H, et al. (2020) The drag crisis phenomenon on an elite road cyclist— a preliminary numerical simulations analysis in the aero position at different speeds. Int J Env Res Pub He 17: 5003. https://doi.org/10.3390/ijerph17145003
22. Moonen P, Blocken B, Carmeliet J (2007) Indicators for the evaluation of wind tunnel test section flow quality and application to a numerical closed-circuit wind tunnel. J Wind Eng Ind Aerod 95:

1289–1314. https://doi.org/10.1016/j.jweia.2007.02.027
23. Defraeye T, Blocken B, Koninckx E, et al. (2010) Aerodynamic study of different cyclist positions: CFD analysis and full-scale wind-tunnel tests. J Biomech 43: 1262–1268. https://doi.org/10.1016/j.jbiomech.2010.01.025
24. Singh M, Singh N (2013) Review of design and construction of an open circuit low speed wind tunnel. Glob J Res Eng
25. Moonen P, Blocken B, Roels S, et al (2006) Numerical modeling of the flow conditions in a closed-circuit low-speed wind tunnel. J Wind Eng Ind Aerod 94: 699–723. https://doi.org/10.1016/j.jweia.2006.02.001
26. Panda MK, Samanta AK (2016) Design of low cost open circuit wind tunnel-a case study. Indian J Sci Technol 9: 1–7. https://doi.org/10.17485/ijst/2016/v9i30/99195
27. Calautit JK, Chaudhry HN, Hughes BR, et al. (2014) A validated design methodology for a closed loop subsonic wind tunnel. J https://doi.org/10.1016/j.jweia.2013.12.010
28. Forte P, Marinho DA, Barbosa TM, et al. (2020) Estimation of an elite road cyclist performance in different positions based on numerical simulations and analytical procedures. Front Bioeng Biotech 8: 538. https://doi.org/10.3389/fbioe.2020.00538
29. Kolitzus HJ (2003) Ball roll behavior: The functional relationship of the ball roll distance and the timing gate method: How to calculate the ball roll distance from timing gate measurements. Int Assoc Sport Surf Sci
30. Minkin L, Sikes D (2018) Coefficient of rolling friction-Lab experiment. Am J Phys 86: 77–78. https://doi.org/10.1119/1.5011957
31. Marinho DA, Barbosa TM, Mantha V, et al. (2012) Modelling propelling force in swimming using numerical simulations. Fluid Dyn, Comput Model Appl 439–448.
32. Forte P, Marinho DA, Barbosa TM, et al. (2020) Estimation of an elite road cyclist performance in different positions based on numerical simulations and analytical procedures. Front Bioeng Biotech 8: 538. https://doi.org/10.3389/fbioe.2020.00538
33. Forte P, Marinho DA, Barbosa TM, et al. (2020) Analysis of a normal and aero helmet on an elite cyclist in the dropped position. AIMS Biophys 7: 54–64. https://doi.org/10.3934/biophy.2020005
34. White F (1999) Fluid Mechanics, 7 Eds., New York
35. Barbosa TM, Forte P, Estrela JE, et al. (2016) Analysis of the aerodynamics by experimental testing elite wheelchair https://doi.org/10.1016/j.proeng.2016.06.180
36. Sawatzky B, Kim W, Denison I (2004) The ergonomics of different tyres and tyre pressure during wheelchair propulsion. Ergonomics https://doi.org/10.1080/00140130412331290862
37. Richard S, Champoux Y, Lépine J, et al. (2015) Using an alternative forced-choice method to study shock perception at cyclists' hands: the effect of tyre pressure. Procedia Eng 112: 361–366. https://doi.org/10.1016/j.proeng.2015.07.263
38. Besson U, Borghi L, De Ambrosis A, et al. (2007) How to teach friction: Experiments and models. Am J Phys 75: 1106–1113. https://doi.org/10.1119/1.2779881
39. Krasner S (1992) Why wheels work: a second version. Phys Teach 30: 212–215. https://doi.org/10.1119/1.2343520
40. Mungan CE (2012) Rolling friction on a wheeled laboratory cart. Phys Educ 47: 288.
41. Morais JE, Silva AJ, Marinho DA, et al. (2016) Effect of a specific concurrent water and dry-land training over a season in young swimmers' performance. Int J Perf Anal Sport 16: 760–775. https://doi.org/10.1080/24748668.2016.11868926
42. Yanci J, Granados C, Otero M, et al. (2015) Sprint, agility, strength and endurance capacity in wheelchair basketball players. Biol Sport 32: 71. https://doi.org/10.5604/20831862.1127285
43. Miyazaki Y, Iida K, Nakashima M, et al. (2020) Measurement of push-rim forces during racing

wheelchair propulsion using a novel attachable force sensor system. Proceedings of the Institution of Mechanical Engineers, Part P: Journal of Sports Engineering and Technology, 1754337120904260. https://doi.org/10.1177/1754337120904260
44. Kauer JB, Antúnez MLVS, Fração VB, et al. (2007) Avaliação da razão de torque dos músculos flexores e extensores do cotovelo em paratletas. 39–46.
45. Smith DJ (2003) A framework for understanding the training process leading to elite performance. Sports Med 33: 1103–1126. https://doi.org/10.2165/00007256-200333150-00003
46. Turbanski S, Schmidtbleicher D (2010) Effects of heavy resistance training on strength and power in upper extremities in wheelchair athletes. J Strength Cond Res 24: 8–16.
47. Tørhaug T, Brurok B, Hoff J, et al. (2016) The effect from maximal bench press strength training on work economy during wheelchair propulsion in men with spinal cord injury. Spinal Cord 54: 838–842. effects
48. Ragnarsson, KT (2008) Functional electrical stimulation after spinal cord injury: current use, therapeutic and future directions. Spinal Cord 46: 255–274. https://doi.org/10.1038/sj.sc.3102091
49. Yang YS, Koontz AM, Triolo RJ, et al. (2009) Biomechanical analysis of functional electrical stimulation on trunk musculature during wheelchair propulsion. Neurorehab Neural Re 23: 717–725.
50. Stockbrugger BA, Haennel RG (2001) Validity and reliability of a medicine ball explosive power test. J Strength Cond Res 15: 431–438.
51. Van den Tillaar R, Marques MC (2011) A comparison of three training programs with the same workload on overhead throwing velocity with different weighted balls. J Strength Cond Res 25: 2316–2321. https://doi.org/10.1519/JSC.0b013e3181f159d6

Interplay and multiscale modeling of complex biological systems

Carlo Bianca1,2,*
1 Laboratoire Quartz EA 7393, École Supérieure d'Ingénieurs en Génie Électrique, Productique et Management Industriel, 13 Boulevard de l'Hautil, 95092 Cergy Pontoise Cedex, France
2 Laboratoire de Recherche en Eco-innovation Industrielle et Énergétique, École Supérieure d'Ingénieurs en Génie Électrique, Productique et Management Industriel, 13 Boulevard de l'Hautil, 95092 Cergy Pontoise Cedex, France

ABSTRACT

Recently the understanding of complex biological systems has been increased considering the important interplay among different scholars coming from different applied sciences such as mathematics, physics and information sciences. As known, the modeling of a complex system requires the analysis of the different interactions occurring among the different components of the system. Moreover, the analysis of a complex system can be performed at different scales; usually the microscopic, the mesoscopic and the macroscopic scales are the most representation scales. However, a multiscale approach is required. A unified approach that takes into account the different phenomena occurring at each observation scale is the desire of this century. This editorial article deals with the topic of this special issue, which is devoted to the new developments in the multiscale modeling of complex biological systems with special attention to the interplay between different scholars.

Keywords: mathematical models; multi-agent models; multiscale models; validation; system biology

Preface

In the last two decades, the research activity in biology has shown the important interplay between different scientists in order to gain information in the modeling and analysis of complex phenomena occurring in the real world. In particular, complex biological systems have gained much attention and the interplay among mathematicians, physicists and information science scholars on the one hand and biologists, immunologists, physicians on the other hand have increased. Moreover, the different international calls for interdisciplinary projects have extensively allowed the interactions and the collaborations among the different scholars coming from the different sciences and the different countries. Consequently, new hybrid research domains and scholars have raised and the management of complexity has been more easily pursued and achieved.

The complex emerging behaviours in biological systems are the consequence of nonlinear interactions among a large number of elements composing the biological system [1,2]. A biological system is usually composed by molecules, cells, and tissues (see the books [3]) whose global interaction is not the linear sum of each interaction. The analysis of complex biological systems thus requires a particular attention and is usually performed in three steps: A theoretical analysis (or phenomenological analysis), a computational analysis (or modeling analysis) and a numerical or experimental analysis (or validation analysis). This approach is nowadays well-developed and the main contributions in the pertinent literature refer, among others, to the tumor growth and immune system

competition [4], soft tissues growth [5], fibroproliferative disorders [6], genoma analysis [7]. In particular many of the above mentioned applications have been obtained as result of the collaboration of mathematicians and physicists with scholars coming from the biological and medical sciences. The outcome of these interplays has been the birth of new hybrid research fields, among others, biomathematics, bioinformatics, biomechanics, and biophysics.

Biomathematics. This research domain is mainly the result of the interplay between biologists and mathematicians. Specifically, the biological system under consideration is modeled by employing a system of mathematical equations, usually differential equations (ordinary or partial differentential equations) and/or algebraic equations. In this context the system of mathematical equations is called 'a model' and the solution describes the time and space evolution of a quantity related to the system [8]. Accordingly assumptions and parameters are defined and the evolution of the system is analyzed by simulating a numerical solution of the model. This research field is also known as mathematical biology.

Bioinformatics. This research domain is the result of the interplay between biologists and computer science scholars. The main aim of this research field is the capture and interpretation of biological data by employing computer software programs and the internet. Agent-based models are also proposed and employed for the analysis and management of data in modern biology and medicine. An agent-based model is based on the definition of entities (agents), a set of relationships and a framework for simulating agent behaviors and interactions. The reader is addressed to [9] for a deeper understanding of this research field. It is worth stressing that bioinformatics has largely evolved in the last decade and many subfields have been emerged.

Biomechanics. This research domain is mainly the outcome of the interplay between biologists and mechanical/biomedical engineers. This research field has recently captured the interest of many mathematicians and physicists. In this research field, the methods of mechanics are employed and in particular the movement and structure of biological systems are modeled and simulated [10]. The main methods employed in biomechanics are continuum mechanics [11], mechanism analysis, structural analysis, kinematics and dynamics. Recently applications of biomechanics refer to sport [12], implant, biomaterials, biofluids. It is worth pointing out that, in the last decade biomechanics has largely increasing its application domain.

Biophysics. This research domain is mainly the consequence of the interplay between biologists and physicists/chemists. The methods of physics are employed in biophysics and all scales of biological organization, from molecular to organismic and populations, are covered [13]. In particular the interactions between the various systems of a cell, including the interactions between DNA, RNA and protein biosynthesis, are of great interest in biophysics. Moreover, molecular biology takes great advantage from the collaboration with physicists which support the physical knowledge behind the biomolecular phenomena. Among the research fields mentioned above, biophysics is considered as the research field that strongly overlaps with the other sciences.

According to the above classification, the interplay among the different scientists working in biomathematics, bioinformatics, biomechanics and biophysics has a key role in order to obtain a complete description of a biological system, namely in the development of a unified method which results in a multiscale approach. Indeed, for instance, the modeling from the molecular to the cellular scale needs the definition of the clustering of genes that produce certain phenomena at the cellular scale.

The development of a multiscale approach requires a linking among the different approaches and methods employed at each scale of observation. In particular the same phenomenon can be modeled by recurring to different approaches at different scales. In many branches of biology, such as molecular and cell biology, microbiology and histology, three mains representations scales are common to complex biological systems: Microscopic scale (molecular: gene expression and signal transduction), mesoscopic scale (cellular: cell movement and extracellular phenomena), and macroscopic scale (tissue: organ function and systemic circulation). However other scales of representation can be proposed considering the length scales of a biological system. It is worth stressing that the same method can be employed to two different scales. Indeed if the interest is the time evolution of a macroscopic quantity of the system, e.g. the density of a cell population, this quantity can be modeled by an ordinary differential equation if the cell population is homogeneous in space or by a partial differential equation if space dynamics needs to be taken into account. Accordingly the proposition of a new observation and/or representation scale or the adaptation of a specific method for the modeling of a specific phenomenon of a complex biological system is the main interest of this special issue.

In the current pertinent literature, the modeling methods developed at each scale can be summarized as follows:

microscopic scale:by means of ordinary differential equations, delay differential equations, boolean network modeling, graph theory logical, rule-based models;
mesoscopic scale:by means of partial differential equations, age-structured models, stochastic differential equations, reaction–diffusion equations, boolean network modeling, cellular automata, agent-based models, Potts models, lattice gas, lattice Boltzmann, kineti theory;
macroscopic scale: by means of ordinary differential equations, partial differential equations, lattice-based models, continuum mechanics, mechano-biological framework, agent-based models, lattice Boltzman.

A multiscale approach consists in linking the modeling frameworks proposed to lower and upper scales. The link can be obtained by introducing into a framework at a specific scale (usually the upper scale) a quantity related to the lower scale or by obtaining the dynamics at a upper scale as limit of the dynamics at lower scale (asymptotic methods). Multiscale approaches have been proposed for the tumor growth [14], would healing diseases [15], immune system [16], neural system [17], tissue engineering [18].

It is worth stressing that each modeling method presents advantages and disadvantages. Indeed the derivation of a specific theoretical model usually need assumptions which can reduce the complexity of the phenomenon and then approximate its analysis and simulation. Moreover some methods require a high computational analysis and then can be very expensive from the modeling point of view [19,20]. Bearing all above in mind, a multiscale analysis and modeling need a particular attention. Recently the definition of hybrid models, combining the above mentioned different approaches, has gained much attention. An hybrid model helps to resolve the weakness of each approach. This is an important perspective which represents another interest of this special issue.

The multidisciplinary collaboration among scholars of the biological sciences and of the applied sciences should provide the good answers to the multiscale modeling of a complex biological system and the papers published in this special issue can be considered as a primordial contribution to this research field.

References

1. Bar-Yam Y (2003) Dynamics of Complex Systems, Studies in Nonlinearity, Westview Press.
2. Nicolis G, Nicolis C (2007) Foundations of complex systems: Nonlinear dynamics, Statistical Physics, Information and Prediction, World Scientific Publishing Co. Pte. Ltd.
3. Bianca C, Bellomo N (2011) Towards a Mathematical Theory of Complex Biological Systems, World Scientific Publishing Co. Pte. Ltd.
4. Pappalardo F, Palladini A, Pennisi M, et al. (2012) Mathematical and computational models in tumor immunology. Math Model Nat Pheno 7: 186–203.
5. Kroon W, Delhaas T, Arts T, et al. (2009) Computational modeling of volumetric soft tissue growth: application to the cardiac left ventricle. Biomech Model Mechan 8: 301–309.
6. Amar MB, Bianca C (2016) Towards a unified approach in the modeling of fibrosis: A review with research perspectives. Phys Life Rev 17: 61–85.
7. Kalisky T, Blainey P, Quake SR (2011) Genomic analysis at the single-cell level. Annu Rev Genet 45: 431–445.
8. Britton NF (2003) Essential Mathematical Biology, Springer Undergraduate Mathematics Series, Springer-Verlag London.
9. Hogeweg P (2011) The roots of bioinformatics in theoretical biology. PLoS Comput Biol 7: e1002021.
10. Hatze H (1974) The meaning of the term 'biomechanics'. J Biomech 7: 189–190.
11. Chauvière A, Preziosi L, Verdier C (2010) Cell Mechanics: from Single Scale-Based Models to Multiscale Modeling, London: Chapman and Hall/CRC.
12. Bartlett R (2014) Introduction to Sports Biomechanics, Routledge, New York.
13. Glaser R (2012) Biophysics: an introduction, Springer Science & Business Media.
14. Alarcon T, Byrne HM, Maini PK (2004) Towards whole-organ modelling of tumour growth. Prog Biophys Mol Biol 85: 451–472.
15. Bunyavanich S, Schadt EE (2015) Systems biology of asthma and allergic diseases: a multiscale approach. J Aller Clin Immunol 135: 31–42.
16. Cappuccio A, Tieri P, Castiglione F (2016) Multiscale modelling in immunology: a review. Brief Bioinform 17: 408–418.
17. Breakspear M, Stam CJ (2005) Dynamics of a neural system with a multiscale architecture. Philos T R Soc B 360: 1051–1074.
18. Comisar WA, Hsiong SX, Kong HJ, et al. (2006) Multi-scale modeling to predict ligand presentation within RGD nanopatterned hydrogels. Biomaterials 27: 2322–2329.
19. Gosak M, Markovič R, Dolenšek J, et al. (2018) Network science of biological systems at different scales: A review. Phys Life Rev 24: 118–135.
20. Van Liedekerke P, Palm MM, Jagiella N, et al. (2015) Simulating tissue mechanics with agentbased models: concepts, perspectives and some novel results. Comput Part Mech 2: 401–444.

Density of electric field energy around two surface-charged spheres surrounded by electrolyte II. The smaller sphere is inside the larger one

István P. Sugár*

Department of Neurology, Icahn School of Medicine at Mount Sinai, New York, NY 10029

ABSTRACT

Based on the generalized version of Newton's Shell Theorem [7] the electric field energy density, u_F around two surface-charged spheres surrounded by electrolyte where the smaller sphere is inside the larger one is analytically calculated. According to the calculations when the surfaces of the spheres are farther from each other than four times of the Debye length the field energy density around and inside the smaller sphere is basically independent from the presence of the larger sphere. The electric field energy density is maximal when the smaller sphere touches the inner surface of the larger sphere and the maximum of u_F is located at the touching point on the outer surface of the larger sphere.

Keywords: generalized shell theorem; electric field energy density; Debye length

1. Introduction

The head groups of membrane lipids have either single charge (e.g. tetraether lipids [1], phosphatidic acid (PA), phosphatidylserine (PS), phosphatidylethanolamine (PE), and phosphatidylinositol (PI)) or electric dipole (e.g. phospholipids, such as dimyristoyl-, dipalmitoyl- and distearoylphosphatidyl choline (DMPC, DPPC and DSPC, respectively)).

Between lipids containing head groups with electric dipole there is short range interaction, i.e. where the two-body potential decays algebraically at large distances with a power equal or larger than the spatial dimension [2]. Theoretical models of lipid membranes usually focus on systems where there is short range lateral interactions between nearest neighbor lipids [3,4] because it is enough to consider only the interactions between nearest-neighbor lipid molecules. It is much more difficult to model a lipid membrane containing single charged head groups [5]. Between lipids with single charged head groups there is long range interaction, i.e. where the two-body potential decays algebraically at large distances with a power smaller than the spatial dimension [2] and thus modeling this system one has to consider the entire system rather than the interactions between the nearest-neighbor lipids. In order to get closer to the solution of this problem recently we developed a generalized version of Newton's Shell Theorem [6,7] to calculate the electric potential, V around a surface-charged sphere (of radius R1) surrounded by electrolyte at a distance Z from the center of the sphere (see also Eqs 9,10 in ref.7):

$$V(Z) = \frac{k_e \cdot Q_1 \cdot \lambda_D}{\varepsilon_r \cdot Z \cdot R_1} \cdot e^{-\frac{Z}{\lambda_D}} \cdot sinh\left(\frac{R_1}{\lambda_D}\right) \qquad at\ Z > R_1 \tag{1}$$

$$V(Z) = \frac{k_e \cdot Q_1 \cdot \lambda_D}{\varepsilon_r \cdot Z \cdot R_1} \cdot e^{-\frac{R_1}{\lambda_D}} \cdot sinh\left(\frac{Z}{\lambda_D}\right) \qquad at\ Z < R_1 \tag{2}$$

where $k_e = (4\,\pi\,\varepsilon_0)^{-1}$ is the Coulomb's constant, λ_D is the Debye length, Q_1 is the total charge of the homogeneously charged surface of the sphere of radius R_1, ε_r is the relative static permittivity of the electrolyte. Deriving Eqs.1,2 the general solution of the Screened Poisson Equation was utilized (see Eq 4 in ref.7 or A5 in Appendix 1), an equation that is valid if the electrolyte is electrically neutral [8]. It is important to note that the Screened Poisson Equation (Eq A4) is different from the Poisson-Boltzmann equation (see Eqs A1,A3). The Poisson-Boltzmann equation can be used to calculate the potential energy of an arbitrary, electroneutral, ion solution (i.e. electrolyte). However, for the solution (see Eq A2) one has to know the charge density of the ions in the electrolyte (i.e. the Boltzmann distribution; see Eq A3), which depends on the potential, V, itself. Thus only approximative solution is available (the Debye- Hückel approximation [9]), that is valid when $|z_i eV/(k_B T)| \ll 1$ (where e: charge of an electron, z_i: charge number of the i-th type of ion, k_B: Boltzmann constant, T: absolute temperature).

Using the Screened Poisson Equation (Eq A4) one can calculate the potential energy of an electrolyte that contains also external charges. The external charges are embedded into the electrolyte (like the charges of the surface-charged sphere) but not part of the electrolyte itself. For the solution one has to know the charge density of the external charges (see Eq 4 in ref.7 or Eq A5 in Appendix 1), i.e. distribution of the charges on the surface-charged sphere and not the distribution of the ions in the electrolyte. In our case it is assumed that the charges on the surface of the sphere are homogeneously distributed and in this case Eqs 1,2 is the exact solution of the Screened Poisson Equation.

Note that recently by using Eqs 1,2 electric energies have been calculated [10], such as the electric potential energy needed to build up a surface-charged sphere, and the field and polarization energy of the electrolyte inside and around the surface-charged sphere.

In this paper the density of electric field energy is calculated around two surface-charged spheres where the smaller sphere is located inside the larger one and the entire system is embedded in neutral electrolyte. This system is close to a charged vesicle [1] or to a cell [11] where charged lipids are located both on the outer and inner leaflet of the membrane, i.e. two concentric surface-charged spheres. It also models an eukaryote [12] where neutral phospholipids such as sphingomyelin and zwitterionic phosphatidylcholine are located primarily in the outer leaflet of the plasma membrane, and most anionic phospholipids, such as phosphatidic acid (PA), phosphatidylserine (PS), phosphatidylethanolamine (PE), and phosphatidylinositol (PI) are located in the inner leaflet of the plasma membrane (represented by the large surface-charged sphere of our model). Eukaryotes also have a single nucleus enveloped by double layer of lipid membranes which may contain charged lipids too (representing the smaller surface-charged sphere of our model). Note that these two charged spheres of an eukaryote are not necessarily concentric. Finally, our model is generalized for the case when the large surface-charged sphere contains several smaller surface-charged spheres. This system may also model osteoclast cells [12] containing many nuclei.

In this work the density of the electric field energy inside and outside of two surface-charged spheres are calculated at different locations. The density of the electric field energy at a point can be calculated by the following equation [13]:

$$u_F = \frac{\varepsilon_r \varepsilon_0}{2} \underline{E} \cdot \underline{E} \tag{3}$$

where $\underline{E}$ is the vector of the electric field strength at the considered point, ε_0 is the absolute vacuum permittivity and ε_r is the relative permittivity of the electrolyte.

2. Model

Here by using the recently generalized Shell Theorem [7] we calculate the density of electric field energy, u_F produced by two surface-charged spheres (see Figure 1) surrounded outside and inside by electrolyte where the smaller sphere is located inside the larger sphere.

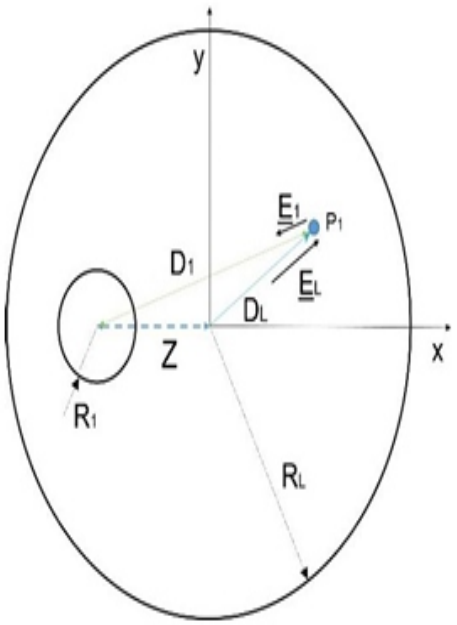

Figure 1. Two surface-charged spheres surrounded outside and inside by electrolyte where the smaller sphere is located inside the larger one.

Z: the distance between the centers of the spheres (dashed blue line); R_1 and R_L is the radius of the smaller and larger sphere, respectively; D_1 and D_L is the distance between point P_1 and the center of the smaller and larger sphere, respectively; $\underline{E}_1$ and $\underline{E}_L$ is the field strength created in point P_1 by the smaller and larger surface-charged sphere, respectively.

The origin of the coordinate system (x, y) is attached to the center of the larger sphere and the coordinates of point P_1 are x_p and y_p. The coordinates of the center of the larger and smaller sphere are $(x_L, y_L) = (0,0)$ and $(x_1, y_1) = (-Z, 0)$, respectively.

In order to calculate the density of electric field energy one has to determine the electric field strength (see Eq 3), i.e. the gradient of the electric potential. The potential produced by the smaller sphere, V_1 at a distance D_1 from its center can be calculated by Eqs 1,2 (or Eqs 9,10 in ref.[7]). The electric field strength created by the smaller sphere at point P_1 (see Figure 1) is:

$$\underline{E_1} = -grad(V_1) = -\left(\frac{dV_1}{dD_1}\frac{dD_1}{dx_P}, \frac{dV_1}{dD_1}\frac{dD_1}{dy_P}\right) = -\frac{dV_1}{dD_1}\left(\frac{d\sqrt{(x_P-x_1)^2+(y_P-y_1)^2}}{dx_P}, \frac{d\sqrt{(x_P-x_1)^2+(y_P-y_1)^2}}{dy_P}\right) =$$

$$-\frac{dV_1}{dD_1}\left(\frac{x_P-x_1}{D_1}, \frac{y_P-y_1}{D_1}\right) = \left(-\frac{dV_1}{dD_1}\frac{x_P+Z}{D_1}, -\frac{dV_1}{dD_1}\frac{y_P}{D_1}\right) = (E_{1x}, E_{1y}) \tag{4}$$

where

$$\frac{dV_1}{dD_1} = \begin{cases} \frac{k_e Q_1 \lambda_D}{\varepsilon_r R_1} sinh(R_1/\lambda_D)\left[-\frac{e^{-\frac{D_1}{\lambda_D}}}{D_1^2} - \frac{e^{-\frac{D_1}{\lambda_D}}}{D_1\lambda_D}\right] & if\ D_1 > R_1 \\ \frac{k_e Q_1 \lambda_D}{\varepsilon_r R_1} e^{-\frac{R_1}{\lambda_D}}\left[-\frac{sinh\left(\frac{D_1}{\lambda_D}\right)}{D_1^2} + \frac{cosh\left(\frac{D_1}{\lambda_D}\right)}{D_1\lambda_D}\right] & if\ D_1 < R_1 \end{cases} \tag{5}$$

where λ_D is the Debye length and $Z \leq R_L - R_1$.

Similarly, the electric field strength created by the large sphere at point P_1 (i.e. at a distance D_L from its center; see Figure 1) is:

$$\underline{E_L} = -grad(V_L) = -\left(\frac{dV_L}{dD_L}\frac{dD_L}{dx_P}, \frac{dV_L}{dD_L}\frac{dD_L}{dy_P}\right)$$

$$= -\frac{dV_L}{dD_L}\left(\frac{d\sqrt{(x_P - x_L)^2 + (y_P - y_L)^2}}{dx_P}, \frac{d\sqrt{(x_P - x_L)^2 + (y_P - y_L)^2}}{dy_P}\right)$$

$$= -\frac{dV_L}{dD_L}\left(\frac{x_P-x_L}{D_L}, \frac{y_P-y_L}{D_L}\right) = \left(-\frac{dV_L}{dD_L}\frac{x_P}{D_L}, -\frac{dV_L}{dD_L}\frac{y_P}{D_L}\right) = \left(E_{Lx}, E_{Ly}\right) \tag{6}$$

where one can construct $\frac{dV_L}{dD_L}$ from Eq 5 by changing D_1 to D_L, R_1 to R_L and Q_1 to Q_L.

$$u_F(x_P, y_P) = \frac{\varepsilon_r \varepsilon_0}{2}\underline{E}\cdot\underline{E} = \frac{\varepsilon_r \varepsilon_0}{2}\left(\underline{E_1} + \underline{E_L}\right)\cdot\left(\underline{E_1} + \underline{E_L}\right)$$

$$= \frac{\varepsilon_r \varepsilon_0}{2}([E_{1x} + E_{Lx}], [E_{1y} + E_{Ly}])\cdot([E_{1x} + E_{Lx}], [E_{1y} + E_{Ly}])$$

$$= \frac{\varepsilon_r \varepsilon_0}{2}\left([E_{1x} + E_{Lx}]^2 + [E_{1y} + E_{Ly}]^2\right) \tag{7}$$

3. Results

Here by using Eq 7 the density of the electric field energy, u_F, is calculated around two surface-charged spheres (where the smaller sphere is located inside the larger sphere) surrounded in- and outside by electrolyte. The radius of the larger and smaller sphere is: $R_L = 10^{-6}\, m$ and $R_1 = 0.2\, R_L$, respectively. The surface charge density of the homogeneously charged spheres is $\rho_s = -0.266\, C/m^2$ (the surface charge density of the PLFE lipid vesicles [1]). The total charge of the larger and the smaller sphere is, $Q_2 = \rho_s 4\pi R_2^2 = -3.3427 \cdot 10^{-12}\, C$ and $Q_1 = \rho_s 4\pi R_1^2 = -1.337 \cdot 10^{-13}\, C$, respectively. This system is axially symmetric, where the symmetry axis is the straight line connecting the centers of the spheres. The center of the attached coordinate system is at the center of large sphere and the x axis is defined by the symmetry axis. Because of the axial symmetry of the system it is enough to calculate u_F along straight lines parallel to the symmetry axis (see Figure 2), where the same y_P coordinate belongs to each straight line. The surface-charged spheres are surrounded by electrolyte containing monovalent ions. The considered electrolyte ion concentrations (of the positive ion) are: 0.00001, 0.001 and $0.1\, mol/m^3$ and the respective Debye lengths are: $3.05 \cdot 10^{-6}$, $3.05 \cdot 10^{-7}$ and $3.05 \cdot 10^{-8}\, m$ (see Table 1 in ref.7), and the relative permittivity of the electrolyte is $\varepsilon_r = 78$.

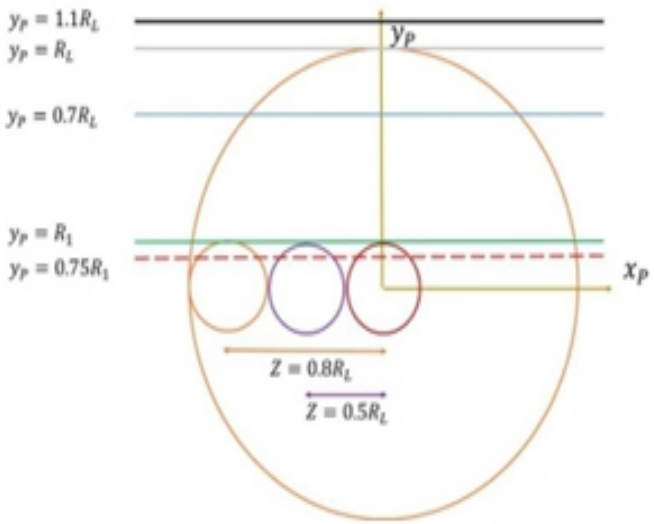

Figure 2. Locations of a small surface-charged sphere inside a large surface-charged sphere.

Inside a large surface-charged sphere of radius $R_L(= 10^{-6}\, m)$ a small surface-charged sphere of radius $R_1(= 0.2\, R_L)$ is located. The electric field energy density, u_F is calculated at the three different locations of the small sphere, i.e. in Figure 3, Figure 4 and Figure 5 the center of the small sphere is at $Z = 0.8\, R_L$ (see small orange circle), $Z = 0.5\, R_L$ (see small purple circle) and $Z = 0$ (see small dark red circle at the center of the large circle), respectively. In Figures 3–5 the electric field energy densities are calculated along the five horizontal (dashed red, green, blue, grey, black) lines.

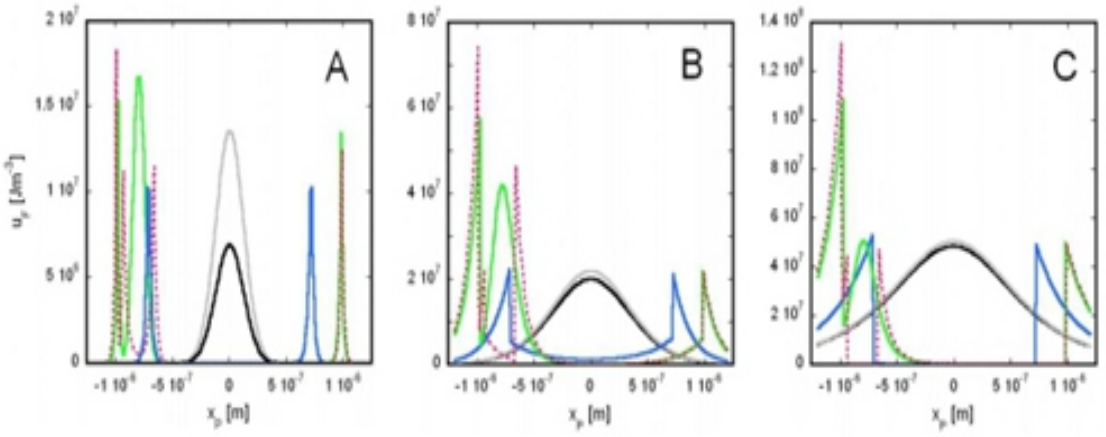

Figure 3. Density of the electric field energy around two surface-charged spheres.

$Z = 0.8\,R_L$

Dotted red line: $y_P = 0.75\,R_1$; green line: $y_P = R_1$; blue line: $y_P = 0.7\,R_L$; grey line: $y_P = R_L$; black line: $y_P = 1.01\,R_L$. The concentration of the monovalent positive (or negative) ion in the electrolyte is: A) $C = 0.1\ mol/m^3$; B) $C = 0.001\ mol/m^3$; C) $C = 0.00001\ mol/m^3$.

The connection point between the large sphere and the small sphere (represented by orange circle in Figure 2) is at $x_P = -R_L$ and $y_P = 0$. At this point there is no electrolyte and Eqs 4–7 are not applicable. Similar situations take place when the horizontal line crosses the circles in Figure 2. The x_p coordinates of these cross sections, x_p^c can be calculated by:

$$x_p^c = \pm\sqrt{R_L^2 - y_p^2} \quad \text{(crossing the large circle, i.e. } y_P < R_L\text{)} \tag{8}$$

and

$$x_p^c = -Z \pm \sqrt{R_1^2 - y_p^2} \quad \text{(crossing the small circle located at } -R_L < x_1 < 0 \text{ and } y_P < R_1\text{)} \tag{9}$$

$$x_p^c = Z \pm \sqrt{R_1^2 - y_p^2} \quad \text{(crossing the small circle located at } 0 < x_1 < R_L \text{ and } y_P < R_1\text{)} \tag{10}$$

where x_1 is the x coordinate of the center of the small sphere.

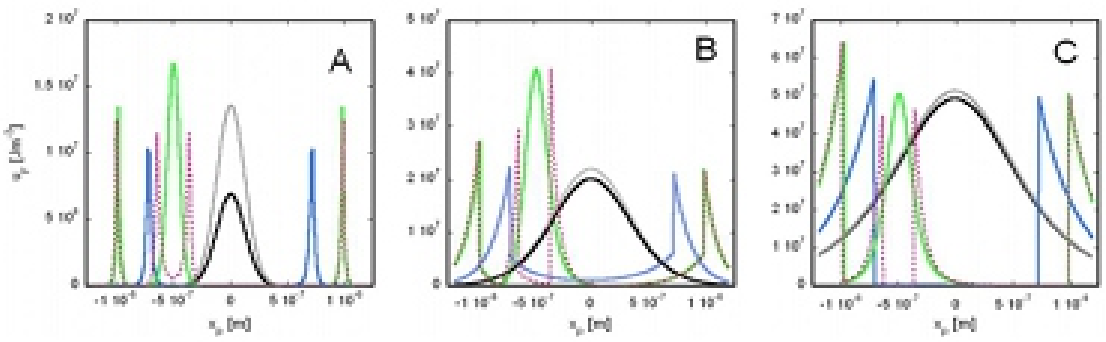

Figure 4. Density of the electric field energy around two surface-charged spheres.

$Z = 0.5\ R_L$

Dotted red line: $y_P = 0.75\ R_1$; green line: $y_P = R_1$; blue line: $y_P = 0.7\ R_L$; grey line: $y_P = R_L$; black line: $y_P = 1.01\ R_L$. The concentration of the monovalent positive (or negative) ion in the electrolyte is: A) $C = 0.1\ mol/m^3$; B) $C = 0.001\ mol/m^3$; C) $C = 0.00001\ mol/m^3$.

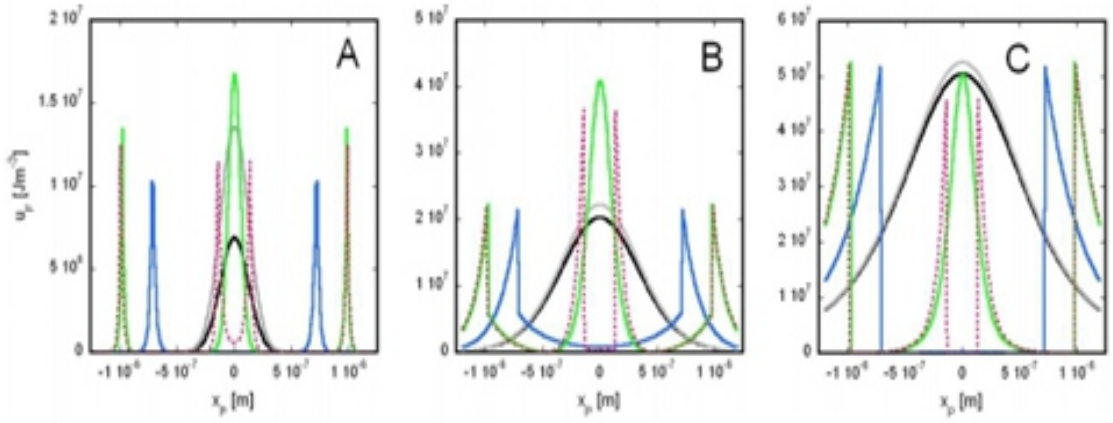

Figure 5. Density of the electric field energy around two surface-charged spheres.

$Z = 0$

Dotted red line: $y_P = 0.75\ R_1$; green line: $y_P = R_1$; blue line: $y_P = 0.7\ R_L$; grey line: $y_P = R_L$; black line: $y_P = 1.01\ R_L$. The concentration of the monovalent positive (or negative) ion in the electrolyte is: A) $C = 0.1\ mol/m^3$; B) $C = 0.001\ mol/m^3$; C) $C = 0.00001\ mol/m^3$.

Note in Figures 3–5 the sharp maxima of the density of the electric field energy appear where the horizontal line at the respective y_P crosses the charged sphere(s). These crossing points, x_p^c's, can be calculated by Eqs 8–10. In the case of $y_P = 0.75\ R_1$ the values of the crossing points are listed at the first column of Table 1.

It is also important to note that $|\underline{E}_1| \sim Q_1$ and $|\underline{E}_L| \sim Q_L$ (see Eqs 4–6) and thus in the case of total surface charges $a \cdot Q_1$ and $a \cdot Q_L$ (where $0 < a < 1$ is a constant) the electric field energy density will be a^2 times of the above calculated $u_F(x_P, y_P)$ values (see Eq 7).

4. Discussion

In this work the solution of the screened Poisson equation ([7] and Eq A5 in Appendix 1) is used to calculate the field energy density around two surface-charged spheres where the small sphere is located inside the large sphere. This solution is not restricted to small potentials (<< 25 mV) like in the case of the Debye-Hückel approximation of the Poisson-Boltzmann equation [9] where the superposition principle is not applicable either. This is an important advantage because the measured absolute value of the Zeta potentials of the cells are usually higher than 25 mV (e.g. –57.89 ± 22.63 mV on ARO cells, –40.41 ± 5.10 mV on C32TG cells, −46.99 ± 18.71 mV on RT4 cells, –40.13 ± 9.28 mV on TK cells, and −43.03 ± 5.52 mV on UM-UC-14 cells [14].

The considered two spheres (with homogeneously charged surfaces) electrically interact. If the lateral movement of the charges on the spheres would not be restricted the interaction of the smaller sphere (located inside the larger sphere) with the larger sphere would result in inhomogeneous distribution of the surface charges on both spheres. However, the free lateral diffusion of proteins and lipids are usually restricted in biological membranes not only by direct collisions with structures where immobile proteins are crowded, but also by electrostatic deflection, hydrophobic mismatches, and other mechanisms [15].

The density of the electric field energy depends on the electric field strength (Eq 3), i.e. the gradient of the electric potential (Eqs 4,6). In the case of a single surface-charged sphere surrounded by electrolyte with low ion concentration the potential inside the sphere is close to constant (see red curve in Figure 3A in ref. [7]) and thus the absolute value of the electric field strength is close to zero. On the other hand, outside the sphere the absolute value of the potential and also the electric field strength decrease with increasing distance from the surface of the sphere (see red curve in Figure 3A in ref. [7]). At higher electrolyte ion concentration, because of the increased screening effect, the absolute value of the potential and also the electric field strength decrease faster with increasing distance from the surface of the sphere. In this case inside the sphere toward its center the absolute value of the potential and the electric field strength also decrease (see curves in Figure 3A,B in ref. [7]).

In this work two surface-charged spheres (with the same surface charge density) are considered where the smaller sphere is located inside the larger sphere. The above mentioned electric properties of a single surface-charged sphere remain the same for the smaller sphere (located inside a larger sphere) if the surfaces of the spheres are far enough from each other (farther than $4\,\lambda_D$), i.e. the absolute value of the potential decreases close to zero between the surfaces of the two spheres. However, when part of the surfaces of the two spheres are close enough to each other one sphere contributes to the potential and electric field strength around the other sphere. The electric field energy density is particularly high at the place where the surfaces of the two spheres touch each other. This maximal electric field energy density is very close to the outer surface of the larger sphere. Thus one can detect at the outer surface of the erythrocyte when the nucleus is getting close.

The electric field energy density has maximum when the horizontal line crosses the circles in Figure 2. The x_p coordinates of these cross sections, x_p^c can be calculated by Eqs 8–10. When the x axis of the coordinate system is the horizontal line (i.e. $y_P = 0$) the electric field energy density is particularly high at the place where the surfaces of the two spheres touch each other (see orange circles in Figure 2) at close to zero electrolyte ion concentration (i.e. $C = 0.00001\ mol/m^3$):

$$u_F(x_p = -R_{L+}, y_p = 0; -x_1 = Z = 0.8R_L = R_L - R_1)$$

$$= \frac{\varepsilon_r \varepsilon_0}{2}(\cdot\,[E_{1x} + E_{Lx}]^2 + [E_{1y} + E_{Ly}]^2)$$

$$= \frac{\varepsilon_r \varepsilon_0}{2}\left(\left[\left(-\frac{dV_1}{dD_1}\right)_{D_1=R_{1+}} \frac{x_p - x_1}{R_{1+}} + \left(-\frac{dV_L}{dD_L}\right)_{D_L=R_{L+}} \frac{x_p}{R_{L+}}\right]^2 + [0+0]^2\right)$$

$$\cong \frac{\varepsilon_r \varepsilon_0}{2}\left(\left[-\frac{k_e Q_1}{\varepsilon_r R_{1+}^2} - \frac{k_e Q_L}{\varepsilon_r R_{L+}^2}\right]^2\right) = \frac{2\rho_s^2}{\varepsilon_r \varepsilon_0} = 1.4798 \cdot 10^8 Jm^{-3} \qquad (11)$$

This maximal electric field energy density is very close to the outer surface of the larger sphere ($|x_P| = R_{L+} \geq R_L$) on the x axis of the coordinate system. The x axis also crosses the small and large spheres at $x_p = -3\,R_1$ and $x_p = R_L$, respectively. Very close to these coss sections, at the outer side of the spheres, the field energy density is only a quarter of the above maximal value.

In general the first maximum of u_F (see the left maximum in Figures 3–5) is getting smaller when the center of the small sphere approaches the center of the large sphere. This is the case because the interaction between the spheres is reducing when the average distance between the surfaces of the two spheres is increasing.

In the case of horizontal lines where $y_P > 0$ $E_{1y} + E_{Ly}$ contributes also to u_F. This contribution is particularly high by E_{1y} when $x_p \cong -Z$ or by E_{Ly} when $x_p \cong 0$ relative to the contribution by E_{1x} and E_{Lx}, respectively.

When the location of the center of the small and large sphere is identical (i.e. $Z = 0$) then because of the additional symmetry $u_F(x_P, y_P) = u_F(-x_p, y_P)$ at any value of y_p (see Figure 5).

When $y_p > R_1$ the horizontal line crosses only the surface of the large sphere at two points and these are symmetric crossing points (where the y axis is the symmetry axis). The distance of the left crossing point from the y axis is similar to the distance of the right crossing point from the y axis (see Eq 8). Because of this symmetry if the small sphere only slightly affect the field strength along the horizontal line then $u_F(x_P, y_P) \cong u_F(-x_p, y_P)$ at any location of the small sphere along the x axis (see blue, black and grey lines in Figures 3–5).

In the case of $0 < y_p < R_1$ the horizontal line crosses twice the large and twice the small sphere. In the case of the dotted red lines in Figures 3–5 $y_p = 0.75\,R_1$ and each curve has four maxima. The hight of each maxima depends on the square of the field strength at the respective crossing point (see Eq 3), which is related to the x and y components of the field strengths created by the small sphere (E_{1x}, E_{1y}) and by the large sphere (E_{Lx}, E_{Ly}) (see Eq 7). In order to find out the reason of the hight of each maximum of the curves shown in Figures 3B–5B (i.e. at $C = 0.001\ mol/m^3$) in Table 1 these x and y components of the field strengths are listed.

Table 1. Values of the x and y components of the electric field strength at the cross sections between a horizontal line (at $y_p = 0.75 \cdot R_1$) and two spheres of radii R_1 and R_L.

Cross #	x_p [m]	u_F [J]	E_{1x} [V/m]	E_{Lx} [V/m]	E_{1y} [V/m]	E_{Ly} [V/m]
			$Z = 0.8\,R_L$			
1	$-9.9 \cdot 10^{-7}$	$7.4 \cdot 10^{7}$	$1.8 \cdot 10^{8}$	$2.47 \cdot 10^{8}$	$-1.42 \cdot 10^{8}$	$-3.74 \cdot 10^{7}$
2	$-9.4 \cdot 10^{-7}$	$2.2 \cdot 10^{7}$	$2.29 \cdot 10^{8}$	$-1.16 \cdot 10^{8}$	$-2.45 \cdot 10^{8}$	$1.86 \cdot 10^{7}$
3	$-6.6 \cdot 10^{-7}$	$4.65 \cdot 10^{7}$	$-2.29 \cdot 10^{8}$	$-5.45 \cdot 10^{7}$	$-2.45 \cdot 10^{8}$	$1.24 \cdot 10^{7}$
4	$9.9 \cdot 10^{-7}$	$2.15 \cdot 10^{7}$	$-9.7 \cdot 10^{4}$	$-2.47 \cdot 10^{8}$	$-8.2 \cdot 10^{3}$	$-3.74 \cdot 10^{7}$
			$Z = 0.5\,R_L$			
1	$-9.9 \cdot 10^{-7}$	$2.73 \cdot 10^{7}$	$3 \cdot 10^{7}$	$2.47 \cdot 10^{8}$	$-9.22 \cdot 10^{6}$	$-3.74 \cdot 10^{7}$
2	$-6.4 \cdot 10^{-7}$	$2.97 \cdot 10^{7}$	$2.29 \cdot 10^{8}$	$-5.16 \cdot 10^{7}$	$-2.45 \cdot 10^{8}$	$1.2 \cdot 10^{7}$
3	$-3.6 \cdot 10^{-7}$	$4.1 \cdot 10^{7}$	$-2.29 \cdot 10^{8}$	$-2.2 \cdot 10^{7}$	$-2.45 \cdot 10^{8}$	$9.16 \cdot 10^{6}$
4	$9.9 \cdot 10^{-7}$	$2.15 \cdot 10^{7}$	$-3.2 \cdot 10^{5}$	$-2.47 \cdot 10^{8}$	$-3.22 \cdot 10^{4}$	$-3.74 \cdot 10^{7}$

			$Z = 0.0\ R_L$			
1	$-9.9 \cdot 10^{-7}$	$2.2 \cdot 10^{7}$	$2.6 \cdot 10^{6}$	$2.47 \cdot 10^{8}$	$-3.97 \cdot 10^{5}$	$-3.74 \cdot 10^{7}$
2	$-1.4 \cdot 10^{-7}$	$3.63 \cdot 10^{7}$	$2.29 \cdot 10^{8}$	$-7.6 \cdot 10^{6}$	$-2.45 \cdot 10^{8}$	$8.17 \cdot 10^{6}$
3	$1.4 \cdot 10^{-7}$	$3.63 \cdot 10^{7}$	$-2.29 \cdot 10^{8}$	$7.6 \cdot 10^{6}$	$-2.45 \cdot 10^{8}$	$8.17 \cdot 10^{6}$
4	$9.9 \cdot 10^{-7}$	$2.2 \cdot 10^{7}$	$-2.6 \cdot 10^{6}$	$-2.47 \cdot 10^{8}$	$-3.97 \cdot 10^{5}$	$-3.74 \cdot 10^{7}$

For example in the case of $Z = 0.5\ R_L$ (thus $x_1 = -Z = -5 \cdot 10^{-7}\ m$) the reason that the maximum at cross section 3 is higher than at cross section 2 is that at cross section 3 both $E_{1x}(3)$ and $E_{Lx}(3)$ are negative while at cross section 2 $E_{1x}(2)$ is positive and $E_{Lx}(2)$ is negative. Because of this at cross section 3 $[E_{1x} + E_{Lx}]^2$ much larger than at cross section 2. Actually because of the symmetry $|E_{1x}(3)| = |E_{1x}(2)|$ but $signE_{1x}(3) \neq signE_{1x}(2)$ because $sign\left(\frac{x_p(3)-x_1}{D_1}\right) \neq sign\left(\frac{x_p(2)-x_1}{D_1}\right)$ (see Eq 4).

As an other example in the case of $Z = 0.0\ R_L$ the maximum at cross section 3 is higher than at cross section 4. The reason is that $|E_{Ly}(4)| \ll |E_{Lx}(4)|$ while $|E_{1y}(3)| \cong |E_{1x}(3)| \cong |E_{Lx}(4)|$. Note that $|E_{Ly}(4)| \ll |E_{Lx}(4)|$because the direction of $\underline{E_L}(4)$ is close to the direction of the x axis.

Finally, the analytical equation, Eq 7, for the calculation of the electric field energy density of two surface-charged spheres (the smaller sphere located inside the larger sphere), can be generalized for the case when N small surface-charged spheres are located inside the large sphere (see Appendix 2). Also when the radius of the smaller sphere approaches zero the total surface charge of the smaller sphere, Q_1 approaches zero too and consequently the electric field strength of the smaller sphere, $\underline{E_1}$approaches zero. Thus, based on Eq 7 one can calculate the field energy density around a single charged sphere by:

$$u_F(x_p, y_p) = \frac{\varepsilon_r \varepsilon_0}{2} \underline{E} \cdot \underline{E} = \frac{\varepsilon_r \varepsilon_0}{2} \left(\underline{E_L}\right) \cdot \left(\underline{E_L}\right)$$

$$= \frac{\varepsilon_r \varepsilon_0}{2} (E_{Lx}, E_{Ly}) \cdot (E_{Lx}, E_{Ly})$$

$$= \frac{\varepsilon_r \varepsilon_0}{2} \left([E_{Lx}]^2 + [E_{Ly}]^2 \right)$$

5. Conclusions

Based on the generalized version of Newton's Shell Theorem [7] the electric field energy density, U_F around two surface-charged spheres surrounded by electrolyte where the smaller sphere is inside the larger one is analytically calculated. According to the calculations when the surfaces of the spheres are farther from each other than four times of the Debye length the field energy density around and inside the smaller sphere is basically independent from the presence of the larger sphere. The electric field energy density is maximal when the smaller sphere touches the inner surface of the larger sphere and the maximum of u_F is located at the touching point on the outer surface of the larger sphere.

Acknowledgments

The author is very thankful for Chinmoy Kumar Ghose.

Conflict of interest

The author declares no conflict of interest.

References

1. Chong PLG (2010) Archaebacterial bipolar tetraether lipids: Physico-chemical and membrane properties. Chem Phys Lipids 163: 253–265. https://doi.org/10.1016/j.chemphyslip.2009.12.006
2. Ewald PP (1921) Die berechnung optischer und elektrostatischer gitterpotentiale. Ann Phys-berlin 369: 253–287. https://doi.org/10.1002/andp.19213690304
3. Sugár IP, Thompson TE, Biltonen RL (1999) Monte carlo simulation of two-component bilayers: DMPC/DSPC mixtures. Biophys J 76: 2099–2110. https://doi.org/10.1016/S0006-3495(99)77366-2
4. Almeida PFF (2009) Thermodynamics of lipid interactions in complex bilayers. BBA Biomembranes 1788: 72–85. https://doi.org/10.1016/j.bbamem.2008.08.007 double
5.Bohinc K, Špadina M, Reščič J, et al. (2022) Influence of charge lipid head group structures on electric layer properties. https://doi.org/10.1021/acs.jctc.1c00800
6. Newton I (1999) The Principia: Mathematical Principles of Natural Philosophy, Berkeley: University of California Press, 590.
7. Sugár IP (2020) A generalization of the shell theorem. Electric potential of charged spheres and charged surrounded by https://doi.org/10.3934/biophy.2020007
8. Fetter AL, Walecka JD (2003) Theoretical Mechanics of Particles and Continua, New York: Dover Publications, 307–310.
9. Holtzer AM (1954) The collected papers of Peter JW Debye. Interscience, New York-London, 1954. xxi+ 700 pp., $9.50. J Polym Sci 13: 548. https://doi.org/10.1002/pol.1954.120137203
10. Sugár IP (2021) Electric energies of a charged sphere surrounded by electrolyte. AIMS Biophys 8: 157–164. https://doi.org/10.3934/biophy.2021012
11. Ma Y, Poole K, Goyette J, et al. (2017) Introducing membrane charge and membrane potential to T cell signaling. Front Immunol 8: 1513. https://doi.org/10.3389/fimmu.2017.01513
12. Bar-Shavit Z (2007) The osteoclast: a multinucleated, hematopoietic-origin, bone-resorbing osteoimmune cell. J Cell Biochem 102: 1130–1139. https://doi.org/10.1002/jcb.21553
13. Griffiths DJ (2005) Introduction to electrodynamics. AM J Phys 73: 574. https://doi.org/10.1119/1.4766311
14. Nishino M, Matsuzaki I, Musangile FY, et al. (2020) Measurement and visualization of cell membrane surface charge in fixed cultured cells related with cell morphology. PLoS One 15: e0236373. https://doi.org/10.1371/journal.pone.0236373
15. Trimble WS, Grinstein S (2015) Barriers to free diffusion of proteins and lipids in plasma membrane. J Cell Biol 208: 259–271. https://doi.org/10.1083/jcb.201410071

Looking into mucormycosis coinfections in COVID-19 patients using computational analysis

Ibrahim Khater1 and Aaya Nassar1,2,*

1 Biophysics Department, Faculty of Science, Cairo University, Giza, Egypt
2 Department of Clinical Research and Leadership, School of Medicine and Health Sciences, George Washington University, U.S.A.Real, Portugal

ABSTRACT

Mucormycosis infection may develop after using steroids treatment to improve the severely of the symptoms in coronavirus patients. The rising in the infection rate of mucormycosis has been noticed in patients after COVID-19 infection. To understand the high morbidity mucormycosis coinfection, the cell surface Glucose Regulated Protein 78 (CS-GRP78) was docked to the virus ACE2SARS-CoV-2 RBD to create the ACE2-SARS-CoV-2 RBD-GRP78 complex which facilitates the virus entrance into the cell. The spore coat protein homolog 3 (CotH3) of mucormycosis was modeled and docked to the ACE2-SARS-CoV-2 RBD-GRP78 complex. The binding energies of CotH3 with RBD, ACE2, and GRP78 were calculated. The binding results show that GRP78 substrate-binding domain β weakly binds to the spike RBD combined with ACE2 of the spike RBD-ACE2 complex. Its main function is to stabilize the binding between RBD and ACE2, while CotH3 has a strong affinity for the SARS-CoV-2 RBD, but not for ACE2 or GRP78. The CotH3 appeared to have the same affinity to RBD in the SARS-CoV-2 lineages with some preference to the lineage B.1.617.2 (Delta variant). The complex design illustrates that the coat protein of the fungi is more likely linked to the spike protein of the SARS-CoV-2 virus, which would explain the increased mortality mucormycosis coinfections in COVID-19 patients.

Keywords: mucormycosis; COVID-19; SARS-CoV-2; CotH3; ACE2; GRP78; RBD

1. Introduction

In early May 2021, the rare disease mucormycosis has been declared an epidemic and a lifethreatening infection in India and other South Asian countries. Mucormycosis, also known as zygomycosis and phycomycosis, is a rare and uncommon infection caused by a group of fungi named mucormycetes that are found to be residing in the atmosphere and primarily affect individuals with comorbidities or immunocompromised health problems. The inhalation of fungus spores is the common mode of contamination, however, it can happen as a consequence of a bodily cut or a burn [1,2]. There are different types of mucormycosis, including 1) Rhinocerebral mucormycosis which affects the sinus and can spread to the brain, commonly occurring in uncontrolled diabetic patients and people who had kidney transplant [3–5]; 2) Pulmonary mucormycosis which is commonly observed in cancer patients and people who had organ or stem cell transplant [6]; 3) Gastrointestinal mucormycosis which is commonly observed in young children and premature born babies who might have surgery or received medications that lowered their germ defense ability [7,8], 4) Cutaneous mucormycosis which occurs when the fungi break through the skin due to cuts, burns, surgery or skin trauma that can be

observed in people who do not have compromised immune system [9]; and 5) Disseminated mucormycosis which spreads through the bloodstream and mostly affects the brain and other organs including the heart and spleen [10].

India experienced the second wave of coronavirus 2019 (COVID-19) infections nearly a year after the pandemic was announced. The dominant strain was then named the Delta variant and classified as a strain of concern due to its increased transmissibility and disease severity, according to the Centers for Disease Control and Prevention (CDC) variants classification [11]. Virus strains that scientists consider are more transmissible or capable of producing more severe illnesses are classified as variants of concern (VOC), including B.1.1.7 lineages (Alpha variants), B.1.351 lineages (Beta variants), P.1 lineages (Gamma variants), B.1.427 and B.1.429 lineages (Epsilon variants), and B.1.617.2 and AY lineages described as Delta variants [12].

Mucormycosis symptoms vary depending on where the fungus is growing in the body and some of the mucormycosis symptoms are similar to those symptoms reported after COVID-19 infection. Symptoms of rhinocerebral mucormycosis can include headache, sinus or nasal congestion, and fever; symptoms of pulmonary mucormycosis may include fever, cough, chest pain, and shortness of breath; while symptoms of gastrointestinal mucormycosis may include abdominal pain, nausea, and vomiting. Mucormycosis is more common in people with diabetes and ketoacidosis, as well as those receiving high dosages of corticosteroids after COVID-19 infection. The combination of various clinical data and the isolation of the fungus from clinical samples in culture is required for the probable diagnosis of mucormycosis [1,13,14].

Several risk factors have been reported that would increase the mucormycosis epidemic during the COVID-19 pandemic. Diabetes mellitus, chronic hypertension, cardiovascular diseases, and renal diseases are among the most prominent risk factors linked to an elevated mucormycosis infection rate among COVID-19 patients in India, South Asia, the United States of America, Egypt, Iran, Brazil, Chili [15–18]. Patients with a past medical history of one or more comorbidities and those who have recovered from COVID-19 infection are more susceptible to mucormycosis infection. In addition, it has been noted that unwarranted medication used for treating severe COVID-19 symptoms might have increased patients' likelihood of mucormycosis infection, where steroids are the most frequently prescribed medication for COVID-19, followed by Remdesivir, antibiotics, and Tocilizumab [16,19].The infection rates have been noted to vary among different regions where high infection rates in the United Kingdom, France, Italy, Austria, and Mexico, is reported among COVID-19 patients with organ transplants and immunocompromised people [20–23].

Mucormycosis disease incidence and infection rates have been increasing, particularly during and after infection with the virus causing the COVID-19, and have been observed in India during its second wave of infection [24,25]. Patients with severe COVID-19 symptoms, particularly those admitted to the hospital and into the intensive care unit, are more prone to develop this fungal infection, which has been associated with serious illness and death [22]. COVID-19 specific treatments, such as receiving high-dosage corticosteroids that had been used to treat severe COVID-19 cases, are more likely to increase the risk of mucormycosis in COVID-19 patients [17,26].

Mucormycosis is not a new form of fungus, it is also known as the black fungus, and it is caused by species called Mucorales with Rhizopus Oryzae being known the most. Up to 70% of all cases of mucormycosis are caused by this fungus [27–29]. Mucormycosis infection is more likely in individuals who have a weak immune system. Patients with comorbidities like diabetes are more susceptible to contract mucormycosis, as are those taking steroids to treat severe COVID-19 symptoms. Mucormycosis, on the other hand, is not a contagious disease [30]. Intravenous catheterization and the use of broad-spectrum antibiotics are risk factors for getting mucormycosis. Mucormycosis can also

develop as a result of surgical procedures, hyperalimentation, or malnutrition [31].

Global epidemiological studies of mucormycosis are reasonable in assessing the disease pattern and the infection incidence among people who are at high risk in different countries. Mucormycosis has diverse causal agent factors depending on the geographic location. Rhizopus arrhizus is reported to be the most common agent isolated globally, however, other agents such as Apophysomyces is found to be dominant in Asia, Lichtheimia species are found to be dominant in Europe, while Rhizopus homothallicus, Mucor irregularis, and Thamnostylum lucknowense are reported mostly in Asia [32], [33]. The number of epidemiological studies determining the burden of infection is limited, and disease agents have been associated with geographic dispersion. Study findings showed some significant results of mucormycosis coinfection rate reported in certain countries may be due to the frequency of in COVID-19 patients.

From molecular approach, Mucorales bind to the host cell using the endothelium cell receptor glucose-regulated protein 78 (GRP78) [34–37]. The pathogenesis of mucormycosis is complicated by the fungus' interaction with the endothelium cells that line the blood vessels. Induced endocytosis allows Rhizopus Oryzae strains to attach to human umbilical vein endothelial cells and invade them. [38–40]. Gebremariam et al. found the spore coat protein homolog 3 (CotH3) cell surface protein that binds to GRP78 and examined its role in mucormycosis pathogenesis, where CotH3 acts as a fungal ligand during cell-surface attachment and invasion [41].

The spore coat protein homolog (CotH) cell surface proteins, particularly CotH3, are fungal ligands that enable attachment to the host cell invasion [27–29]. Mucormycosis is characterized by vascular infiltration. The fungal ligands for GRP78 were discovered to be Mucorales spore coat protein homologs (CotH). CotH proteins, which were abundant in Mucorales, were absent in noninvasive pathogens [41]. By binding to GRP78, the heterologous development of CotH3 and CotH2 in Saccharomyces cerevisiae was able to gain the ability to penetrate host cells. According to homology modeling research, GRP78 and both CotH3 and CotH2 have structurally compatible interactions [35,42].

The severe acute respiratory syndrome coronavirus 2 (SARS-CoV-2) causes the coronavirus disease COVID-19. Understanding SARS-CoV-2 transmission and pathophysiology requires knowledge of the entrance receptor. Early research suggested that the SARS-CoV-2 entrance receptor is angiotensin converting enzyme 2 (ACE2), the receptor for entrance into the lung epithelial cells [43], [44–46]. The cell-surface Glucose Directed Protein 78 (Cs-GRP78) can also act as a multifunctional receptor interacting with many ligands and proteins [47–49]. GRP78's substrate-binding domain beta (SBD) has been identified as the binding site for the C480-C488 region within the SARS-CoV-2 spike receptor-binding domain (RBD) [50,51]. Therefore, CS-GRP78 has been predicted to bind to the SARS-CoV-2 spike protein near the putative host cell receptor ACE2 [52,53], where GRP78 depleting antibodies blocks the viral entry; hence, GRP78 in association with both ACE2 and the spike proteins would prevent SARS-CoV-2 invasion of the cell [54,55].

The current work is a computational modeling design of the molecular multi-complex formed by the binding between ACE2 (an entry point in human cells for the coronavirus SARS-CoV-2), RBD (the receptor-binding domain of the coronavirus spike protein), GPR78 (a glucose-regulated protein, which acts as a receptor for host cell invasion of fungi belonging to the Mucorales species, responsible for mucormycosis infection), and CotH3 (a spore coat protein that binds to GPR78 and has a role in the mucormycosis pathogenesis). The assumption is that multiple binding with molecular interactions favors the coinfection between the coronavirus SARS-CoV-2 and the mucormycosis fungi, which would explain why patients with COVID-19 are more likely to develop mucormycosis infection resulting in high morbidity and mortality rates.

2. Materials and methods

2.1. ACE2-RBD interactions

The Protein Data Bank (PDB ID: 6M0J) provided the crystal structure of the SARS-CoV-2 spike receptor-binding domain bound to ACE2 (ACE2-RBD). The binding energy of ACE2-RBD (6M0J) was calculated using the end-point free energy calculation approach called the Molecular MechanicsGeneralized Born Surface Area (MM/GBSA) by using HawkDock web server, a tool used for the protein-protein complex structural prediction and analysis [56]. This method is extensively used to estimate the free binding energies and to find the correct binding conformations for protein-protein systems, treating water molecules explicitly is a rigorous technique to account for the solvent effect. The docked structure is then uploaded to PDBePISA for analyzing the interactions of the proteins. Hydrogen bonds, salt bridges, nonbonded contacts, Gibb's free energy of binding, interactive interfaces, tunnels, and pores are all identified in protein complexes. PDBePISA is available at (https://www.ebi.ac.uk/msd-srv/pisa/cgi-bin/piserver?qi=6jpf).

2.2. GRP78 and ACE2-RBD molecular docking

GRP78/BiP (PDB ID: 5E84) was docked to the spike receptor-binding domain ACE2 of the SARS-CoV-2 crystal structure of the bound with (RBD-ACE2) (PDB ID: 6M0J) using the ClusPro 2 website [57–59]. To evaluate the interactions established, the binding energies of the complexes were assessed using the HawkDock webserver's end-point free energy calculation approach MM/GBSA and the PDBePISA tool.

The Rhizopus Oryzae CotH3 (RO3G_11882) sequence was obtained from the UniProt database (https://www.uniprot.org). CotH3 was modeled by SWISS-MODEL workspace, a fully automated homology-modeling for the protein structure, using the 5JD9.1 chain A template [60–63]. The generated model was then verified using three webservers: PROCHEK, [64,65], VERIFY 3D [66], and ERRAT [67], available online from the University of California UCLA-DOE LAB using the SAVES v.6.0 webserver (https://saves.mbi.ucla.edu).

2.4. CotH3 and ACE2-RBD-GRP78 molecular docking

The ClusPro 2.0 webserver for docking protein-protein interactions was used to dock the modeled CotH3 to the RBD-ACE2-GRP78 complex. The binding energies of complexes were calculated using the end-point free energy calculation methodology MM/GBSA of the HawkDock webserver, and the PDBePISA v1.52 tool was used to analyze the interactions formed. The model was examined for SARS-CoV-2 virus variants including the Wildtype PDB ID: 6M0J chain E, Alpha lineage (B. 1.1.7), Beta lineage (B. 1.351), Gamma lineage (P.1), Delta lineage (B.1.617.2), and Delta plus (or Kappa) lineage (B.1.617.2.1) using PyMol software to map and visualize the complexes [68]. The software is available at (https://pymol.org).

3. Results

The binding energy of ACE2-RBD (6M0J) was first calculated using the MM/GBSA of the HawkDock webserver. The PDBePISA tool was then used to evaluate the expected interface features and key atoms between the docked structures, such as hydrogen bonds and salt bridges, using the PDBePISA tool. The

predicted salt bridges and hydrogen bonds are listed in Table 1. The number of hydrogen bonds and salt bridges is used to assess the likely stability of the interface.

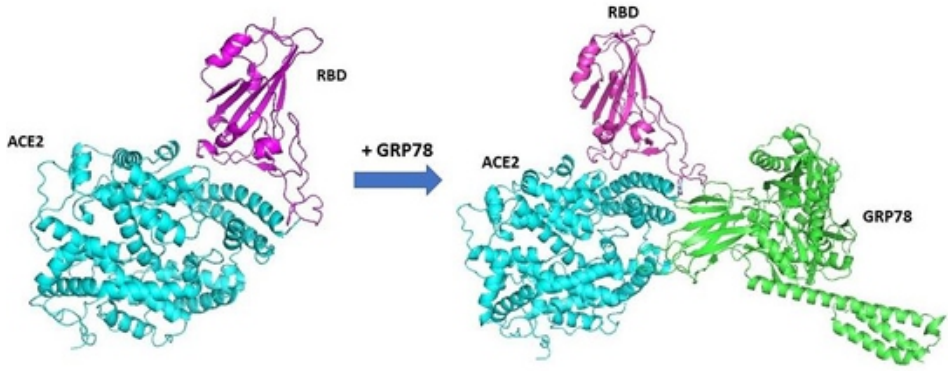

Figure 1. GRP78 was docked to ACE2-RBD (ID: 6M0J) using ClusPro 2.0.

Table 1. The interactions of ACE2-RBD and ACE2-RBD-GRP78 complexes analyzed using PDBePISA. The binding energies were calculated using MM/GBSA of the HawkDock webserver.

ACE2-RBD Complex (6M0J)				ACE2-RBD-GRP78 Complex							
ACE2-RBD interactions (-60.55 ± 0.75) kcal/mol				ACE2-RBD interactions (-87.50 ± 0.85) kcal/mol				GRP78-RBD interactions (-18.5 ± 0.19) kcal/mol			
11 Hydrogen bonds		2 Salt bridges		14 Hydrogen bonds		4 Salt bridges		3 Hydrogen bonds		No Salt bridges	
ACE2 residues	RBD residues	ACE2 residues	RBD residues	ACE2 residues	RBD residues	ACE2 residues	RBD residues	GRP78 residues	RBD residues	GRP78 residues	RBD residues
GLN 24	LYS 417	ASP 30	LYS 417	GLN 24	LYS 417	ASP 30	LYS 417	LYS 435	PRO 479	-	-
ASP 30	GLY 446			ASP 30	GLY 446	LYS 31	GLU 484		LYS 480		
GLU 35	TYR 449			GLU 35	TYR 449				ASN 481		
GLU 37	ASN 487			GLU 37	ASN 487						
ASP 38	TYR 489			ASP 38	TYR 489						
TYR 41	GLN 493			GLN 42	GLN 493						
GLN 42	THR 500			TY R83	GLY 496						
TYR 83	ASN 501			LYS 353	GLN 498						
LYS 353	GLY 502				GLY 502						
ARG 393	TYR 505				TYR 505						

ClusPro 2.0 was then used to dock GRP78 to ACE2-RBD. The resulting complexes were ranked by the binding energies calculated using MM/GBSA where the complex that had the highest binding energy was selected. The results are displayed in Figure 1. The binding energies between GRP78 and ACE2 with RBD within the ACE2-RBD-GRP78 complex were calculated using MM/GBSA. Table 1 Table 1 displays the results of the PDBePISA for the salt-bridge and hydrogen bond interface interactions.

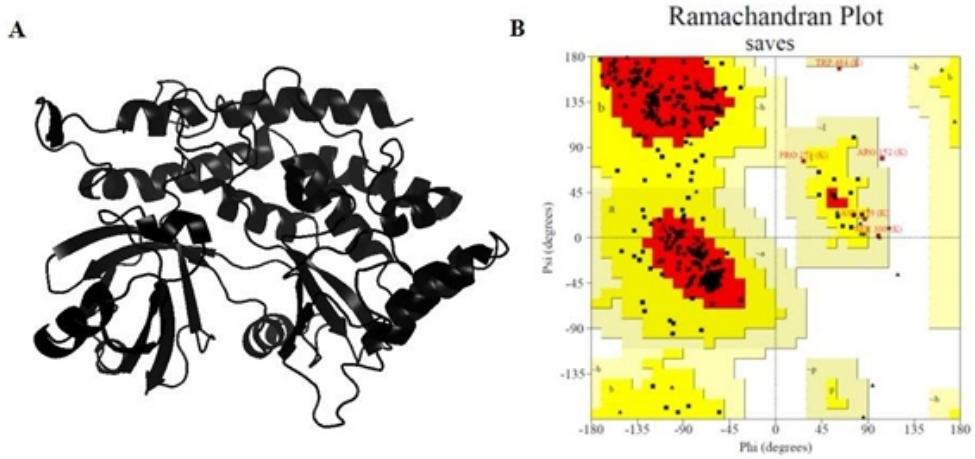

Figure 2. (A) SWISS-MODEL homology model of CotH3 using the 5JD9.1 chain A template. (B) A Ramachandran plot of the CotH3 model reveals that 96.6% of the model residues are in the allowed region.

The CotH3 model of Rhizopus Oryzae was created by the SWISS-MODEL workspace using the 5JD9.1 chain A template (18.68% sequence similarity). The model is shown in Figure 2A. According to the Ramachandran plot, 96.6% of the model residues are within the allowed regions, as shown in Figure 2B. The VERIFY tool assessed approximately 81.5% of the residues to have a 3D-1D score ≥ 0.2, and the overall ERRAT quality factor was 86.12%.

ClusPro 2.0 was used again to dock the CotH3 model to the ACE2-RBD-GRP78 complex. The binding energies of CotH3 and ACE2, RBD, and GRP78 were calculated using MM/GBSA. The complex that had the highest binding energy was selected. Results are ranked by the binding energies and shown in Figure 3. PDBePISA was then used to predict the number of the salt bridges and hydrogen bonds of the interacting interface. Results are listed in Table 2 and the interacting sites are displayed in Figure 4. Approximately 2961 mutations in Spike protein have been found based on the genome sequences of the SARS-CoV-2. We obtained information on all S protein mutations found in the RBD domain. Table 3 displays the binding energies of CotH3 and SARS-CoV-2 RBD for the lineages examined including Alpha, Beta, Gamma, Delta, and Delta plus variants.

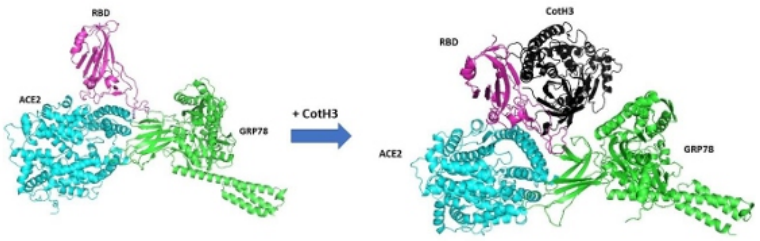

Figure 3. CotH3 docked to the ACE2-RBD-GRP78 complex using ClusPro 2.0.

Table 2. The interactions of ACE2-RBD-CotH3-GRP78 complex analyzed using PDBePISA. The binding energies were calculated using MM/GBSA of the HawkDock webserver.

ACE2-RBD- CotH3-GRP78 Complex											
RBD-CotH3 interactions (-117.40 ± 0.69) kcal/mol				ACE2-CotH3 interactions (20.55 ± 0.61) kcal/mol				GRP78-CotH3 interactions (-2.56 ± 0.28) kcal/mol			
16 Hydrogen bonds		2 Salt bridges		1 Hydrogen bond		No Salt bridges		4 Hydrogen bonds		1 Salt bridge	
RBD residues	CotH3 residues			ACE2 residues	CotH3 residues	ACE2 residues	CotH3 residues	GRP78 residues	CotH3 residues	GRP78 residues	CotH3 residues
ARG 346	TYR 128	ARG 346	ASP 466	GLU35	TYR164	-	-	VAL 429	TYR 164	LYS	ASP 197
TYR 351	ILE 129							ARG466	ASN 170	470	
ASN 354	SER 131							LYS 470	SER 194		
LYS 356	ARG 240										
ARG 357	ASN 245										
ASP 442	ASP 466										
ASN 450	GLU 468										
ILE 468	GLN 475										
	GLN 476										

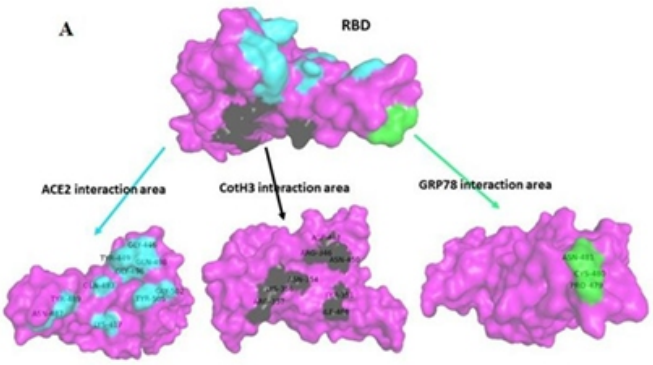

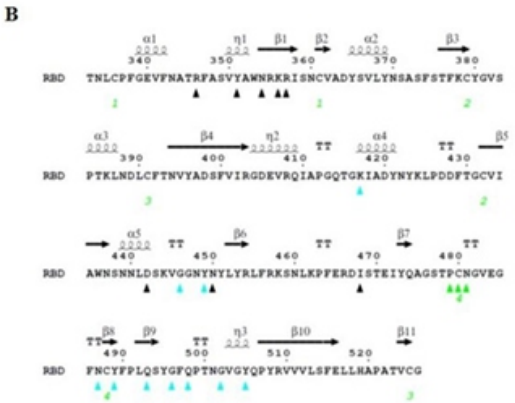

Figure 4. (A) Interactions sites for CotH3 and RBD (cyan), ACE2 (green) and GRP78 (black). **(B)** Interaction residues given by Escript3.

Table 3. The binding energy between CotH3 and RBD for the SARS-CoV-2 virus variants calculated using MM/GBSA of the HawkDock webserver.

SARS-CoV-2 Variants of Concern	RBD-CotH3 Binding Energy (kcal/mol)
Wildtype	−117.40 ± 0.69
Alpha (B.1.1.7)	−117.87 ± 0.10
Beta (B.1.351)	−112.53 ± 2.79
Gamma (P.1)	−113.64 ± 1.30
Delta (B.1.617.2)	−120.42 ± 2.24
Delta plus (B.1.617.2.1)	−122.16 ± 0.56

4. Discussion

The findings of GRP78 binding to the RBD are consistent with Ibrahim et al. study findings [50], which presented that GRP78 binds to 4 regions with the Spike protein of the SARS-CoV-2 virus, among which regions III (C391-C525) and IV (C480C488) show stronger Spike RBD affinity [46]. The results show that the substrate-binding domain β of GRP78 weakly binds to region IV of WT RBD (C480-C488) (−18.5 kcal/mol) forming three hydrogen bonds with PRO479, CYS480, and LYS481, as shown in Table 1. Figure 1 and Figure 3 show that GRP78 and ACE2 bind to the spike RBD surface in roughly the same sites and bind to each other. This is consistent with the findings of Aguiar et al. [69] who showed that the GRP78-binding location overlaps with the ACE2-binding location, albeit the residues engaged in the interactions may differ somewhat. The binding energy between the RBD and ACE2 is increased by around 45%, from −60.55 kcal/mol to −87.5 kcal/mol due to GRP78. In the ACE2-RBD complex, RBD forms 11 hydrogen bonds and two salt bridges with ACE2, whereas in the GRP78-RBD-ACE2 complex, the complex forms 14 hydrogen bonds and four salt bridges with ACE2, as shown in Table 1. Therefore, GRP78 stabilizes the binding of RBD and ACE2, which improves the successful entry of the virus.

The results of CotH3 binding to the ACE2-RBD-GRP78 complex show that while CotH3 weakly attaches itself to GRP78 (−2.63 kcal/mol) and repels from ACE2 (+21.15 kcal/mol), it strongly binds to RBD (−116.91 kcal/mol) as it forms 16 hydrogen bonds and doubles the number of salt bridges with the spike RBD, as listed in Table 2. CotH3 shows a similar affinity for the SARS-CoV-2 virus variants of RBD with some preference for the Delta variants as shown in Table 3. This means that the fungus can enter the cell via the spore coat protein attached to the SARS-CoV-2 RBD spike, which would explain the high coinfection rate of mucormycosis in COVID-19 patients.

5. Conclusions

Mucormycosis, known as black fungus, is a life-threatening fungal infection. The growing number of case mortality and morbidity reported globally during the second wave of the Corona Virus Disease

2019 infection (COVID-19) suggested a high coinfection rate of mucormycosis among COVID-19 patients, where the infection rates of Mucormycosis in COVID-19 patients have been increased.

Current work presents a hypothesis of the molecular interactions that favor the coinfection between the coronavirus SARS-CoV-2 and the mucormycosis fungi. The present research work explains the observed increased morbidity and mortality coinfection in COVID-19 patients with mucormycosis by using the proposed computational molecular model of the fungus spore coat protein that binds to the spike protein of the SARS-CoV-2 virus. The SARS-CoV-2 RBD complex with ACE2 and GRP78 binds to the CotH3 ligand of mucormycosis, carrying it into the host cells during COVID-19 infection. The findings from this study explain that the COVID-19 infection generates an appropriate environment for the spread of Mucorales, resulting in a high infection rate of mucormycosis. The outcome from this study suggests that COVID-19 patients with severe symptoms be evaluated for mucormycosis infection when comorbidities are present, and further research is needed to evaluate the potential association between both infections.

Acknowledgement

This research was funded by The Science and Technology Development Fund (STDF), Grant No. 44575.

Conflict of interest

The authors state that they have no known competing financial interests or personal ties that could have influenced the research presented in this study.

References

1. Sugar AM (1992) Mucormycosis. Clin Infect Dis 14: S126–S129. https://doi.org/10.1093/clinids/14.Supplement_1.S126

2. Daria S, Asaduzzaman M, Shahriar M, et al. (2021) The massive attack of COVID-19 in India is a big concern for Bangladesh: The key focus should be given on the interconnection between the countries. Int J Health Plan M https://doi.org/https://doi.org/10.1002/hpm.3245

3. Song Y, Qiao J, Giovanni G, et al. (2017) Mucormycosis in renal transplant recipients: review of 174 reported cases. BMC Infect Dis 17: 283. https://doi.org/10.1186/s12879-017-2381-1

4. Bouza E, Muñoz P, Guinea J (2006) Mucormycosis: an emerging disease? Clin Microbiol Infec 12: 7–23. https://doi.org/10.1111/j.1469-0691.2006.01604.x

5. Farmakiotis D, Kontoyiannis DP (2016) Mucormycoses. Infect Dis Clin N Am 30: 143–163. https://doi.org/https://doi.org/10.1016/j.idc.2015.10.011

6.Hamilos G, Samonis G, Kontoyiannis DP (2011) Pulmonary mucormycosis. Semin Respir Crit Care Med 32: 693–702. https://doi.org/10.1055/s-0031-1295717

7. Francis JR, Villanueva P, Bryant P, et al. (2018) Mucormycosis in children: review and recommendations for management. https://doi.org/10.1093/jpids/pix107

8. Vallabhaneni S, Mody RK (2015) Gastrointestinal mucormycosis in neonates: a review. Curr Fungal Infect Rep 9: 269–274. https://doi.org/10.1007/s12281-015-0239-9

9. Castrejón-Pérez AD, Welsh EC, Miranda I, et al. (2017) Cutaneous mucormycosis. An Bras Dermatol 92: 304–311. https://doi.org/10.1590/abd1806-4841.20176614

*10. Spellberg B, Edwards JrJ, Ibrahim A (2005) Novel perspectives on mucormycosis: patho*p

Mucormycosis: An emerging disease hysiology, presentation, and management. Clin Microbiol Rev 18: 556–569. https://doi.org/10.1128/CMR.18.3.556-569.2005
11. Yang W, Shaman J (2021) COVID-19 pandemic dynamics in India and impact of the SARS-CoV 2 Delta (B.1.617.2) variant. MedRxiv. https://doi.org/10.1101/2021.06.21.21259268
12. Centers for Disease Control and Preventions, Variants of the Virus. Department of Health & Human Services, 2011. ncov/variants/variants.html.
13. White PL, Dhillon R, Cordey A, et al. (2021) A national strategy to diagnose coronavirus disease 2019–associated invasive fungal disease in the intensive care unit. Clin Infect Dis 73: e1634e1644. https://doi.org/10.1093/cid/ciaa1298
14. Petrikkos G, Skiada A, Lortholary O, et al. (2012) Epidemiology and clinical manifestations of mucormycosis, Clinical Infectious Diseases : An Official Publication of the Infectious Diseases Society of America, 54: S23–S34. https://doi.org/10.1093/cid/cir866
15. Drissi C (2021) Black fungus, the darker side of COVID-19. J Neuroradiol 48: 317–318. https://doi.org/10.1016/j.neurad.2021.07.003
16. Bhanuprasad K, Manesh A, Devasagayam E, et al. (2021) Risk factors associated with the mucormycosis epidemic during the COVID-19 pandemic. Int J Infect Dis 111: 267–270. https://doi.org/10.1016/j.ijid.2021.08.037
17. Garg D, Muthu V, Sehgal IS, et al. (2021) Coronavirus disease (Covid-19) associated mucormycosis (CAM): case report and systematic review of literature. Mycopathologia 186: 289298. https://doi.org/10.1007/s11046-021-00528-2
18. Pal R, Singh B, Bhadada SK, et al. (2021) COVID-19-associated mucormycosis: an updated systematic review of literature. Mycoses 64: 1452–1459. https://doi.org/10.1111/myc.13338
19. Kumar M, Sarma DK, Shubham S, et al. (2021) Mucormycosis in COVID-19 pandemic: Risk factors and linkages. Curr Res Microb https://doi.org/https://doi.org/10.1016/j.crmicr.2021.100057 Sci 2: 100057.
20. Riad A, Shabaan AA, Issa J, et al. (2021) COVID-19-Associated mucormycosis (CAM): caseseries and global analysis of mortality risk factors. J Fungi 7: 837. https://doi.org/10.3390/jof7100837
21. Khatri A, Chang KM, Berlinrut I, et al. (2021) Mucormycosis after Coronavirus disease 2019 infection in a heart transplant recipient–case report and review of literature. J Med Mycol 31: 101125. https://doi.org/10.1016/j.mycmed.2021.101125
22. Singh AK, Singh R, Joshi SR, et al (2021) Mucormycosis in COVID-19: a systematic review of cases reported worldwide and in India. Diabetes Metab Synd 15: 102146. https://doi.org/10.1016/j.dsx.2021.05.019
23. Devnath P, Dhama K, Tareq AM, et al. (2021) Mucormycosis coinfection in the context of global COVID-19 outbreak: a fatal addition to the pandemic spectrum. Int J Surg (London, England) 92: 106031. https://doi.org/10.1016/j.ijsu.2021.106031
24. Gangneux JP, Bougnoux ME, Dannaoui E, et al. (2020) Invasive fungal diseases during COVID 19: We should be prepared. https://doi.org/10.1016/j.mycmed.2020.100971 J Mycol Med 30: 100971.
25. Hoenigl M (2021) Invasive fungal disease complicating coronavirus disease 2019: when it rains, it spores. Clin Infect Dis 73: e1645–e1648. https://doi.org/10.1093/cid/ciaa1342
26. Rabagliati R, Rodríguez N, Núñez C, et al. (2021) COVID-19–associated mold infection in critically Ill patients, Chile. Emerg https://doi.org/https://doi.org/10.3201/eid2705.204412
27. Ribes JA, Vanover-Sams CL, Baker DJ (2000) Zygomycetes in human disease. Clin Microbiol Rev 13: 236–301. https://doi.org/10.1128/CMR.13.2.236
28. Roden MM, Zaoutis TE, Buchanan WL, et al. (2005) Epidemiology and outcome of zygomycosis: a review of 929 reported cases. Clin Infect Dis 41: 634–653. https://doi.org/10.1086/432579

29. Ibrahim AS, Spellberg B, Walsh TJ, et al. (2012) Pathogenesis of mucormycosis. Clin Infect Dis 54: S16–S22. https://doi.org/10.1093/cid/cir865
30. John TM, Jacob CN, Kontoyiannis DP (2021) When uncontrolled diabetes mellitus and severe COVID-19 converge: the perfect storm for mucormycosis. J Fungi 7: 298. https://doi.org/10.3390/jof7040298
31. Stein DK, Sugar AM (1989) Fungal infections in the immunocompromised host. Diagn Micr Infec Dis 12: 221–228. https://doi.org/https://doi.org/10.1016/0732-8893(89)90140-5
32. Prakash H, Chakrabarti A (2019) Global epidemiology of mucormycosis. J Fungi 5: 26. https://doi.org/10.3390/jof5010026
33. Skiada A, Pavleas I, Drogari-Apiranthitou M (2020) Epidemiology and diagnosis of mucormycosis: an update. J Fungi 6: 265. https://doi.org/10.3390/jof604026
34. Ibrahim AS, Spellberg B, Avanessian V, et al. (2005) Rhizopus oryzae adheres to, is phagocytosed by, and damages endothelial cells in vitro. Infect Immun 73: 778–783. https://doi.org/10.1128/IAI.73.2.778-783.2005
35. Liu M, Spellberg B, Phan QT, et al. (2010) The endothelial cell receptor GRP78 is required for mucormycosis pathogenesis in diabetic mice. J Clin Invest 120: 1914–1924. https://doi.org/10.1172/JCI42164
36. Gumashta J, Gumashta R (2021) COVID19 associated mucormycosis: Is GRP78 a possible link? J Infect Public Heal 14: 1351–1357. https://doi.org/10.1016/j.jiph.2021.09.004
37. Chandra S, Rawal R (2021) The surge in Covid related mucormycosis. J Infection 83: 381–412. https://doi.org/10.1016/j.jinf.2021.06.008
38. Ibrahim AS, Edwards JEJ, Filler SG (2003) Zygomycosis, Clinical Mycology, New York: Oxford University Press, 241–251.
39. Ibrahim AS (2011) Host cell invasion in mucormycosis: role of iron. Curr Opin Microbiol 14: 406–411. https://doi.org/10.1016/j.mib.2011.07.004
40. Ibrahim AS (2014) Host-iron assimilation: pathogenesis and novel therapies of mucormycosis. Mycoses 57: 13–17. https://doi.org/10.1111/myc.12232
41. Gebremariam T, Liu M, Luo G, et al (2014) CotH3 mediates fungal invasion of host cells during mucormycosis. J Clin Invest 124: 237–250. https://doi.org/10.1172/JCI71349
42. Alqarihi A, Gebremariam T, Gu Y, et al. (2020) GRP78 and integrins play different roles in host cell invasion during mucormycosis. MBio 11: e01087–20. https://doi.org/10.1128/mBio.0108720
43. Cuervo NZ, Grandvaux N (2020) ACE2: Evidence of role as entry receptor for SARS-CoV-2 and implications in comorbidities. ELife 9: e61390. https://doi.org/10.7554/eLife.61390
44. Li W, Moore MJ, Vasilieva N, et al. (2003) Angiotensin-converting enzyme 2 is a functional receptor for the SARS coronavirus. Nature 426: 450–454. https://doi.org/10.1038/nature02145
45. Pandiar D, Kumar NS, Anand R, et al. (2021) Does COVID 19 generate a milieu for propagation of mucormycosis? Med Hypotheses 152: 110613. https://doi.org/10.1016/j.mehy.2021.110613
46. Verma J, Subbarao N (2021) Insilico study on the effect of SARS-CoV-2 RBD hotspot mutants' interaction with ACE2 to understand the binding affinity and stability. Virology 561: 107–116. https://doi.org/10.1016/j.virol.2021.06.009
47. Li J, Lee AS (2006) Stress induction of GRP78/BiP and its role in cancer. Curr Mol Med 6: 4554. https://doi.org/10.2174/156652406775574523
48. Perlman S, Netland J (2009) Coronaviruses post-SARS: update on replication and pathogenesis. Nat Rev Microbiol 7: 439–450. https://doi.org/10.1038/nrmicro2147
49. Lee AS (2014) Glucose-regulated proteins in cancer: molecular mechanisms and therapeutic potential. Nat Rev Cancer 14: 263–276. https://doi.org/10.1038/nrc3701

50. Ibrahim IM, Abdelmalek DH, Elshahat ME, et al. (2020) COVID-19 spike-host cell receptor GRP78 site prediction. https://doi.org/10.1016/j.jinf.2020.02.026 J Infection 80: 554–562.
51. Ha DP, Van Krieken R, Carlos AJ, et al. (2020) The stress-inducible molecular chaperone GRP78 as potential therapeutic target for coronavirus infection. J Infection 81: 452–482. https://doi.org/10.1016/j.jinf.2020.06.017
52. Elfiky AA, Ibrahim IM, Ismail AM, et al. (2021) A possible role for GRP78 in cross vaccination against COVID-19. J Infection 82: 282–327. https://doi.org/10.1016/j.jinf.2020.09.004
53. Elfiky AA (2020) SARS-CoV-2 spike-heat shock protein A5 (GRP78) recognition may be related to the immersed human coronaviruses. https://doi.org/10.3389/fphar.2020.577467 Front Pharmacol 11: 577467.
54. Saghazadeh A, Rezaei N (2020) Towards treatment planning of COVID-19: Rationale and hypothesis for the use of multiple immunosuppressive agents: anti-antibodies, immunoglobulins, and corticosteroids. https://doi.org/10.1016/j.intimp.2020.106560 Immunopharmacol 84: 106560.
55. Carlos AJ, Ha DP, Yeh DW, et al. (2021) GRP78 binds SARS-CoV-2 Spike protein and ACE2 and GRP78 depleting antibody blocks viral entry and infection in vitro. BioRxiv https://doi.org/10.1101/2021.01.20.427368
56. Weng G, Wang E, Wang Z, et al. (2019) HawkDock: a web server to predict and analyze the protein–protein complex based on computational docking and MM/GBSA. Nucleic Acids Res 47: W322–W330. https://doi.org/10.1093/nar/gkz397
57. Kozakov D, Beglov D, Bohnuud T, et al. (2013) How good is automated protein docking? Proteins 81: 2159–2166. https://doi.org/10.1002/prot.24403
58. Vajda S, Yueh C, Beglov D, et al. (2017) New additions to the ClusPro server motivated by CAPRI. Proteins 85: 435–444. https://doi.org/https://doi.org/10.1002/prot.25219
59. Kozakov D, Hall DR, Xia B, et al. (2017) The ClusPro web server for protein–protein docking. Nat Protoc 12: 255–278. https://doi.org/10.1038/nprot.2016.169
60. Waterhouse A, Bertoni M, Bienert S, et al. (2018) SWISS-MODEL: homology modelling of protein structures and complexes. Nucleic Acids Res 46: W296–W303.
61. Bienert S, Waterhouse A, de Beer TAP, et al. (2017) The SWISS-MODEL repository-new features and functionality. Nucleic Acids Res 45: D313–D319.
62. Guex N, Peitsch MC, Schwede T (2009) Automated comparative protein structure modeling with SWISS-MODEL and Swiss-PdbViewer: a historical perspective. Electrophoresis 30: S162–S173. https://doi.org/10.1002/elps.200900140
63. Studer G, Tauriello G, Bienert S, et al. (2021) ProMod3—A versatile homology modelling toolbox. PLoS Comput Biol 17: e1008667. https://doi.org/10.1371/journal.pcbi.1008667
64. Laskowski RA, MacArthur MW, Moss DS, et al. (1993) PROCHECK: a program to check the stereochemical quality of protein structures. J Appl Crystallogr 26: 283–291. https://doi.org/https://doi.org/10.1107/S0021889892009944
65. Laskowski RA, Rullmann JAC, MacArthur MW, et al. (1996) AQUA and PROCHECK-NMR: Programs for checking the quality of protein structures solved by NMR. J Biomol NMR 8: 477 486. https://doi.org/10.1007/BF00228148
66. Eisenberg D, Lüthy R, Bowie JU (1997) VERIFY3D: assessment of protein models with threedimensional profiles. Method Enzymol 277: 396–404. https://doi.org/10.1016/s00766879(97)77022-8
67. Colovos C, Yeates TO (1993) Verification of protein structures: patterns of nonbonded atomic interactions. Protein Sci 2: 1511–1519. https://doi.org/10.1002/pro.5560020916
68. DeLano WL (2002) Pymol: An open-source molecular graphics tool. CCP4 Newsl Protein

Crystallogr 40: 82–92.
69. Aguiar JA, Tremblay BJM, Mansfield MJ, et al. (2020) Gene expression and in situ protein profiling of candidate SARS-CoV-2 receptors in human airway epithelial cells and lung tissue. Eur Respir J 56: 2001123. https://doi.org/10.1183/13993003.01123-2020

Instructions for Authors

Essentials for Publishing in this Journal

1 Submitted articles should not have been previously published or be currently under consideration for publication elsewhere.

2 Conference papers may only be submitted if the paper has been completely re-written (taken to mean more than 50%) and the author has cleared any necessary permission with the copyright owner if it has been previously copyrighted.

3 All our articles are refereed through a double-blind process.

4 All authors must declare they have read and agreed to the content of the submitted article and must sign a declaration correspond to the originality of the article.

Submission Process

All articles for this journal must be submitted using our online submissions system. http://enrichedpub.com/ . Please use the Submit Your Article link in the Author Service area.

Manuscript Guidelines

The instructions to authors about the article preparation for publication in the Manuscripts are submitted online, through the e-Ur (Electronic editing) system, developed by **Enriched Publications Pvt. Ltd**. The article should contain the abstract with keywords, introduction, body, conclusion, references and the summary in English language (without heading and subheading enumeration). The article length should not exceed 16 pages of A4 paper format.

Title

The title should be informative. It is in both Journal's and author's best interest to use terms suitable. For indexing and word search. If there are no such terms in the title, the author is strongly advised to add a subtitle. The title should be given in English as well. The titles precede the abstract and the summary in an appropriate language.

Letterhead Title

The letterhead title is given at a top of each page for easier identification of article copies in an Electronic form in particular. It contains the author's surname and first name initial .article title, journal title and collation (year, volume, and issue, first and last page). The journal and article titles can be given in a shortened form.

Author's Name

Full name(s) of author(s) should be used. It is advisable to give the middle initial. Names are given in their original form.

Contact Details

The postal address or the e-mail address of the author (usually of the first one if there are more Authors) is given in the footnote at the bottom of the first page.

Type of Articles

Classification of articles is a duty of the editorial staff and is of special importance. Referees and the members of the editorial staff, or section editors, can propose a category, but the editor-in-chief has the sole responsibility for their classification. Journal articles are classified as follows:

Scientific articles:

1. Original scientific paper (giving the previously unpublished results of the author's own research based on management methods).

2. Survey paper (giving an original, detailed and critical view of a research problem or an area to which the author has made a contribution visible through his self-citation);

3. Short or preliminary communication (original management paper of full format but of a smaller extent or of a preliminary character);

4. Scientific critique or forum (discussion on a particular scientific topic, based exclusively on management argumentation) and commentaries. Exceptionally, in particular areas, a scientific paper in the Journal can be in a form of a monograph or a critical edition of scientific data (historical, archival, lexicographic, bibliographic, data survey, etc.) which were unknown or hardly accessible for scientific research.

Professional articles:

1. Professional paper (contribution offering experience useful for improvement of professional practice but not necessarily based on scientific methods);
2. Informative contribution (editorial, commentary, etc.);
3. Review (of a book, software, case study, scientific event, etc.)

Language

The article should be in English. The grammar and style of the article should be of good quality. The systematized text should be without abbreviations (except standard ones). All measurements must be in SI units. The sequence of formulae is denoted in Arabic numerals in parentheses on the right-hand side.

Abstract and Summary

An abstract is a concise informative presentation of the article content for fast and accurate Evaluation of its relevance. It is both in the Editorial Office's and the author's best interest for an abstract to contain terms often used for indexing and article search. The abstract describes the purpose of the study and the methods, outlines the findings and state the conclusions. A 100- to 250-Word abstract should be placed between the title and the keywords with the body text to follow. Besides an abstract are advised to have a summary in English, at the end of the article, after the Reference list. The summary should be structured and long up to 1/10 of the article length (it is more extensive than the abstract).

Keywords

Keywords are terms or phrases showing adequately the article content for indexing and search purposes. They should be allocated heaving in mind widely accepted international sources (index, dictionary or thesaurus), such as the Web of Science keyword list for science in general. The higher their usage frequency is the better. Up to 10 keywords immediately follow the abstract and the summary, in respective languages.

Acknowledgements

The name and the number of the project or programmed within which the article was realized is given in a separate note at the bottom of the first page together with the name of the institution which financially supported the project or programmed.

Tables and Illustrations

All the captions should be in the original language as well as in English, together with the texts in illustrations if possible. Tables are typed in the same style as the text and are denoted by numerals at the top. Photographs and drawings, placed appropriately in the text, should be clear, precise and suitable for reproduction. Drawings should be created in Word or Corel.

Citation in the Text

Citation in the text must be uniform. When citing references in the text, use the reference number set in square brackets from the Reference list at the end of the article.

Footnotes

Footnotes are given at the bottom of the page with the text they refer to. They can contain less relevant details, additional explanations or used sources (e.g. scientific material, manuals). They cannot replace the cited literature.
The article should be accompanied with a cover letter with the information about the author(s): surname, middle initial, first name, and citizen personal number, rank, title, e-mail address, and affiliation address, home address including municipality, phone number in the office and at home (or a mobile phone number). The cover letter should state the type of the article and tell which illustrations are original and which are not.

Address of the Editorial Office:

Enriched Publications Pvt. Ltd.
S-9,IInd FLOOR, MLU POCKET,
MANISH ABHINAV PLAZA-II, ABOVE FEDERAL BANK,
PLOT NO-5, SECTOR -5, DWARKA, NEW DELHI, INDIA-110075,
PHONE: - + (91)-(11)-45525005